Timing Calibration of the Trigger System for the Drift Tube Detector of the OPERA Neutrino Oscillation Experiment

Dissertation
zur Erlangung des Doktorgrades
des Fachbereichs Physik
der Universität Hamburg

vorgelegt von
Jan Lenkeit
aus Hamburg

Hamburg
2015

Timing Calibration of the Trigger System for the Drift Tube Detector of the OPERA Neutrino Oscillation Experiment

Abstract

The OPERA experiment searches for $\nu_\mu \to \nu_\tau$ oscillations in an almost pure ν_μ beam. The goal is to observe the oscillations in appearance mode by using a large-scale lead/emulsion target to resolve individual ν_τ interactions. Magnetic spectrometers measure the charge and momentum of beam induced muons leaving the target sections. The Precision Tracker, a drift tube detector consisting of almost 10 000 drift tubes, provides the tracking information inside the spectrometers. The coordinate measurement in the drift tubes is derived from a time measurement relative to an external trigger signal. In order to reach the required momentum resolution of less than 25 % for particle momenta up to 25 GeV, the uncertainty on the trigger timing must not exceed a value of 5 ns. In this thesis, a procedure for the timing calibration of the trigger system is presented. A step-by-step calibration of the corresponding signal paths is described. Applying all calibration results, a spatial resolution of 255 µm is achieved for the Precision Tracker, meeting the specified requirements. Furthermore, a method using the calibrated trigger system for performing time of flight measurements with atmospheric muons is developed. The average error on the measured flight times is ±4.5 ns.

Zeitliche Kalibration des Triggersystems des Driftröhrendetektors am Neutrinooszillationsexperiment OPERA

Kurzfassung

Das OPERA-Experiment sucht nach $\nu_\mu \to \nu_\tau$-Oszillationen in einem nahezu reinen ν_μ-Strahl. Ziel ist der direkte Nachweis der Oszillationen durch die Rekonstruktion einzelner ν_τ-Wechselwirkungen in einem massiven Blei-/Emulsions-Target. Magnetspektrometer messen Ladung und Impuls von strahlinduzierten Myonen, welche die Target-Bereiche verlassen. Der Precision Tracker, ein Driftröhrendetektor mit nahezu 10 000 Messkanälen, liefert die Spurinformationen innerhalb der Spektrometer. Die Ortsmessung in der Driftröhre erfolgt über eine Zeitmessung relativ zu einem externen Triggersignal. Um die angestrebte Impulsauflösung von weniger als 25 % für Teilchenimpulse bis zu 25 GeV zu erreichen, darf der zeitliche Fehler des Triggersignals maximal 5 ns betragen. Im Rahmen dieser Arbeit wird eine Prozedur für die zeitliche Kalibration des Triggersystems präsentiert. Die Kalibration erfolgt sukzessiv für alle Signalwege des Triggersignals. Unter Verwendung sämtlicher Kalibrationsergebnisse erreicht der Precision Tracker eine Ortsauflösung von 255 µm, welche die gestellten Anforderungen erfüllt. Darüber hinaus wird eine Methode entwickelt, die eine Flugzeitbestimmung für atmosphärische Myonen mittels des kalibrierten Triggersystems ermöglicht. Der mittlere Fehler der so gemessenen Flugzeiten beträgt ±4,5 ns.

Contents

Chapter 1

Introduction

Neutrino oscillations are by now a well-established concept to explain various experimentally observed phenomena associated with the time evolution of neutrinos. The first indication for processes changing the flavors of propagating neutrinos over time came from solar neutrino experiments. They measured a significant deficit in the neutrino flux from the Sun as compared to theoretical predictions. During the last few decades, numerous experiments have confirmed the existence of neutrino oscillations by investigating neutrinos from different natural and artificial sources, using various detection techniques.

The primary scientific goal of the OPERA[1] experiment is to give conclusive evidence for $\nu_\mu \to \nu_\tau$ oscillations by direct observation of ν_τ appearance on an event-by-event basis. OPERA uses the CNGS[2] beam produced at CERN[3] as an almost pure ν_μ source. To be able to detect the short-lived τ leptons resulting from ν_τ interactions, a target mass of more than $1\,\mathrm{kt}$ is used, combined with nuclear emulsions featuring a sub-micrometer spatial resolution. In order to gain real-time information on neutrino events in OPERA, a hybrid detector design was chosen. Electronic detectors track charged particles coming from neutrino interactions inside the passive lead/emulsion target and allow for locating the interaction vertices. Spectrometers consisting of large dipole magnets and tracking detectors determine the charge and momentum of muons. This information is essential for exploiting the muonic τ decay channel as well as for background reduction. The Precision Tracker (PT) is part of the muon spectrometers. It consists of almost $10\,000$ drift tubes and measures the magnitude of the muons' deflection when crossing the magnetic field. Since the coordinate measurement of a drift tube is derived from a time

---

[1] Oscillation Project with Emulsion-Tracking Apparatus, L'Aquila, Italy

[2] CERN Neutrinos to Gran Sasso

[3] Conseil Européen pour la Recherche Nucléaire/European Organization for Nuclear Research, Geneva, Switzerland

measurement relative to an external trigger signal, the tube's spatial resolution directly depends on the timing resolution of the trigger system.

In this thesis, a procedure for the timing calibration of the PT trigger system is presented. A step-by-step calibration of the propagation delays on all corresponding cables and electronic components is performed, using test pulses and selected detector signals as well as different measurement techniques. Furthermore, the correlation between the trigger timing and the ambient temperature is examined. To be able to determine the direction of flight for particles crossing the OPERA spectrometers, a method for performing time of flight measurements using the calibrated trigger system is developed.

This thesis is divided into seven chapters. Following the introduction, Chapter 2 gives a short overview of neutrino physics with a focus on neutrino oscillations, and presents a selection of currently open questions concerning the neutrino's properties. Chapter 3 describes the OPERA experiment, including the neutrino beam, the features and sub-systems of the OPERA detector, the data taking procedure and the major background sources for the τ decay search. At the end of the chapter, the analysis results accomplished so far are presented. In Chapter 4 the trigger system for the drift tube detector is described in detail. Following an explanation of the principle of the drift time measurement, the general concept and layout of the trigger system is introduced. The function of all electronic components is described and the hardware modifications implemented in the course of the experiment are outlined. Moreover, a method to determine the trigger efficiency is developed and applied to the data of all OPERA physics runs. In Chapter 5 the impact of the trigger timing accuracy on the drift tubes' spatial resolution is estimated and the general principle of time of flight measurements with the PT trigger system is explained. Following this, the procedure developed for the timing calibration of the trigger system is described in subsections according to the successive calibration steps for the different signal paths. In Chapter 6 the results of the timing calibration are presented and discussed. Moreover, the temperature dependence of the trigger timing is determined and a method for performing time of flight measurements with atmospheric muons using the calibrated trigger system is developed and demonstrated. Finally, a conclusion is given in Chapter 7.

Within this thesis the speed of light c is set to one. Therefore, all particle energies, momenta and masses are expressed in eV.

Chapter 2

Neutrino Physics

In 1914, 18 years after Henri Becquerel discovered the radioactive decay, the English physicist James Chadwick determined the energy spectrum of electrons emitted during the β decay of ^{214}Pb and ^{214}Bi. As opposed to the discrete spectral lines of α and γ decays, Chadwick measured a continuous spectrum [Cha14]. This discovery contradicted the assumption of a two-body decay. A few years later, the fractional (1/2) spin of the electron was discovered [Pau25, UG25] along with the observation that in β decays the mother and the daughter nucleus always carry the same type of spin, either integer or fractional. Therefore, a two-body decay would also have been inconsistent with the conservation of the angular momentum. To resolve these two problems, in December 1930 Wolfgang Pauli postulated an electrically neutral spin 1/2 particle that is emitted along with the electron and escapes detection. This particle was later named neutrino by Enrico Fermi. It took more than 25 years until the neutrino's existence was first verified experimentally.

2.1   Discovery of the Neutrino

Over the past 60 years, various experiments were dedicated to the detection of neutrinos and were able to reveal several of its properties. However, many questions concerning the neutrino's nature remain unanswered and require further experimental investigation. An incomplete list of yet unresolved issues is given in Section 2.3.

The first experiment to detect a neutrino was carried out in 1956 by Frederick Reines and Clyde Cowan at the Savannah River Plant, a nuclear reactor facility in South Carolina, USA. Electron antineutrinos emitted during the nuclear fission processes were detected through the observation of the

so-called inverse β decay:

$$\overline{\nu}_e + p^+ \rightarrow e^+ + n. \tag{2.1}$$

The signal of this reaction is a coincidence measurement of the two photons from the annihilation of the positron and the γ-emission following the neutron capture by a nucleus [C+56].

In 1960 Bruno Pontecorvo and Melvin Schwartz suggested an experiment producing a beam of high-energetic muon neutrinos by means of a proton synchrotron [Pon60, Sch60]. The protons were to be directed onto a fixed target, yielding high-energetic charged pions and kaons boosted in forward direction. These would decay in-flight mainly into μ and ν_μ, producing the neutrino beam. The idea was to probe the presumed difference between the neutrino emitted in β decay and the one accompanied by muons. In 1962 this plan was put into action at the Brookhaven National Laboratory by Leon M. Lederman, Melvin Schwartz and Jack Steinberger. ν_μ and ν_e events were discriminated by the different tracking profiles of the muon and the electron. A large surplus of detected ν_μ events proved the existence of a second neutrino flavor [D+62]. Moreover, the experiment marked the birth of accelerator driven neutrino production, a technique used for many high-energy neutrino experiments since then, e.g. OPERA (see Section 3.1).

The detection of neutrinos of the third flavor was achieved by the DONUT[1] experiment at Fermilab[2] in 2000 [K+01]. The tau neutrinos were produced via the decay of charmed mesons which in turn were created using the proton beam of the Tevatron accelerator. DONUT used electronic detectors to identify neutrino events, and nuclear emulsions to detect the short-lived τ lepton originating from the neutrino event vertex. The general concept for observing ν_τ interactions was adapted for the OPERA experiment and is described in detail in Chapter 3.

Already before the discovery of the ν_τ, several experiments determined the number of light active neutrino species by measuring the Z^0 decay width.[3] All four detectors at the LEP[4] accelerator at CERN measured both the total decay width and the partial widths of decays into hadrons and charged leptons with high precision. Assuming lepton universality, the width of decays into

---

[1] Direct Observation of Nu Tau

[2] Fermi National Accelerator Laboratory, Batavia, USA

[3] "Light" refers to neutrino masses smaller than half the Z^0-mass ($m_Z = 91.2\,\text{GeV}$), and "active" refers to the property of participating in the weak interaction.

[4] Large Electron-Positron Collider

neutrinos is the difference between the total Z^0 decay width and the width of all visible decays. By comparing the combined experimental results to the theoretical predictions, the number of neutrino species was determined to be 2.9840 ± 0.0082 [S+06], representing strong evidence that no more than three generations of leptons and quarks exist.

In conclusion, today's Standard Model of particle physics knows three types of neutrinos and their corresponding antiparticles. Neutrinos are electrically neutral fermions participating in the weak interaction only. The Standard Model assumes the neutrinos to be massless, a hypothesis disproved by the evidence of neutrino oscillations.

2.2 Neutrino Oscillations

Neutrino oscillations are defined as oscillating transitions of the type $\nu_\alpha \leftrightarrow \nu_\beta$ or $\overline{\nu}_\alpha \leftrightarrow \overline{\nu}_\beta$ with $\alpha, \beta = e, \mu, \tau$. In 1957 Bruno Pontecorvo proposed the idea of neutrino oscillations, although at that time, the ν_μ had not yet been discovered, he thought of $\nu \leftrightarrow \overline{\nu}$ transitions similar to the ones in the neutral kaon system [Pon57]. The first indications of flavor oscillations came from experiments designed to validate the standard solar model by measuring the ν_e flux from the Sun.

Between 1970 and 1994 a group of physicists around Raymond Davis, Jr. conducted a radiochemical experiment in the Homestake Gold Mine in South Dakota, USA [D+68]. A tank filled with $615\,\mathrm{t}$ of C_2Cl_4 was used to capture solar electron neutrinos with energies as low as $814\,\mathrm{keV}$ through the reaction

$$\nu_e + {}^{37}\mathrm{Cl} \rightarrow {}^{37}\mathrm{Ar} + e^-. \tag{2.2}$$

The extraction and counting of the radioactive ${}^{37}\mathrm{Ar}$ atoms produced, showed a significant discrepancy between the measured and the predicted solar neutrino flux. Only about one third of the number of ν_e expected from calculations based on the standard solar model [BP95] was detected in the Homestake experiment [C+98]. This deficit was referred to as the solar neutrino problem. Also the gallium experiments SAGE[5] in Baksan, Russia, and GALLEX[6]/GNO[7] in the LNGS[8] underground laboratory measured a solar neutrino deficit [A+94, K+10, A+05]. Likewise, the water Cherenkov detector

---

[5] Soviet-American Gallium Experiment

[6] Gallium Experiment

[7] Gallium Neutrino Observatory

[8] Laboratori Nazionali del Gran Sasso, L'Aquila, Italy

Kamiokande[9] in Japan confirmed the deficit, offering a real-time neutrino detection including directional information by detecting elastic ν_e scattering on electrons [F$^+$96].

Although the first evidence of neutrino oscillations was given in 1998 by the Super-Kamiokande experiment in the atmospheric sector (see Section 2.2.2), the solution to the solar neutrino problem was found by the SNO[10] experiment in Ontario, Canada, in 2001 [A$^+$01c]. SNO was sensitive to all neutrino flavors through the detection of elastic scattering and NC[11] interactions. At the same time, only the electron type neutrinos from the Sun were also detected through CC[12] interactions, since the solar neutrino energies are too low to produce μ or τ. While the ν_e flux again showed a deficit, the total solar neutrino flux was consistent with the predictions. Firstly, this result confirmed the validity of the standard solar model. And secondly, it implied that a significant fraction of the ν_e change flavor between the point of their origin in the Sun and the point of their detection on Earth.

To describe neutrino flavor oscillations, the propagating neutrinos have to be regarded as mixed mass states. Neutrinos are produced and detected as weak eigenstates $|\nu_\alpha\rangle$ with a distinct flavor $\alpha = e, \mu, \tau$ which is defined by the associated charged lepton. In case of a non-zero neutrino mass, the neutrino's mass eigenstates $|\nu_i\rangle$, with $i = 1, 2, 3$, are not necessarily identical with the flavor eigenstates. The flavor eigenstates can be expressed as a superposition of the mass eigenstates:

$$|\nu_\alpha\rangle = \sum_i U_{\alpha i}^* |\nu_i\rangle . \tag{2.3}$$

U is the unitary lepton mixing matrix called PMNS matrix[13]. It can be parametrized using three mixing angles θ_{12}, θ_{13} and θ_{23}, and one CP[14] violating phase δ:

$$U = \begin{pmatrix} 1 & 0 & 0 \\ 0 & c_{23} & s_{23} \\ 0 & -s_{23} & c_{23} \end{pmatrix} \begin{pmatrix} c_{13} & 0 & s_{13}e^{-i\delta} \\ 0 & 1 & 0 \\ -s_{13}e^{i\delta} & 0 & c_{13} \end{pmatrix} \begin{pmatrix} c_{12} & s_{12} & 0 \\ -s_{12} & c_{12} & 0 \\ 0 & 0 & 1 \end{pmatrix} \tag{2.4}$$

---

[9] Kamioka Nucleon Decay Experiment

[10] Sudbury Neutrino Observatory

[11] Neutral Current

[12] Charged Current

[13] Named after the physicists who first introduced the idea of neutrino mixing: Bruno Pontecorvo, Ziro Maki, Masami Nakagawa and Shoichi Sakata [Pon57, M$^+$62]

[14] Charge parity

with $s_{ij} = \sin(\theta_{ij})$ and $c_{ij} = \cos(\theta_{ij})$. If neutrinos are so-called Majorana particles, i.e. their own antiparticles, the mixing matrix U has to be multiplied by the matrix M,

$$M = \begin{pmatrix} e^{i\alpha_1/2} & 0 & 0 \\ 0 & e^{i\alpha_2/2} & 0 \\ 0 & 0 & 1 \end{pmatrix}, \tag{2.5}$$

introducing two additional Majorana phases α_1 and α_2.

A direct consequence of the mixing of flavor and mass eigenstates, different neutrino mass eigenstates and, consequently, non-zero mass squared differences $\Delta m_{ij}^2 = m_i^2 - m_j^2$, is the existence of neutrino oscillations. Depending on the neutrino's energy E and the distance L it travels between origin and detection there is a non-vanishing probability of a flavor change. In a simplified approach, only two flavors are considered in the following. For many experiments this is a valid approximation since two of the Δm^2 differ greatly from each other, $\Delta m_{21}^2 \ll |\Delta m_{32}^2| \approx |\Delta m_{31}^2|$ (see Sections 2.2.1 and 2.2.2), and the mixing angle θ_{13} is very small (see Section 2.2.3). The mixing matrix with only one mixing angle θ is then reduced to:

$$U = \begin{pmatrix} \cos\theta & \sin\theta \\ -\sin\theta & \cos\theta \end{pmatrix}. \tag{2.6}$$

With a single mass squared difference $\Delta m^2 = m_1^2 - m_2^2$ the probability of a neutrino produced in a flavor state α to be detected in a different flavor state β is:

$$P_{\nu_\alpha \to \nu_\beta} = \sin^2(2\theta) \sin^2\left(\frac{\Delta m^2 L}{4E}\right). \tag{2.7}$$

In conclusion it can be stated that the observation of neutrino oscillations is only possible if neutrinos have different rest masses and if their flavor and mass eigenstates are not identical. Meanwhile many experiments have established the neutrino oscillation scenario. A selection of the most important and most recent results are presented in the following three sections.

2.2.1 Solar Sector

The first experiments to indicate the presence of neutrino oscillations in the solar sector where the radiochemical experiments described above. The water Cherenkov detectors Kamiokande and Super-Kamiokande also detected solar neutrinos, in addition to their studies on atmospheric neutrinos [F+96, A+11b].

Due to the directional information, which these detectors offered, they were able to clearly identify the Sun as the dominant source of the measured ν_e flux. As elaborated above, the SNO experiment was the first one to give convincing evidence of flavor transitions in the solar sector.

Another approach towards the observation of neutrino oscillations and the determination of the parameters θ_{12} and Δm_{21}^2 was followed by the liquid scintillator experiment KamLAND[15]. It measured the $\overline{\nu}_e$ flux and spectrum from more than 50 Japanese nuclear power reactors through the detection of the inverse beta decay (see reaction 2.1). KamLAND was able to confirm the presence of neutrino oscillations and greatly improved the results on the mass squared difference Δm_{21}^2. Figure 2.1 shows the ratio of the $\overline{\nu}_e$ spectrum without background and geoneutrinos to the expectation in absence of oscillations as a function of L_0/E. L_0 is the effective baseline ($L_0 = 180$ km) which is the flux-weighted average of all individual baselines with respect to each reactor core. An undistorted reactor $\overline{\nu}_e$ energy spectrum is rejected at a level of more than $5\,\sigma$ [A$^+$08a].
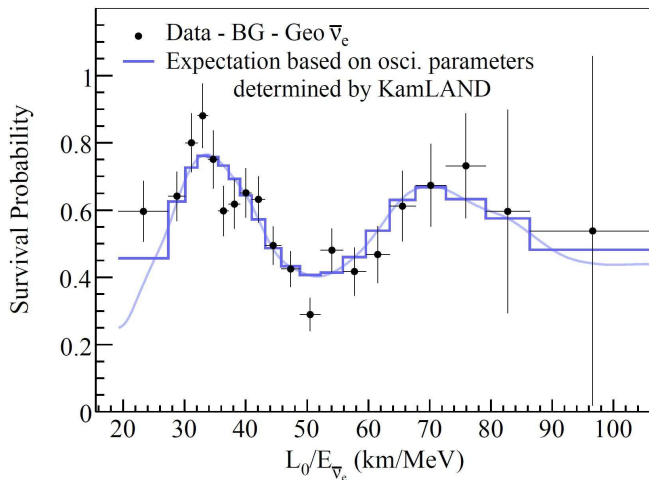
Figure 2.1: Ratio of the KamLAND $\overline{\nu}_e$ spectrum without background and geoneutrinos to the expectation in absence of oscillations as a function of L_0/E. L_0 is the effective baseline. The histogram and curve indicate the expectation accounting for individual baselines, time-dependent flux, and efficiencies (figure taken from [A$^+$08a]).

Figure 2.2 shows the contours of the allowed regions of the ($\tan^2\theta_{12}$, Δm_{21}^2) parameter space, resulting from a three-flavor neutrino oscillation analysis. It includes the data of the solar neutrino experiments SAGE [A$^+$09a], GALLEX [Kae07], GNO [A$^+$05], Homestake [C$^+$98], Borexino[16] [B$^+$11, B$^+$10], Super-Kamiokande [H$^+$06, C$^+$08, A$^+$11b] and SNO [A$^+$13f]. Furthermore, the

---

[15]Kamioka Liquid Scintillator Antineutrino Detector, Japan

[16]Italian diminutive form of BOREX which stands for Boron Solar Neutrino Experiment, LNGS
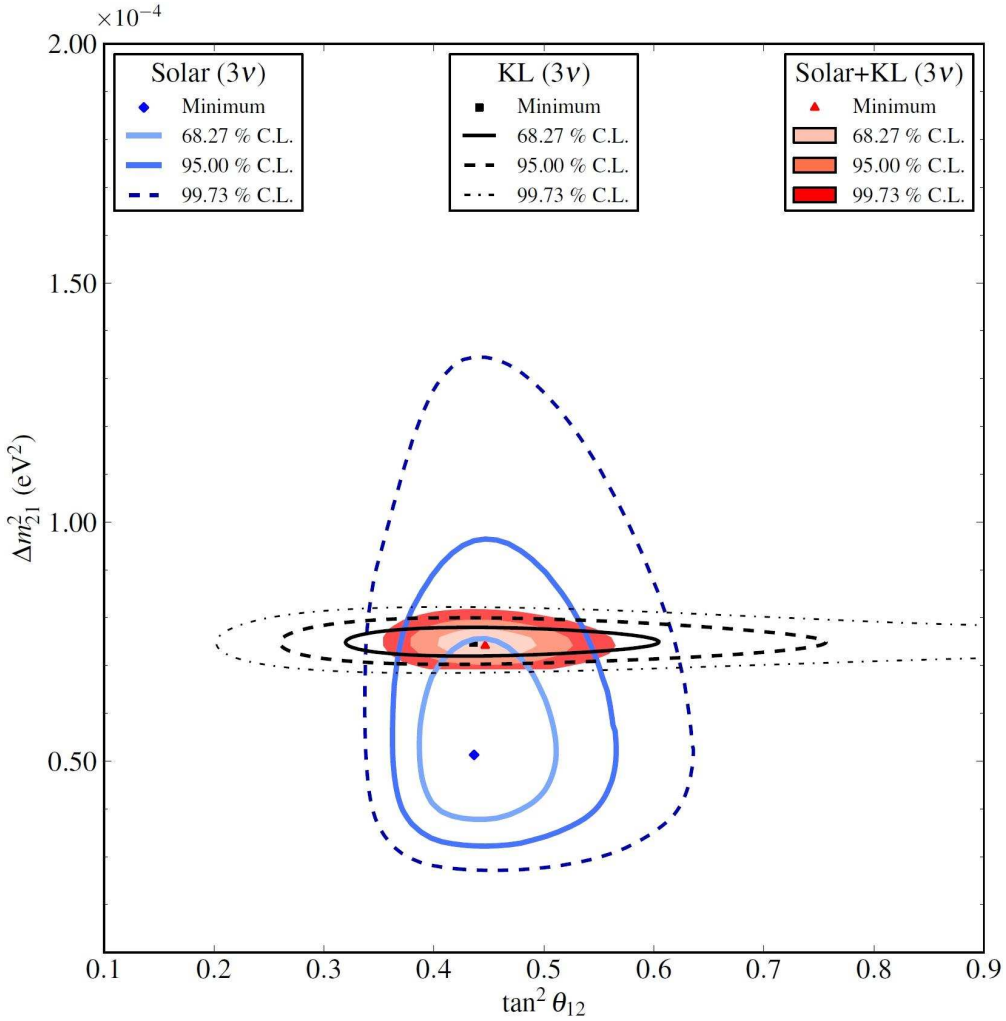
Figure 2.2: Contours of the allowed regions of the ($\tan^2 \theta_{12}$, Δm_{21}^2) parameter space resulting from a three-flavor neutrino oscillation analysis for different confidence levels (C.L.). The data of the solar neutrino experiments listed in the text (Solar), the KamLAND data (KL) and the combination of both (Solar+KL) are shown (figure taken from [A$^+$13f]).

results of the KamLAND experiment [G$^+$11] are shown, both separately and combined with the solar data. Table 2.1 lists the solar oscillation parameters resulting from a global fit with the available neutrino oscillation data as of June 2014. In addition to the experiments listed above, several more contribute to the three-flavor analysis (see [F$^+$14]), most notably the reactor experiments

Double Chooz[17] [A$^+$12b], Daya Bay[18] [Zha14] and RENO[19] [Seo14], and the accelerator experiments MINOS[20] [A$^+$13b, A$^+$13a] and T2K[21] [A$^+$14b, A$^+$14a].

Table 2.1: Solar oscillation parameters [F$^+$14]

Parameter	Best Fit $\pm\,1\,\sigma$	$2\,\sigma$ Range	$3\,\sigma$ Range
$\Delta m_{21}^2\;[10^{-5}\,\mathrm{eV}^2]$	$7.60^{+0.19}_{-0.18}$	7.26–7.99	7.11–8.18
$\sin^2\theta_{12}$	0.323 ± 0.016	0.292–0.357	0.278–0.375
θ_{12}	$34.6°\pm1.0°$	32.7°–36.7°	31.8°–37.8°

2.2.2   Atmospheric Sector

In 1998 the Super-Kamiokande experiment gave the first evidence of neutrino oscillations by measuring atmospheric neutrino fluxes. Its water Cherenkov detector is able to identify and distinguish electron and muon neutrino interactions. Additionally, it can determine the neutrinos' directions of flight. The Super-Kamiokande analysis showed a significant zenith angle dependent deficit of atmospheric muon neutrinos [F$^+$98]. While the number of detected ν_e was in accordance with the predictions, the number of ν_μ coming from below, i.e. the ν_μ crossing the entire diameter of the Earth before reaching the detector, was below the expected value. The ν_μ disappearance as a function of the baseline was explained by the process of $\nu_\mu \to \nu_\tau$ oscillations. These oscillations can also be studied by experiments detecting neutrinos that are produced artificially by the use of particle accelerators. Currently, the by far most precise values for the oscillation parameters in the atmospheric sector are coming from the accelerator experiments MINOS at Fermilab and T2K at J-PARC[22]. Both experiments generate a ν_μ beam and use near and far detectors to measure ν_μ disappearance and ν_e appearance. Furthermore, the MINOS neutrino beam can be switched to $\overline{\nu}_\mu$ production so that also $\overline{\nu}_\mu$ disappearance and $\overline{\nu}_e$ appearance can be studied. All experimental results strongly support the

---

[17]Double Chooz is the successor of the CHOOZ experiment, named after the town Chooz in Northern France.

[18]Daya Bay Reactor Neutrino Experiment, China, named after a bay of the South China Sea

[19]Reactor Experiment for Neutrino Oscillations, Yeonggwang, South Korea

[20]Main Injector Neutrino Oscillation Search, Fermilab

[21]Tokai to Kamioka, Japan

[22]Japan Proton Accelerator Research Complex, Tokai, Japan

oscillation scenario in the atmospheric sector [A$^+$14c, A$^+$14b]. In addition, MINOS was able to demonstrate that ν_μ and $\overline{\nu}_\mu$ oscillate analogously [A$^+$13b].

Although the OPERA experiment is not optimized for precision measurements on the mixing parameters, the detection of, up to now, four ν_τ candidate events (see Section 3.5) allows to limit the 90 % confidence interval for Δm_{32}^2 to $[1.8, 5.0] \times 10^{-3}\,\mathrm{eV}^2$ [A$^+$14g]. The results of experiments with higher precision are within this interval. Figure 2.3 depicts the contours of the allowed regions of the $(\sin^2\theta_{23}, \Delta m_{31}^2)$ parameter space according to MINOS, T2K and a global fit including also the Super-Kamiokande data. Since the sign of Δm_{32}^2 is yet unknown (see Section 2.3.1), both possible scenarios concerning the mass hierarchy are shown. The atmospheric oscillation parameters resulting from the global fit are listed in Table 2.2.
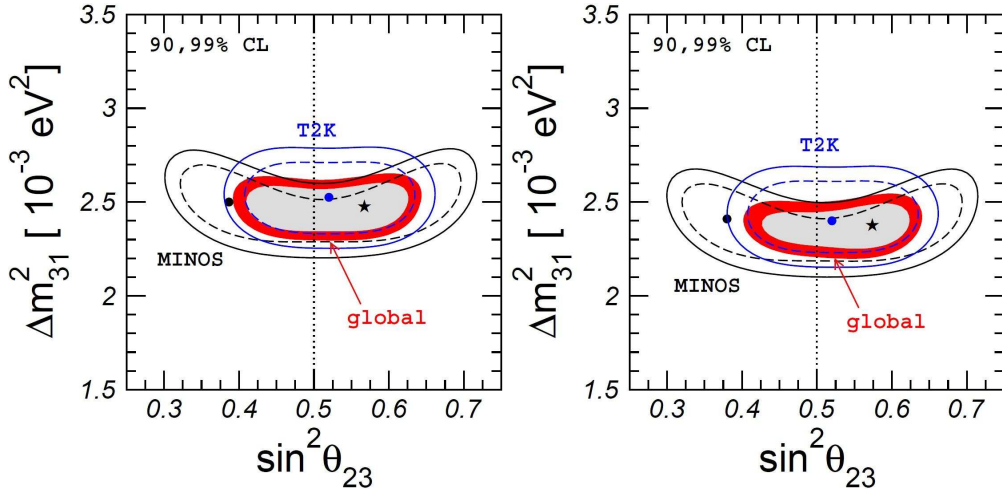
Figure 2.3: Contours of the allowed regions of the $(\sin^2\theta_{23}, \Delta m_{31}^2)$ parameter space according to MINOS, T2K and a global fit including the Super-Kamiokande data, shown for the normal (left) and the inverted (right) mass hierarchy. The inner contours correspond to the 90 %, the outer ones to the 99 % confidence level. The filled circles and the star mark the best fit values of MINOS/T2K and the global fit respectively (figure taken from [F$^+$14]).

Table 2.2: Atmospheric oscillation parameters for the normal mass hierarchy scenario (NH) and the inverted hierarchy (IH) [F⁺14]

Parameter	Best Fit $\pm\,1\,\sigma$	$2\,\sigma$ Range	$3\,\sigma$ Range
$\left\vert\Delta m_{31}^2\right\vert$ $[10^{-3}\,\mathrm{eV}^2]$ (NH)	$2.48^{+0.05}_{-0.07}$	2.35–2.59	2.30–2.65
$\left\vert\Delta m_{31}^2\right\vert$ $[10^{-3}\,\mathrm{eV}^2]$ (IH)	$2.38^{+0.05}_{-0.06}$	2.26–2.48	2.20–2.54
$\sin^2\theta_{23}$ (NH)	$0.567^{+0.032}_{-0.124}$	0.414–0.623	0.393–0.643
θ_{23}	$48.9°^{+1.8°}_{-7.2°}$	40.0°–52.1°	38.8°–53.3°
$\sin^2\theta_{23}$ (IH)	$0.573^{+0.025}_{-0.039}$	0.435–0.621	0.403–0.640
θ_{23}	$49.2°^{+1.5°}_{-2.3°}$	41.3°–52.0°	39.4°–53.1°

2.2.3   Mixing Angle θ_{13}

Until recently, the value of θ_{13} was unknown and the question, if it was non-zero at all, unanswered. Only an upper limit for the mixing angle was provided by the CHOOZ experiment [A⁺03a]. CHOOZ used a liquid scintillator detector to measure the $\overline{\nu}_e$ flux from a nuclear power plant in a distance of about 1 km.

In 2011 T2K found indications of $\nu_\mu \rightarrow \nu_e$ appearance and consequently a non-zero θ_{13} [A⁺11a]. Subsequent results from MINOS [A⁺11d] and Double Chooz[23] [A⁺12a] supported the T2K measurements and improved the precision. In March 2012 the Daya Bay collaboration published their observation of $\overline{\nu}_e$ disappearance with a significance of $5.2\,\sigma$ [A⁺12e]. At that time the experiment already had six liquid scintillator detectors at its disposal to measure the neutrino flux from six reactor cores at two different near and one far location.[24] Figure 2.4 shows the energy spectrum measured by the detectors in the far hall compared with the no-oscillation prediction from the measurements in the two near halls, clearly illustrating the $\overline{\nu}_e$ disappearance.

The RENO experiment follows a very similar experimental strategy: one near and one far liquid scintillator detector measure the $\overline{\nu}_e$ flux and spectrum from six reactor cores with almost the same thermal power as in Daya Bay

---

[23]Double Chooz uses a near and a far liquid scintillator detector. However, the near detector was only ready for commissioning in September 2014 and is therefore not part of the cited analyses.

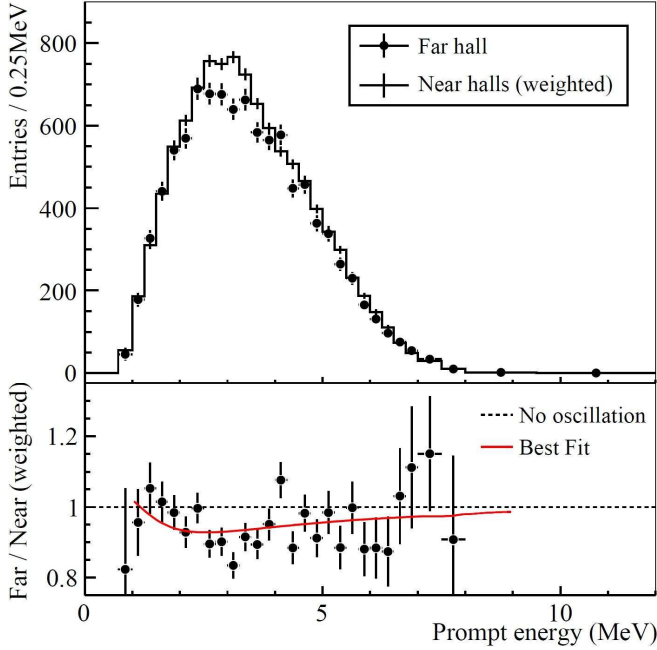[24]Two further detectors started taking data in October 2012.

Figure 2.4: Energy spectrum measured by the Daya Bay detectors in the far hall compared with the no-oscillation prediction from the measurements in the two near halls (top). The background has been subtracted from the spectra. Uncertainties are statistical only. The ratio of measured and predicted no-oscillation spectra is shown at the bottom (figure taken from [A+12e]).

and at comparable baselines. Just one month after the Daya Bay publication RENO announced a $4.9\,\sigma$ observation of a non-zero θ_{13} [A+12d].

Table 2.3 lists the values of the mixing angle θ_{13} for each of the two possible mass hierarchies resulting from a global fit analysis. It includes the data of all reactor neutrino experiments mentioned above as of June 2014 plus the results from KamLAND and Palo Verde[25].

Table 2.3: Mixing Angle θ_{13} for the normal mass hierarchy scenario (NH) and the inverted hierarchy (IH) [F+14]

Parameter	Best Fit $\pm\,1\,\sigma$	$2\,\sigma$ Range	$3\,\sigma$ Range
$\sin^2\theta_{13}$ (NH)	0.0226 ± 0.0012	0.0202–0.0250	0.0190–0.0262
θ_{13}	$8.6°^{+0.3°}_{-0.2°}$	$8.2°$–$9.1°$	$7.9°$–$9.3°$
$\sin^2\theta_{13}$ (IH)	0.0229 ± 0.0012	0.0205–0.0252	0.0193–0.0265
θ_{13}	$8.7°\pm0.2°$	$8.2°$–$9.1°$	$8.0°$–$9.4°$

---

[25]Palo Verde Neutrino Oscillation Experiment, USA [B+01]

2.3   Unresolved Issues in Neutrino Physics

Despite the remarkable progress made in the field of neutrino physics during
the past few decades, many open questions remain concerning the neutrino's
properties. One of the missing pieces of the puzzle will be contributed by
the OPERA experiment. Although the oscillation scenario as a whole is
well-established through a multitude of disappearance and appearance exper-
iments, the direct observation of $\nu_\mu \to \nu_\tau$ transitions on an event-by-event
basis was not accomplished before. The OPERA detector is unique in its
ability to resolve individual ν_τ events on a large scale. As of 2014 four τ
candidate events have been detected, corresponding to a significance of $4.2\,\sigma$
for ν_τ appearance (see Section 3.5). Since the analysis is still ongoing, the
significance of the final result may change, depending on potential improve-
ments in background reduction and whether further candidate events are found.

In the following sections the currently most pressing open questions in
neutrino physics are presented along with selected experiments aspiring to
answer them in the near future.

2.3.1   Mass Hierarchy

The values of the mass squared differences Δm_{21}^2 and Δm_{31}^2 are known
today at the level of a few percent, and various experiments are or will be
acquiring data to increase the precision. Nevertheless, the sign of the larger
of the two values, $\Delta m_{31}^2 = m_3^2 - m_1^2$, is yet unknown. As a consequence,
there are still two possibilities for the hierarchical order of the neutrino mass
eigenstates which are illustrated in Figure 2.5. The case in which ν_1, the mass
eigenstate with the highest ν_e content, is the lightest state is called normal hier-
archy and the order with ν_3 being the lightest state is called inverted hierarchy.

There are different possible approaches to determine the mass hierarchy
experimentally. For example, long-baseline accelerator experiments like
NOvA[26] seek to reach this goal by comparing ν_μ and $\overline{\nu}_\mu$ oscillations [A+07c].
Due to matter effects in the Earth the number of ν_e and $\overline{\nu}_e$, counted at the
far detector in a distance of $810\,\mathrm{km}$ from the neutrino source, is sensitive to
the mass hierarchy. However, for $\nu_\mu \to \nu_e$ / $\overline{\nu}_\mu \to \overline{\nu}_e$ oscillations this effect
may be masked depending on the value of the CP violating phase δ. Another
possibility to distinguish between normal and inverted hierarchy is to measure
the spectrum of reactor $\overline{\nu}_e$ with a high energy resolution of about $3\,\%$ in the

---

[26]NuMI Off-Axis ν_e Appearance, Fermilab. NuMI is the Fermilab neutrino beam. It stands
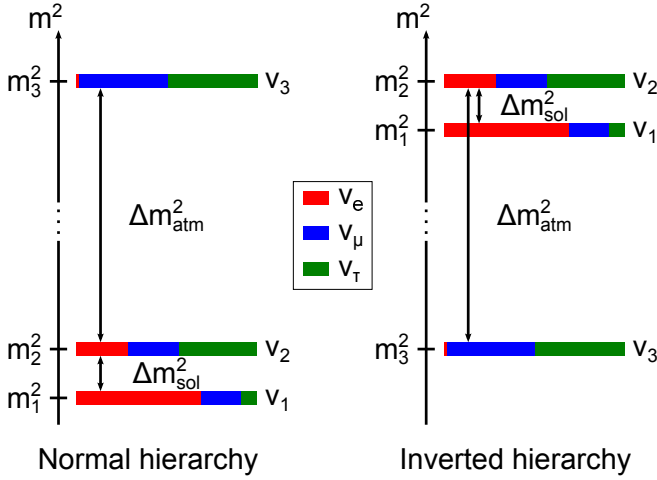   for Neutrinos at the Main Injector.

Figure 2.5: Mass squared spectra for the two possible mass hierarchies, the normal hierarchy (left) and the inverted hierarchy (right). The flavor composition of the three mass eigenstates is color-coded.

MeV-range. The $\overline{\nu}_e \rightarrow \overline{\nu}_e$ survival probability is slightly different for the two possible mass hierarchies. One of the experiments following this approach is JUNO[27], a 20 kt liquid scintillator detector currently in the early construction phase. It will be situated at an underground depth of 700 m and about 53 km away from two reactor complexes. JUNO strives to reach an energy resolution of better than 3 % at 1 MeV by improving the PMT[28] design and coverage with respect to current experiments, and by developing a highly transparent liquid scintillator with an attenuation length of more than 30 m. The first data taking is planed for 2020 [Li14].

2.3.2 CP Violation in the Leptonic Sector

The existence of CP violation in the quark sector is an established fact since the CP violating decay of the K_L^0 into two pions has been observed in 1964 [C+64]. Furthermore, CP violation was also observed in the neutral B meson system [A+01a]. However, it is still an open question if CP violation exists in the leptonic sector. If so, the size of the effect determines to what extend it may account for the matter-antimatter asymmetry in the universe.

Neutrino oscillations offer a method to probe CP symmetry on leptons. If a difference between the neutrino transition $\nu_\alpha \rightarrow \nu_\beta$ and the same process for the antineutrinos, $\overline{\nu}_\alpha \rightarrow \overline{\nu}_\beta$, is observed, then the symmetry must be violated. Nevertheless, depending on the actual mass hierarchy this difference may be increased or obscured by matter effects. One of the experiments

---

[27] Jiangmen Underground Neutrino Observatory, China

[28] Photomultiplier tube

currently searching for leptonic CP violation is NOvA. In September 2014 the construction of NOvA's near and far detector were completed and the experiment started taking data using a ν_μ beam. Later on, the beam will be switched to $\overline{\nu}_\mu$, enabling NOvA to investigate potential differences in the oscillation patterns.

A future generation of neutrino beams, the so-called neutrino factories, which are in an early research and development stage, will considerably improve the potential to study leptonic CP violation by means of neutrino oscillations. A neutrino factory consists of one or more racetrack-shaped muon storage rings with long straight sections pointing at distant detectors. The stored muons decay in flight, producing an intense and focused neutrino beam. Depending on the muons' charge the decay products are as follows:

$$\mu^- \rightarrow e^- + \overline{\nu}_e + \nu_\mu \qquad \text{or} \tag{2.8}$$

$$\mu^+ \rightarrow e^+ + \nu_e + \overline{\nu}_\mu. \tag{2.9}$$

Therefore, the neutrino factory offers the possibility to investigate oscillations of the type $\nu_e \leftrightarrow \nu_\mu$ or $\overline{\nu}_e \leftrightarrow \overline{\nu}_\mu$. Due to the high beam intensities, baselines of several thousand kilometers are possible. The design study for a neutrino factory is described in [A$^+$11c].

2.3.3   Sterile Neutrinos

In 2001 the short-baseline experiment LSND[29] has claimed the observation of a $\overline{\nu}_e$ access in its $\overline{\nu}_\mu \rightarrow \overline{\nu}_e$ appearance search [A$^+$01b]. This result cannot be explained in the context of a three-neutrino framework without contradicting the results of various other oscillation experiments. As a solution to this problem a fourth type of neutrino was postulated, a so-called sterile neutrino which does not take part in the weak interaction but which may mix with the three active neutrino types.

To probe the LSND parameter space, the MiniBooNE[30] experiment was built at Fermilab, using the same ratio of baseline to neutrino energy of about $1\,\text{m/MeV}$. In 2013 an analysis was published, showing a $2.8\,\sigma$ excess for $\overline{\nu}_e$ appearance and an excess of $3.4\,\sigma$ for ν_e appearance. The MiniBooNE results for both neutrinos and antineutrinos are partially compatible with a two-neutrino oscillation model based on the LSND measurements, where an electron type neutrino transforms to a sterile neutrino [AA$^+$13]. However,

---

[29]Liquid Scintillator Neutrino Detector, Los Alamos National Laboratory, USA

[30]BooNE: Booster Neutrino Experiment

various experiments do not confirm this type of oscillation but instead exclude parts of the parameter space for a potential sterile neutrino. Among these experiments are KARMEN[31] [A+02], NOMAD[32] [A+03b] and also OPERA (see Section 3.5). But even all exclusion limits combined do not completely rule out the existence of one or more sterile neutrinos (see Figure 3.21). To resolve the tensions between the different experimental results, further data covering the parameter space in question is necessary. One experiment that will deliver such data is MicroBooNE, a 170 t Liquid Argon Time Projection Chamber currently assembled at Fermilab. Its physics goals include the investigation of the ν_e appearance excess signals [C+07]. Another strategy to probe non-standard oscillations is to place a strong artificial ν_e or $\overline{\nu}_e$ source near or inside a large liquid scintillator detector with the capability to detect low energy electron neutrinos/antineutrinos. For the SOX[33] experiment the use of a ^{51}Cr ν_e source and a ^{144}Ce/^{144}Pr $\overline{\nu}_e$ source is planned. The Borexino detector, which has proven its excellent background reduction capabilities by the recent observation of solar pp neutrinos [B+14a], will then measure a possible $\nu_e/\overline{\nu}_e$ disappearance signal and could resolve the minima and maxima of the hypothetical sterile neutrino oscillations within its detector volume [B+13].

2.3.4   Absolute Neutrino Mass

While the neutrino mass squared differences Δm^2 are known today (see Tables 2.1 and 2.2), the absolute mass values have not yet been determined. There are several different methods for a direct mass measurement. The most promising one for the near future is the precise measurement of the endpoint region of a β decay spectrum. A non-zero neutrino mass implies a kinematical effect on the electron emitted during the decay, caused by the escaping electron antineutrino. The KATRIN[34] experiment is designed to measure the spectrum of electrons from the β decay of tritium with very high precision. A special type of spectrometer, a so-called MAC-E Filter[35], serves as an adjustable energy filter for the electrons, allowing to scan the spectral shape close to the decay's endpoint energy. KATRIN will be sensitive to a neutrino mass down to 0.2 eV [Wol10]. Its predecessor experiments in Mainz and Troitsk, both using the same measurement technique, provided an upper limit for the $\overline{\nu}_e$ mass of

---

[31] Karlsruhe Rutherford Medium Energy Neutrino Experiment, Rutherford Appleton Laboratory, United Kingdom

[32] Neutrino Oscillation Magnetic Detector, CERN

[33] Short distance neutrino Oscillations with Borexino

[34] Karlsruhe Tritium Neutrino Experiment, Germany

[35] Magnetic Adiabatic Collimation combined with an Electrostatic Filter

2.3 eV and 2.2 eV respectively [K$^+$05, A$^+$11f].

Another strategy is pursued by experiments investigating electron capture decays on ^{163}Ho. Electron capture is a type of radioactive decay where a proton-rich nucleus absorbs an electron from one of the inner electron shells. A proton captures the electron and is converted into a neutron, while an electron neutrino is emitted:

$$p^+ + e^- \rightarrow n + \nu_e. \tag{2.10}$$
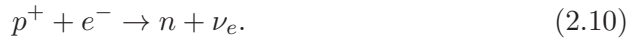
After this process the atom is in an excited state. The mass of the neutrino can be deduced from its influence on the measured de-excitation energy spectrum. Several experiments on this subject, e.g. ECHo[36] and HOLMES[37], are being developed with a planned neutrino mass sensitivity in the sub-eV range [G$^+$14, A$^+$14h].

An upper limit on the sum of the neutrino masses can be obtained from cosmological observations like large-scale structure surveys of the universe or the measurement of the cosmic microwave background. These analyses currently deliver the lowest neutrino mass limits but are highly dependent on the cosmological models. The most recent data comes from the Planck space telescope. A combination with previous experimental data yields an upper limit of 0.23 eV (95 % confidence level) for the neutrino mass sum [A$^+$14d].

2.3.5   Nature of the Neutrino, Majorana/Dirac

A further, yet unanswered question about the neutrino concerns its fundamental nature. According to current knowledge there is no additive quantum number with a non-zero value carried by the neutrino. Therefore, the neutrino may be a Majorana particle, i.e. identical to its own antiparticle, unlike all other fermions in the Standard Model which are Dirac particles. The process of the neutrinoless double β decay offers a possibility to probe the neutrino's nature. The decay can only exist if neutrinos have a non-vanishing mass and are Majorana particles. One of various experiments dedicated to searching for this decay is GERDA[38]. The first phase of the experiment was completed in 2013. So far, no signal was observed and the half-life of a potential neutrinoless double β decay is now limited to at least 2.1×10^{25} years (90 % confidence

---

[36] Electron Capture ^{163}Ho Experiment, Heidelberg, Germany

[37] The Electron Capture Decay of ^{163}Ho to Measure the Electron Neutrino Mass with sub-eV sensitivity, Milan, Italy

[38] Germanium Detector Array, LNGS

level) [A$^+$13e].

The KamLAND-Zen[39] collaboration published a slightly tighter limit of 2.6×10^{25} years (90 % confidence level) for the half-life of the decay [A$^+$14i]. As double β decay source the experiment uses ^{136}Xe which is dissolved in liquid scintillator and contained inside a small nylon vessel. This vessel is placed in the center of the already existing KamLAND detector. Several enhancements of the experiments sensitivity are planed for the future, e.g. an increase of the xenon mass and an upgrade of the light collection system.

COBRA[40] is another experiment on this topic and is currently under development. In contrast to GERDA it will not use germanium as source and detector, but instead semiconductor crystals consisting of cadmium zinc telluride. The COBRA crystals contain a total of nine isotopes that are double β decay candidates. The experiment will also profit from its highly granular setup allowing for coincidence analyses as a further background rejection method [E$^+$13].

---

[39]KamLAND Zero Neutrino Double Beta Decay Search

[40]Cadmium Zinc Telluride 0-Neutrino Double-Beta Research Apparatus, LNGS

Chapter 3

The OPERA Experiment

The main scientific goal of the OPERA experiment is to give conclusive evidence for the oscillation of ν_μ to ν_τ on an event-by-event basis. With the detection of individual ν_τ interactions in a pure ν_μ beam at a long baseline, the appearance of oscillated ν_τ can directly be shown. To achieve this objective, two conflicting challenges have to be met: The tiny neutrino interaction cross section at energies in the GeV range calls for a large and massive target. But then the detection of τ leptons, originating at the ν_τ interaction vertex and having a mean lifetime of only $cT = 87.03\,\mu$m [O$^+$14], require a spatial resolution not exceeding a micrometer.[1] For OPERA, lead with a total mass of 1.25 kt was chosen for a target and nuclear emulsions for a cost-effective, large-area particle detector with sub-micrometer spatial and mrad angular tracking resolution. To obtain a tracking capability throughout the whole target area, thin sheets of lead and emulsions are stacked alternately, forming a structure called Emulsion Cloud Chamber (ECC). Since emulsions are a passive detector type, a hybrid detector design with additional electronic detector components is necessary for real-time triggering and vertex finding of neutrino interactions in the target. In order to achieve the highest possible significance for the oscillation search, all available ν_τ decay channels have to be analyzed. For the kinematic analysis in the muonic decay channel and for the background rejection of charmed hadron decays originating from ν_μ interactions, the capability to measure the muon's momentum and to identify the sign of its charge is essential. Therefore, a magnetic spectrometer is integrated into the detector design. Finally, the requirements for the neutrino beam are: an energy above the tau production threshold of 3.4 GeV, a long-baseline for a significant oscillation probability and the highest possible beam intensity for a maximum number of neutrino interactions in the detector.

---

[1] T is the eigentime.

3.1   The CNGS Neutrino Beam

The neutrinos are produced at CERN, near Geneva, Switzerland, and travel
730 km through the earth to the LNGS underground laboratory, close to the
city of L'Aquila, Italy, where the OPERA detector is located (see Figure 3.1).
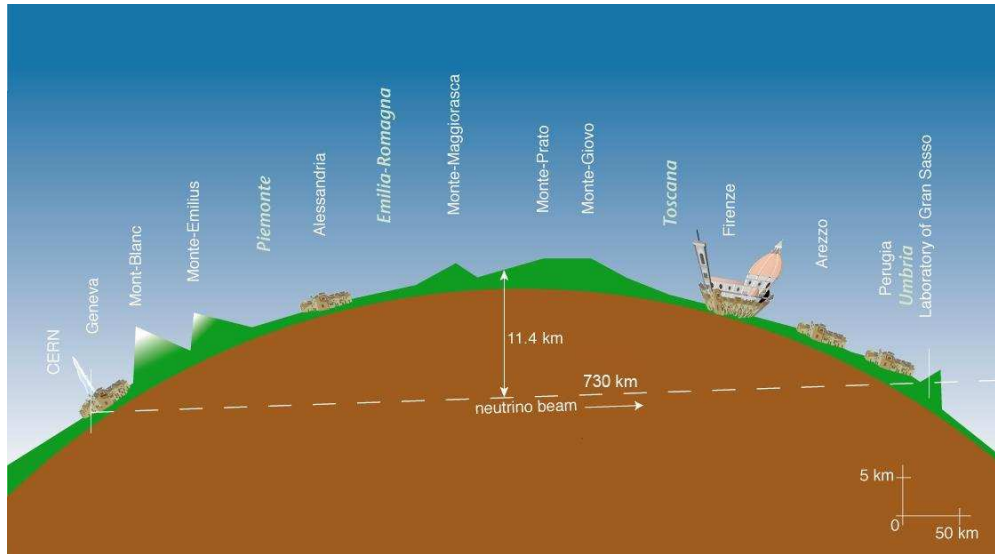For the production of the neutrino beam, protons with an energy of 400 GeV

Figure 3.1: Illustrative graphic of the neutrino flight path through the earth from
CERN to the LNGS (figure adapted from [CNG14])

are extracted from the SPS[2] accelerator and directed downwards by means of
dipole magnets to hit a carbon target (see Figure 3.2).   For each CNGS cycle
the entire content of the SPS is emptied in two fast extractions, which are each
10.5 µs in length and separated by 50 ms. The length of one full CNGS cycle
is six seconds. Since the SPS accelerator is shared among several experiments
(LHC[3] filling, fixed target experiments) and due to practical and legal limita-
tions on the radiation level reached in the underground beam facilities, the time
between two CNGS cycles is variable and of the order of a few tens of seconds.
The beam intensity is expressed in terms of the number of protons reaching
the CNGS target (p.o.t.[4]), the maximum being 3.5×10^{13} p.o.t. per CNGS cycle.

The proton beam is focused to a diameter of 0.5 mm (standard deviation)
onto the target, which consists of an array of air-cooled graphite rods. The

---

[2] Super Proton Synchrotron

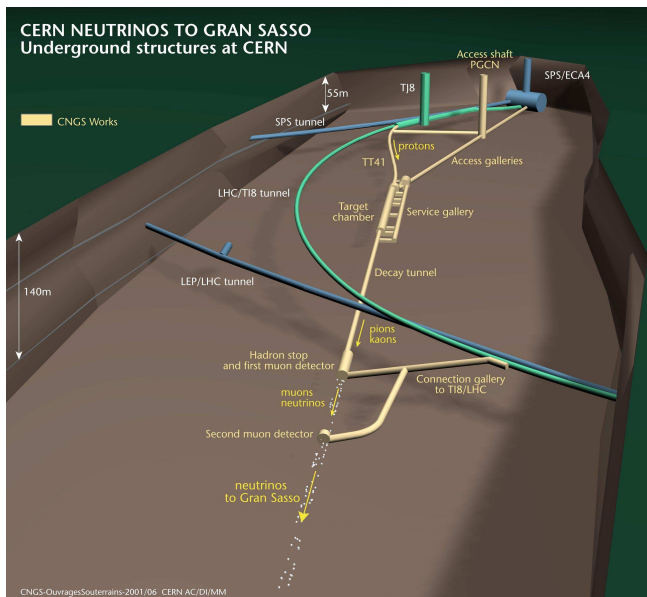[3] Large Hadron Collider

[4] protons on target

Figure 3.2: CNGS underground structures. The beamline TT41 delivers the protons coming from the SPS accelerator to the CNGS target chamber (figure adapted from [CNG14]).
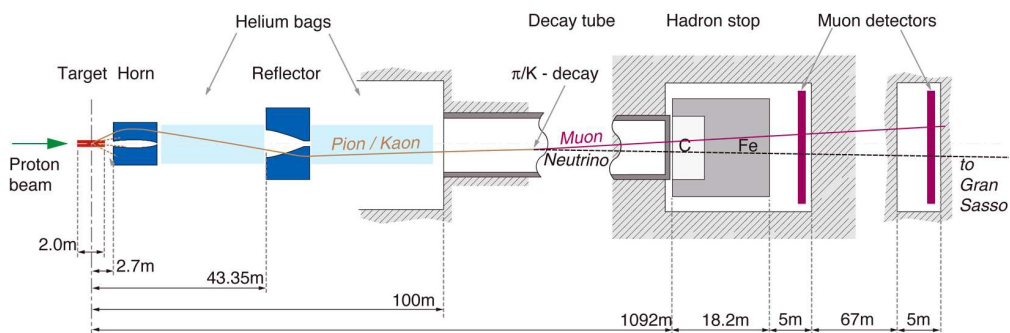

Figure 3.3: Main components of the CNGS target area (figure taken from [CNG14])

interactions of the protons with carbon nuclei in the target produce mainly π^+ and K^+, which are focused in a wide energy range by a system of two magnetic lenses (see Figure 3.3). The first lens, the so-called horn, focuses positive particles with energies around 35 GeV and defocuses all negatively charged ones. Lower energetic particles, which are overfocused, as well as particles with energies greater than 35 GeV, which are insufficiently deflected by the horn, are focused by the second lens, called reflector. Particles that are already aligned with the beam direction can pass the reflector through its large aperture without the risk of further interactions in the material. Horn and reflector are pulsed synchronized with the proton extractions with currents of 150 kA and 180 kA respectively. To dissipate the thermal energy coming from particle interactions in the metal and from the applied electrical currents, both structures are water cooled. Downstream of the reflector the particles

enter the decay tunnel, a steel tube, $2.45\,\text{m}$ in diameter and $992\,\text{m}$ long, which is evacuated to less than $1\,\text{mbar}$ pressure to minimize the probability of secondary interactions. For the same reason the space behind each of the magnetic lenses is occupied by a helium-filled tube, reducing the number of interactions as compared to an air-filled space. The π^+ and K^+ decay in flight, the desired decay product being the ν_μ, which is accompanied by a μ^+. Table 3.1 lists all relevant decay modes. An unavoidable contamination of the beam with neutrinos of the wrong kind is coming from the decays of π^-, K^- and μ^+, the latter decaying into e^+, ν_e and $\overline{\nu}_\mu$ with a branching ratio of nearly $100\,\%$ [O$^+$14]. The contaminations relative to the ν_μ content of the beam are listed in Table 3.2 in terms of CC interactions with an isoscalar[5] target. For OPERA, being a ν_τ appearance experiment without a near detector, the most important point is a possible beam contamination with ν_τ. Next to the π^+ and K^+, the proton interactions in the CNGS target produce a small fraction of D_s mesons, of which $(5.6 \pm 0.4)\,\%$ decay in the τ channel [O$^+$14]. The resulting ν_τ content of the neutrino beam at production is expected to be below 10^{-6} [F$^+$07b]. Considering the opening angle of the beam, the baseline and the ν_τ cross sections, the number of ν_τ CC interactions in the OPERA target originating from the beam contamination is negligible [A$^+$09b].

Table 3.1: Decay modes of π^+ and K^+ with branching ratios above 10^{-2} [O$^+$14]. All further decay modes are strongly suppressed and are not considered here.

Decay Mode	Branching Ratio [%]	
$\pi^+ \to \mu^+\nu_\mu$	99.98770	$\pm\, 0.00004$
$K^+ \to \mu^+\nu_\mu$	63.55	$\pm\, 0.11$
$K^+ \to \pi^+\pi^0$	20.66	$\pm\, 0.08$
$K^+ \to \pi^+\pi^+\pi^-$	5.59	$\pm\, 0.04$
$K^+ \to \pi^0 e^+\nu_e$	5.07	$\pm\, 0.04$
$K^+ \to \pi^0 \mu^+\nu_\mu$	3.353	$\pm\, 0.034$
$K^+ \to \pi^+\pi^0\pi^0$	1.761	$\pm\, 0.022$

Protons, which did not interact with the target, as well as pions and kaons, which did not decay up to the end of the decay tunnel, are absorbed in a massive block of carbon and iron, called hadron stop (see Figure 3.3). Directly behind this structure and also about $70\,\text{m}$ further downstream are muon detectors for real-time monitoring of the beam alignment. The orientation

---

[5] An isoscalar nucleus has the same number of protons and neutrons.

Table 3.2: CNGS beam contamination with ν_e, ν_τ and antineutrinos in terms of CC interactions with an isoscalar target. The intrinsic ν_τ contamination of the beam is expected to be below 10^{-6} [F+07a].

Contaminant	Relative Contamination
ν_e/ν_μ	0.89 %
$\overline{\nu}_\mu/\nu_\mu$	2.4 %
$\overline{\nu}_e/\nu_\mu$	0.06 %
ν_τ/ν_μ	negligible

of the neutrino beam axis is defined by the $-5.6\,\%$ slope of the beamline, delivering the protons to the CNGS target. For fine tuning the neutrino beam, the focal point of the proton beam on the target and the target itself can be shifted. All other components of the CNGS facility are not movable and can therefore not be used to align the beam in direction of the Gran Sasso.

The muons are absorbed within a few hundred meters of rock, while the neutrinos travel through the earth towards the LNGS. The average ν_μ energy at the OPERA detector is $17.9\,\mathrm{GeV}$ [F+07a].

The CNGS beam has been in operation for five years, from 2008 until 2012, with a total of 17.97×10^{19} p.o.t. and $19\,505$ recorded neutrino interactions in the detector's targets [A+14e]. The expected number of detected ν_τ events in OPERA is around five. Due to the smallness of this signal, a passive shielding of the detector against the constant atmospheric particle shower is indispensable.

3.2   The OPERA Detector

The OPERA detector is located in one of the three large experimental halls of the LNGS, an underground laboratory below the Gran Sasso massif, connected to the highway tunnel between the cities of L'Aquila and Teramo, Italy (see Figure 3.4). $1400\,\mathrm{m}$ of rock overburden, featuring a shield against particles equivalent to $3800\,\mathrm{m}$ of water, reduce the atmospheric muon flux in the laboratory to about one muon per square meter and hour [Vot12].

The detector is composed of two almost identical sections called Super Modules (SM). In the direction of the CNGS beam, SM 1 is located in front of SM 2 (see Figure 3.5). Each SM has an instrumented target section, containing the lead/emulsion target with micrometer tracking capability, as well as planes
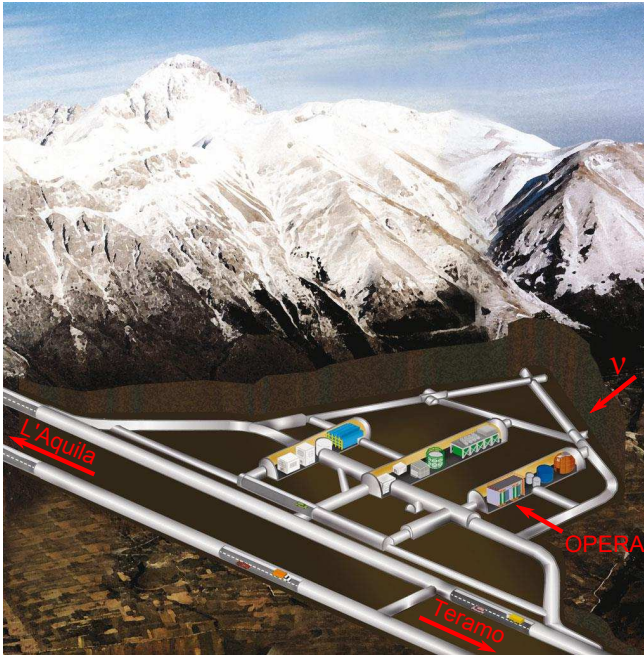
Figure 3.4: LNGS underground laboratory. The OPERA detector is located in the eastern experimental hall. The CNGS beam neutrinos enter the laboratory from the northwest. 1400 m of rock overburden provide a shield equivalent to 3800 m of water (figure adapted, source: LNGS).

of plastic scintillator detectors, called Target Tracker, for a coarse real-time tracking of charged particles. Behind each target is a magnetic spectrometer with a dipole magnet whose two vertical walls are instrumented with Resistive Plate Chambers (RPCs). Upstream and downstream of each magnet wall are the drift tube planes of the Precision Tracker, providing the tracking information for the determination of the particles' charge and momentum. Two large RPC planes in front of SM 1 act as a veto detector against charged particles reaching the target in beam direction. Most of the electronics for the detector control and readout, as well as the various power supplies are located on a platform on top of the OPERA detector.

The different detector parts and their functions are described in the following sections. A more detailed description of the OPERA detector can be found in [A$^+$09b].

3.2.1   Lead/Emulsion Target

Nuclear emulsions are used as a detector for charged particles since about 100 years. Their spatial resolution is less than a micrometer, which is an order of magnitude smaller compared to state of the art silicon pixel detectors at a fraction of the cost. Since a surface of more than $100\,000\,\mathrm{m}^2$ is covered by the emulsions in OPERA, the cost per m^2 becomes a crucial factor.
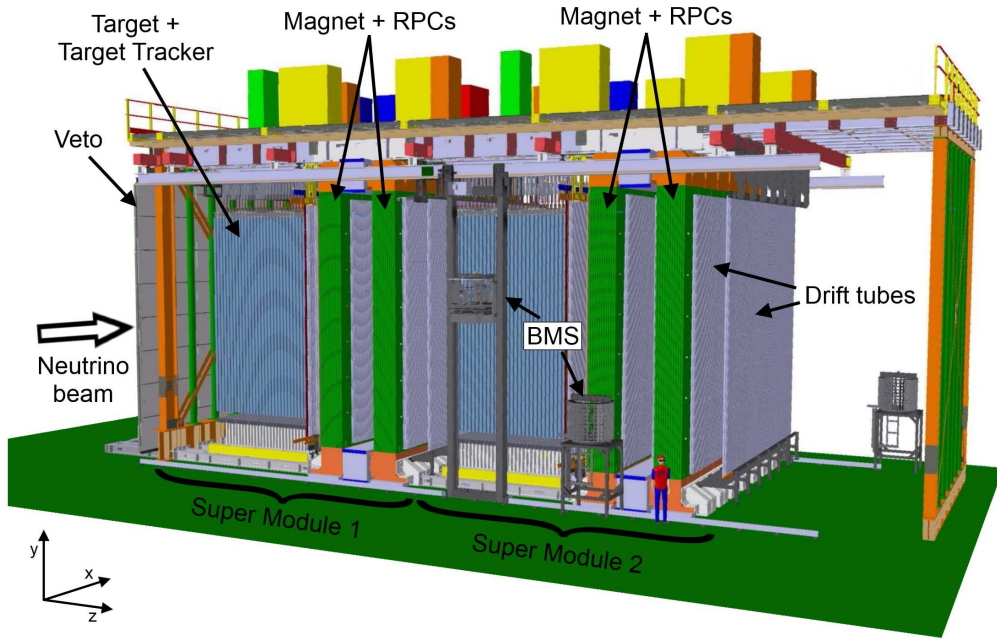
Figure 3.5: Main components of the OPERA detector (figure adapted from [A⁺06a])

Chemically, a nuclear emulsion is a colloidal suspension of silver halide crystals in gelatin. The OPERA emulsions contain silver bromide (AgBr) crystals. Unlike in photographic film, the crystals in nuclear emulsions are uniform in size with a diameter of about $0.2\,\mu m$ [N⁺06].[6] A prerequisite for the functioning of the emulsions as a tracking detector is the presence of point defects in the AgBr crystal lattice, locally lowering the crystal's conduction band. These impurities act as traps for electrons that are set free by the ionization processes induced by charged particles crossing the crystal. The negative electric charge at the site of the electron trap attracts interstitial Ag^+ ions which recombine with the electrons to metallic silver. After the recombination of e^- and Ag^+ to neutral Ag, further electrons may be captured by the same impurity and the process repeats until the charge in the crystal is neutralized. Clusters of at least four Ag atoms serve as so-called latent image centers. These clusters are enlarged during the chemical development process, where a reducing agent provides a large number of electrons, so that the silver clusters grow by several orders of magnitude and eventually become visible under an optical microscope.

---

[6] In photographic emulsions different grain sizes are used for a softer contrast. Larger crystals have a higher sensitivity to light than smaller ones.

The OPERA target is segmented into small units called ECC bricks, which can be extracted individually from the target area and analyzed shortly after an interaction took place. Each brick contains 57 emulsion films interleaved with 56 plates of 1 mm thick lead. An emulsion film consists of a 205 μm thick plastic base with 44 μm thick emulsion layers on each side. The lead/emulsion stack is tightly packed inside a black plastic box, which is wrapped light-tight in aluminum tape (see Figure 3.6). On the downstream-side of the brick a
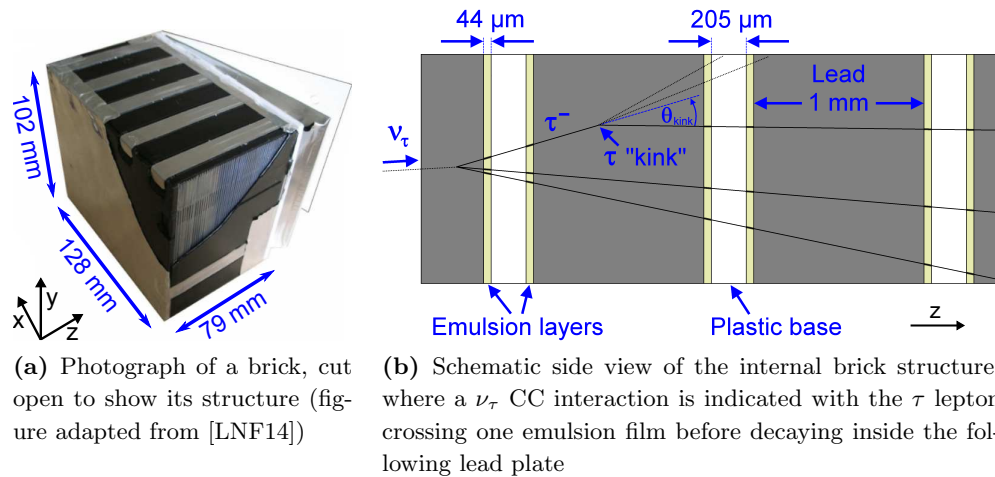

(a) Photograph of a brick, cut open to show its structure (figure adapted from [LNF14])

(b) Schematic side view of the internal brick structure, where a ν_τ CC interaction is indicated with the τ lepton crossing one emulsion film before decaying inside the following lead plate

Figure 3.6: Each ECC brick contains 57 emulsion films interleaved with 56 lead plates of 1 mm thickness, packed inside a black plastic box with light-tight aluminum wrapping. The so-called Changeable Sheets are packed separately and placed inside a white plastic box, attached to the downstream-side of the brick. For the photograph (a) this box has been opened. An emulsion film consists of a 205 μm thick plastic base with 44 μm thick emulsion layers on both sides (b).

white plastic box is attached, containing two additional films packed separately in aluminum-laminated paper (see Figure 3.6a). These emulsion films are called Changeable Sheets (CS). They serve as an interface between the brick and the electronic detectors. A brick has a size of $128 \times 102 \, \text{mm}^2$ transverse to the beam direction and a longitudinal size of 79 mm, corresponding to $10 \, X_0$. The total mass of a brick is 8.3 kg.

The ECC bricks are housed in an ultra-light grid-like structure made of stainless steel. It consists of 31 walls per SM which are oriented perpendicular to the beam direction. Each wall has 64 rows and 52 columns. Accordingly, the target areas have a capacity to hold a total of more than 200 000 bricks. Due to funding issues, the number of bricks was reduced by about 25 % as compared to the experiment proposal [G$^+$00]. 150 000 bricks with a total mass of about 1.25 kt were produced. They are arranged in a symmetrical and compact pattern in the target areas of both SMs to balance the load on the

brick support structure. The bricks are handled by two robotic devices, one on each side of the detector, the so-called Brick Manipulator System (BMS). The initial filling of the target was carried out by the BMS, and since the beginning of the physics runs the BMS extracts ECC bricks that are tagged for a vertex search.

3.2.2 Target Tracker

The brick walls are interleaved with planes of plastic scintillators called Target Tracker (TT). In total, there are 62 TT walls, each consisting of two segmented scintillator planes, one with a horizontal and one with a vertical readout. Each plane is composed of 4×64 strips that are $6.86\,\text{m}$ long, $26.3\,\text{mm}$ wide and $10.6\,\text{mm}$ thick (see Figure 3.7). The strips are equipped with wavelength shifting (WLS) fibers that are glued into a milled groove along the full length of the strip. The WLS fibers are read out on both sides by 64-channel PMTs [A+07a].

The TT's main purpose is the real-time detection of outgoing charged particles from a neutrino interaction in the lead/emulsion target, to identify the candidate ECC brick. Additionally, the TT serves as a coarse hadronic
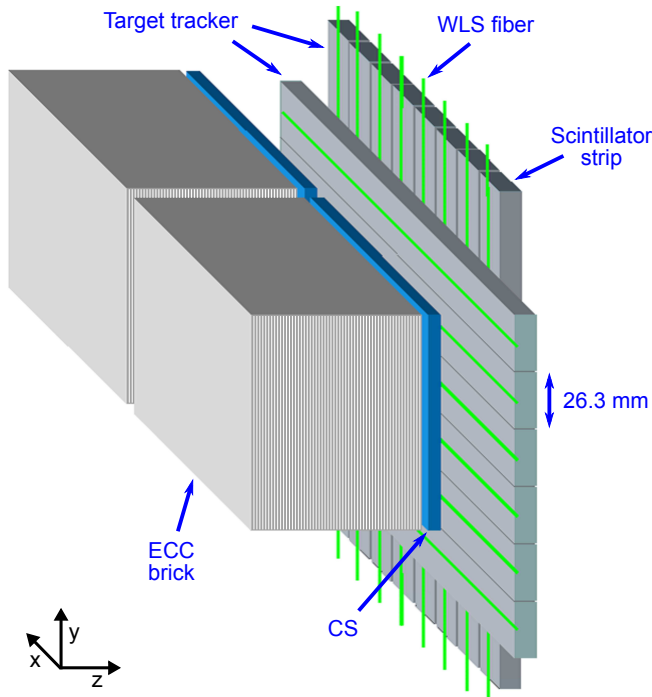

Figure 3.7: Schematic drawing of the target tracker (figure adapted from [A+08b])

sampling calorimeter. The PMT signals are recorded by ADCs[7]. The energy deposited in a scintillator plane is derived from the number of photoelectrons which in turn is calculated from the number of ADC counts and the gain of the corresponding PMT channel [A+11e].

3.2.3   Muon Spectrometer

Each of the two target sections is followed by a muon spectrometer consisting of a large dipole magnet, 24 RPC planes and six drift tube walls. The magnet walls and all electronic detector planes are oriented perpendicular to the beam direction and extend at least 40 cm beyond the target in all transverse directions. The main purpose of the two spectrometers is the identification of muons and the determination of their momentum and charge. This is essential to exploit the muonic τ decay channel for the oscillation analysis and to reduce the background from charmed hadron decays originating from ν_μ interactions.

Dipole Magnet

The magnet is composed of two vertical magnet arms, the top and the bottom flux return yoke (see Figure 3.8). Each arm consists of twelve layers of iron slabs with a thickness of 5 cm that are bolted together leaving 2 cm wide gaps between them to house eleven RPC planes. A copper coil is wound around each of the two steel return yokes. The magnets are operated at a current of 1600 A, resulting in an average magnetic field of 1.53 T [A+09b]. The nominal field polarization is pointing up in the first magnet arm and down in the second one. Therefore, a negatively charged particle traveling in beam direction is deflected horizontally to the left in the first arm and to the right in the second one. The polarization of both magnets was inverted during the 2012 beam run to identify possible systematic effects.

RPCs

The RPCs' main task is to track particles inside the magnet arms and to provide the drift tube detector with a trigger signal (see Chapter 4). The RPC detector offers a 3D tracking with a spatial resolution of about 1.5 cm [B+09a]. The drift tubes, on the other hand, have a much higher intrinsic spatial resolution but are only sensitive in the horizontal plane (x- and z-coordinate, see Figure 3.5). In order to achieve the desired track resolution with the

---
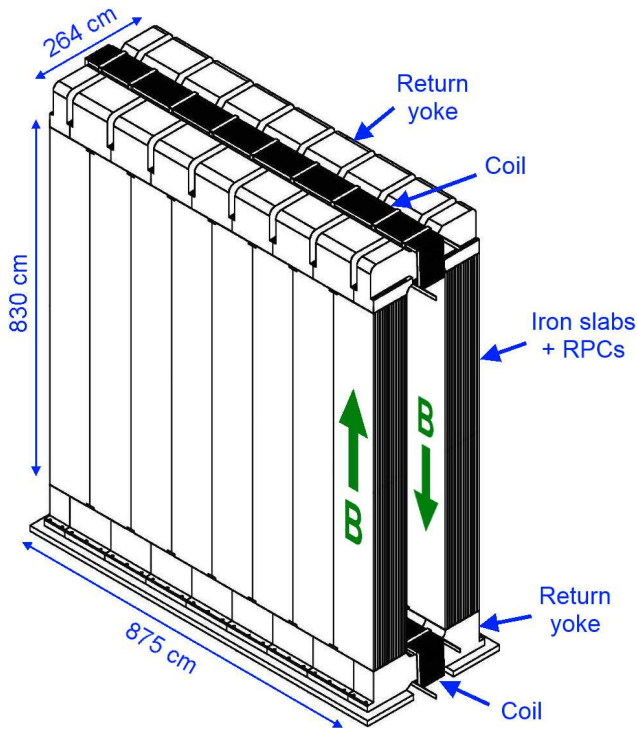
[7] Analog-to-digital converter

Figure 3.8: Schematic drawing of an OPERA dipole magnet. The magnetic field vector B is pointing in opposite directions in the two magnet arms (figure adapted from [AF$^+$07]).

Precision Tracker, an estimate of the corresponding y-coordinates is essential (see Chapter 4). This information is mainly provided by the RPCs. And while the momentum of particles crossing a spectrometer is determined by the Precision Tracker, the momentum of muons stopping inside the first magnet arm can be estimated using the RPCs.

The OPERA RPCs are made up of two parallel Bakelite electrodes, 2 mm thick and kept 2 mm apart by means of Lexan[8] spacers that are installed in a 10 cm lattice configuration throughout the RPCs (see Figure 3.9). The chambers are sealed by a hot melt adhesive and filled with a gas mixture composed of $Ar/C_2H_2F_4/iso-C_4H_{10}/SF_6$ in the volume ratios 75.4/20.0/4.0/0.6 [M$^+$07]. The electrodes have a volume resistivity greater than $5 \times 10^{11}\,\Omega$cm at a temperature of $20°$C. Their inner surface is coated with a layer of polymerized linseed oil in order to smooth the Bakelite's surface roughness and thus reduce the dark current. The electrodes' outer surface is coated with graphite. These layers have a high surface resistivity (about $100\,k\Omega/\square$) and are used for the connection of the high voltage supply. A voltage of 5.7 kV is applied to the graphite layers.[9] As an electrical insulator, a $440\,\mu$m PET[10] layer covers

---

[8] Polycarbonate, trademark by the manufacturer SABIC

[9] The high voltage was lowered from an initial value of 5.8 kV during the 2008 run [Pao14].
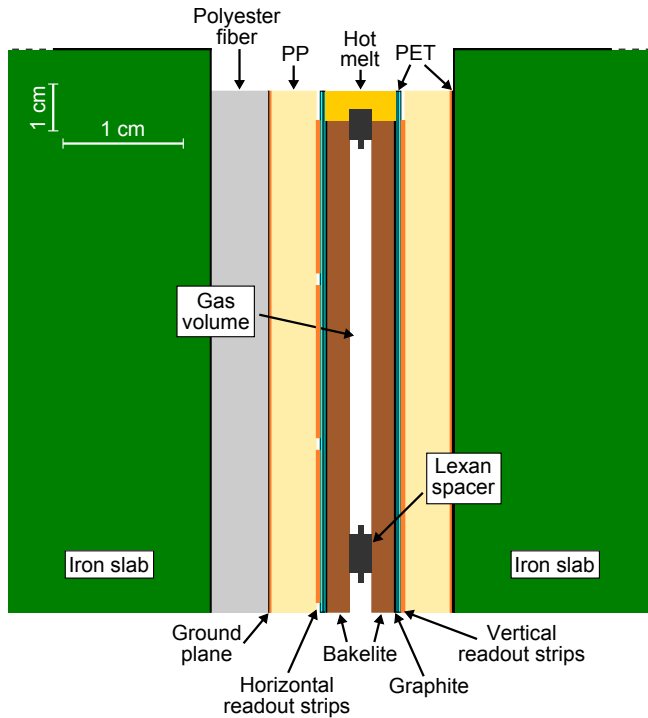
[10]Polyethylene terephthalate

Figure 3.9: Schematic side view of an OPERA RPC, installed inside a magnet arm in the 2 cm wide space between two iron slabs. For a better visualization of the thin vertical layers, the horizontal scale is expanded as compared to the vertical one.

the graphite.[11] Copper readout strips are glued to 4 mm thick PP[12] sheets. On one side of the chamber, 3.5 cm wide and 8.7 m long strips are oriented horizontally, on the other side the strips are 2.6 cm wide, 8.0 m long and are oriented vertically. The exterior surface of the PP sheets is covered with a continuous copper sheet acting as ground plane. The remaining space in the gap between the iron slabs is filled with a slightly compressed polyester fiber pad.

Each individual RPC is 2.91 m wide and 1.134 m high. An RPC plane is composed of 21 of these chambers arranged in seven rows and three columns. 18 chambers per plane have semi-circular notches to leave space for the bolts holding the iron structure of the magnet arms. Due to these notches, the rims of the chambers and the Lexan spacers inside the chambers, i.e. areas not sensitive to particle interactions, the geometrical acceptance of an RPC plane is limited to about 97 % [A[+]09b].

---

[11] The four RPC planes which were installed first, i.e. the two inner planes of both magnet arms in SM 1, have a thinner PET layer of only 190 µm. After the insufficiency of this insulation was noticed, all further RPC planes were equipped with a thicker PET layer. However, during the 2009 run, a section of one of these four RPC planes had to be disabled permanently due to discharges of the high voltage (see Section 4.3).

[12] Polypropylene

The signals on the RPC readout strips are picked up by the so-called interconnection boards. These completely passive printed circuit boards are attached to the PP layer of the RPC (see Figure 3.9). Each board has soldered connections to 16 readout strips and relays their signals to two different output connectors. In addition, the interconnection boards are used to connect the RPC's ground planes to the spectrometer's common ground [A+04b]. One of the two connectors is a socket used on dedicated planes to hold a so-called timing board for the PT trigger system (see Section 4.1.1). The other connector is for a twisted pair flat cable that directly transfers the signals to the readout electronics for the tracking. LVDS[13] line receivers are used as low cost discriminators for the almost 27 000 readout channels [B+12a].

When a charged particle travels through the RPC's gas volume, it ionizes the atoms and molecules along its path. The electrons freed in the ionization process are accelerated in the applied electric field towards the anode. Simultaneously, the ions are accelerated towards the cathode, but as their drift velocity is only of the order of 10^{-3} compared to the electrons, they do not make a significant contribution to the signal. Provided a sufficiently high gas gain is given, the electrons cause further ionizations in the gas, resulting in an electron avalanche. Its arrival at the anode leads to a rapid change in the anode current which induces a signal in the nearest readout strips. The RPCs are operated in the so-called streamer mode, were the electric field is high enough to cause a limited discharge between the Bakelite electrodes through the formation of a plasma channel. The high volume resistivity impedes significant currents in the electrodes. Therefore, the accumulated charges cause a local reduction in the electric field and, eventually, the streamer breaks down. The downside of this mode of operation is a longer dead time as compared to the so-called avalanche mode, in which the evolution of streamers is suppressed through the use of a lower voltage and the choice of the gas mixture. For OPERA, being a low-rate experiment with event rates in the RPCs of about $30\,\mathrm{Hz/m^2}$ [B+12b], the increased dead time is irrelevant. A substantial advantage of the streamer mode operation is the height of the signals induced by the streamers of about $100\,\mathrm{mV}$, rendering a costly electronic amplification of the primary detector signals unnecessary.

In addition to the 22 RPC planes embedded in each magnet, there are two further detector planes, one positioned directly in front of the first PT plane and one behind the second PT plane. These planes are called

---

[13]Low-voltage differential signaling, a standard for the transmission of differential signals, using a common-mode voltage of about $1.2\,\mathrm{V}$ and a differential voltage of about $350\,\mathrm{mV}$

XPCs[14] due to their cross-like tilted readout strips which are inclined by
$\pm 42.6°$ with respect to the horizontal. The corresponding coordinates are
named u and v. Instead of Bakelite, glass is used for the XPCs' electrodes.
While the second XPC has the same dimensions as the RPCs, the first
one is reduced in width to 7.5 m to match the target's dimensions, leaving
enough space to allow the BMS to operate on all target walls. Apart from
these differences, XPCs and RPCs are technically identical. Together with
dedicated RPC planes, the XPCs contribute to the generation of the PT trigger
signal. Furthermore, their task is to improve the track merging between the
different electronic detectors and to reduce possible ambiguities in the xy-plane.

Precision Tracker

The PT's main task is the determination of charge and momentum of muons
crossing the spectrometers with a momentum resolution $\Delta p/p$ of less than 25 %
for muon momenta up to 25 GeV [Z$^+$05]. To achieve this task, the muon tracks
are reconstructed before and after their deflection in the magnetic field using
drift tubes. As in all gaseous wire chambers, particles traversing a drift tube's
gas volume lose energy through ionization processes. Ions and free electrons are
accelerated along the field lines of the applied electric field. Towards the anode
wire, the electric field E increases:

$$E(r) = \frac{1}{r}\frac{V}{\ln(r_c/r_a)},\qquad(3.1)$$

r being the distance from the wire, r_c the cathode radius, r_a the anode radius
and V the electric potential. Providing the gas mixture, its pressure and the
applied voltage are chosen adequately, the electrons drifting towards the wire
cause an avalanche multiplication of the free charges, mainly in the immediate
vicinity of the anode wire [Sau77]. The resulting signal on the wire is than
large enough to be measured. If the time of the particle interaction in the
drift tube is known from an external source, e.g. the trigger signal from the
XPCs/RPCs, the arrival time of the signal at the anode wire is a measure for
the minimal drift distance inside the tube. This way, the measurement of a
time interval can be used to determine the shortest distance between particle
track and wire. The distance information from a single tube is insufficient to
reconstruct a track, since it may be any tangent to the corresponding drift
circle. To reconstruct a track without ambiguities, drift circles from at least
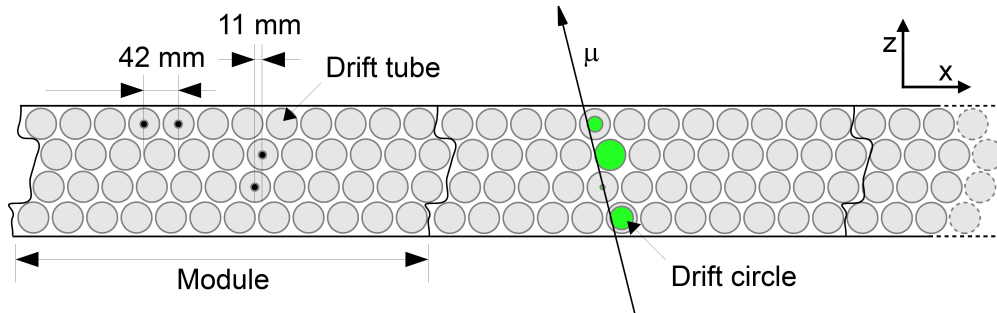three tubes are necessary (see Figure 3.10).

---

[14]Crossed RPC

Figure 3.10: Schematic cross section of the PT modules. To indicate the principle of the track reconstruction in the drift tubes, a muon track crossing four tubes and the corresponding drift circles are shown (figure adapted from [Göl12]).

The PT consists of 9504 vertically oriented aluminum drift tubes with a length of about 8 m, an outer diameter of 38 mm and a wall thickness of 0.85 mm. Gold-plated tungsten sense wires with a diameter of 45 μm are strung along the center of each tube, fixed only at the ends without additional centering supports in between. 48 tubes arranged in four staggered layers make up a module (see Figure 3.10). Nine of the twelve PT walls consist of 17 modules. The remaining three walls are in close vicinity to one of the targets. To leave enough space for the BMS, these PT walls have only 15 modules. There are six PT walls per SM, two in front of the magnet, two behind the magnet and two in between the magnet arms (see Figure 3.11). Due to space limitations inside the magnet, the tubes of the latter two PT walls are 15 cm shorter.

The drift tubes are filled with a gas mixture composed of Ar and CO_2 in the volume ratios 80/20 at an absolute pressure of 1005 ± 5 mbar. As the absolute pressure inside the LNGS experimental halls is kept at about 900–920 mbar, the PT is operated at a slight relative overpressure to avoid a contamination of the drift gas with oxygen [Fer06]. A high voltage of 2450 V is applied between the aluminum tubes, acting as cathode, and the sense wires, acting as anode. The drift tube signals are picked up at the upper end of the wire and transmitted to an amplifier/discriminator board, four of which are mounted directly on top of each PT module. For the signal amplification, chip sets from the forward muon detector of the L3 experiment at CERN are used [A+96]. The amplified signals are digitized using MAX963[15] ultra-high-speed comparators as discriminators. The amplifier/discriminator board is connected to two different boards via 7.5–16.0 m long twisted-pair

---

[15] Vendor: Maxim Integrated Products, USA

cables: a TDC[16] board and a so-called OPERA Support Board (OSUB). The
TDC board is used for the measurement of the drift times. It contains twelve
TDC chips with eight measuring channels each. The TDCs' measuring range
is $3.2\,\mu s$ and their resolution is $1.5\,ns$ [MSC04]. With a frequency of more
than $1\,Hz$ all TDC channels are constantly being temperature calibrated. The
OSUBs' main purpose is the setting of the discriminator thresholds. During the
physics runs all thresholds were set to $100\,mV$. Additionally, the OSUBs can
be used to send test pulses to the amplifier/discriminator boards to verify the
general functionality of the channels and to determine the signal propagation
delays of the twisted pair cables. Also the readout of 116 temperature sensors
distributed over the PT walls is done through the OSUBs.

The principle of the charge and momentum measurement with the PT is
illustrated in Figure 3.11. A muon crossing the spectrometer is deflected twice
and follows an S-shaped track. The PT is used to precisely reconstruct the
three straight track segments outside the magnetic field. For each segment, two
PT walls are available. The particle's momentum p can then be calculated from
the deflection angle $\Phi_2 - \Phi_1$:

$$\Phi_2 - \Phi_1 = \frac{qBd}{p}. \tag{3.2}$$

q is the particle's charge, B the magnetic field and d the distance traveled in
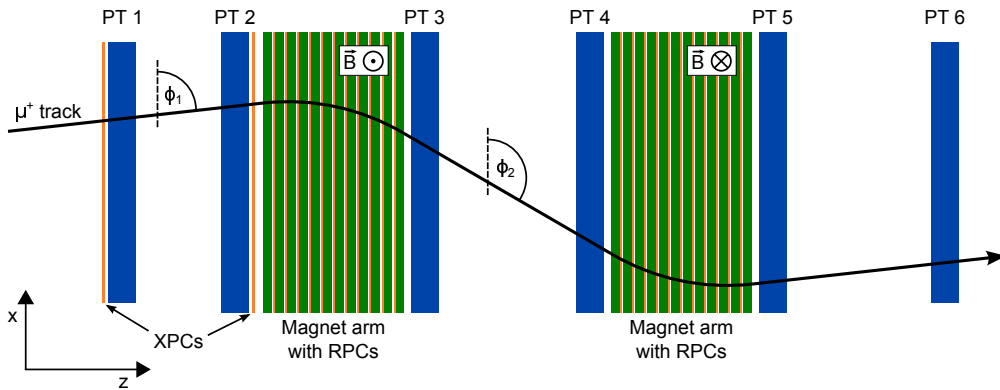the magnetic field.

Figure 3.11: Schematic top view of one spectrometer, illustrating the principle of the
determination of a particle's sign of charge and measurement of its momentum. The
six PT walls are labeled PT 1 through PT 6. The size of the deflection angle $\Phi_2 - \Phi_1$
is highly exaggerated in this example.

---

[16]Time-to-digital converter

During all five years of the physics runs, from 2008 to 2012, the performance of the PT exceeded the expectations. A loss of up to 1% of the drift tubes, i.e. 95 tubes, over the detector's run time was anticipated and considered acceptable in terms of efficiency, assuming a random distribution of the dead tubes. At the beginning of the 2008 run, 41 drift tubes did not deliver any signals.[17] Before the start of the 2010 run, the number of dead tubes was reduced to 18 owing to the replacement of five defective amplifier/discriminator boards. Until the end of the final beam run in 2012, the number of dead tubes never exceeded 20. Moreover, of the 48 high voltage channels only one repeatedly ramped down due to an excessive leakage current, in total 38 times during the physics runs. This problem was addressed by the implementation of a software script, automatically ramping the channel up within ten minutes after an incident. This way, the corresponding channel downtime was reduced to a few hours compared to a detector uptime of more than 800 days. And finally the PT gas system exhibited a very stable performance during the entire time. The excellent gas tightness of the whole system ensured continuous detector operation even during maintenance interventions.

3.2.4 Veto System

An additional double layer of glass RPCs is installed in front of SM 1 to tag charged particles entering the detector in beam direction. The veto planes are $1004\,\mathrm{cm}$ wide and $923\,\mathrm{cm}$ high [B$^+$09b]. Each of the two planes is equipped with horizontal and vertical copper readout strips with a pitch of $2.5\,\mathrm{cm}$.

Due to the reduction of the target mass (see Section 3.2.1), the first two brick walls are left empty. Therefore, in addition to the dedicated veto system, the first three TT planes in SM 1 serve as a veto detector as well.

3.2.5 Data Acquisition System

The OPERA data acquisition (DAQ) system is structured in a highly modular way. Its key element, the so-called Ethernet Controller Mezzanine (ECM), is distributed over all sub-detectors [Mar10]. The ECMs are small printed circuit boards plugged onto the specific controller boards of each electronic detector, in the case of the PT it is mounted on the TDC board. The task of the more than 1000 ECMs is to collect the data from the front-end electronics of the sub-detectors and to transfer it to the DAQ servers via an Ethernet network.

---

[17]A drift tube is considered dead if it produces no entries during a time interval of 25 days of detector operation.

As OPERA is an experiment with a low event rate, a 100 MBit network connection is sufficient to perform this task. The asynchronous readout of the data necessitates the assignment of a timestamp at the level of the ECM. For this purpose, the ECM contains a 100 MHz oscillator [D$^+$04]. Through a dedicated clock distribution network all local oscillators are synchronized with a GPS[18] time signal. The calibration of the clock distribution system, including the signal delay from the GPS antenna outside the tunnel to the detector, allows to correlate the recorded events with the UTC[19] time. Likewise, the proton extractions from the SPS at CERN (see Section 3.1) are UTC timestamped. This way, events in the OPERA detector can be correlated with the CNGS beam, providing all signal propagation delays and the neutrinos' time of flight between CERN and the LNGS are taken into account. A time interval of 40 µs, centered at the beginning of each proton extraction, which have a duration of 10.5 µs, is used to define the so-called ontime events.

3.3   Data Taking Procedure and Analysis Chain

The analysis of neutrino interactions in OPERA starts with the reconstruction of ontime events using the electronic detector data. If a neutrino vertex inside one of the two target areas is predicted, the brick with the highest probability of containing the vertex is extracted by the BMS. A collimated X-ray beam is used to apply several marks on the downstream side of the brick. These marks can later be seen on the CS and on the most downstream film of the brick. Their purpose is the alignment of the two CS films with respect to each other and with respect to the brick. While the CS package is detached from the brick and the films are developed in an underground facility, the corresponding brick is stored in an underground storage area equipped with an iron shielding against the ^{40}K radiation from the concrete. After development, the CS films are scanned. If no compatible tracks are found, a new CS package is attached to the brick which is then reinserted into the detector and the vertex search continues with the second most likely brick. Up to four bricks are extracted and analyzed in this way. If at least one track in accordance with the electronic detector prediction is found in the CS, the brick is analyzed. Bricks removed for analysis are not replaced in the detector. Therefore, the target mass decreased continuously during the five years of data taking. Until the end of the final run in 2012, about 10 000 bricks, corresponding to about 7 % of the initial target mass, were permanently removed from the detector.

---

[18]Global Positioning System

[19]Coordinated Universal Time

The brick is again exposed to an X-ray beam, this time to apply lateral marks on all emulsion films to facilitate a quick identification of each film in terms of position and orientation inside the brick. Subsequently, the brick leaves the underground laboratory to be exposed to cosmic rays for a duration of twelve hours. As a result, about one penetrating track per mm^2 is recorded by the emulsions. These tracks are later used for inter-emulsion alignment and to identify distortions inside the emulsion layers caused by the film development process. As the CS films are detached from the brick before the cosmic ray exposure, they also serve as a veto for the cosmic ray tracks in the brick emulsions. The bricks are then brought to a darkroom and are dismantled. Each emulsion film is labeled with a unique binary code. The films are developed using a fully automated chemical development plant capable of processing up to 3000 films per day (see Figure 3.12). The general process is similar to the one for photographic film, the main steps being:

- development (reduction of Ag^+, enlarging the latent image clusters)

- stop bath (interruption of the development process)

- fixation (dissolving of the remaining silver halide)

- washing (removal of the fixer and silver halide remnants)

After drying, the emulsions are packed and shipped to the various scanning laboratories in Europe and Japan.

Figure 3.12: One of the six automated chains of the film development facility at the external LNGS laboratory

The emulsions are scanned by automated scanning microscopes equipped with digital cameras (see Figure 3.13). There are different systems in use which are continuously improved in terms of scanning speed. The minimum speed, already achieved at the beginning of the data taking, is $20\,cm^2$ per hour

and emulsion layer [A$^+$06b]. Considering the number of about 30 microscopes in operation, this scanning speed is more than sufficient to manage the average rate of about 25 events per day and a scanning area of about $200\,\mathrm{cm}^2$ per event. Nevertheless, a novel scanning system is developed in Japan which already exceeds a scanning speed of $1000\,\mathrm{cm}^2$ per hour and layer.
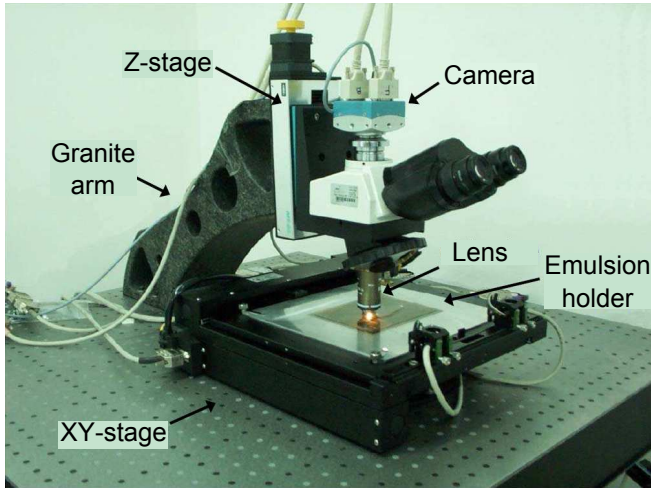

Figure 3.13: One of the microscope stations of the European Scanning System. The XY-stage moves the emulsion holder in the horizontal and the Z-stage moves the lens and the camera perpendicular to the emulsion (figure adapted from [A$^+$06b]).

The microscopes automatically adjust their focal plane, scanning each $44\,\mathrm{\mu m}$ thick emulsion layer in 15 equidistant levels of depth parallel to the surface (see Figure 3.14a). The search for clusters in each field of view and the linear fitting of 3D tracks inside an emulsion layer, called microtracks, is done in real-time. The next step is to link microtracks from both emulsion layers of the same film across the plastic base. These tracks are called basetracks (see Figure 3.14b). Finally, the fit of several basetracks across the intermediate lead plates reveals the particle track through the brick (see Figure 3.14c). Tracks are traced backwards until a vertex is found. From there, all tracks belonging to the vertex are followed in forward direction until the entire event is reconstructed.

3.4 τ Detection and Background Sources

The signal of the ν_μ to ν_τ oscillation searched for in OPERA is the CC interaction of the ν_τ in the detector's lead/emulsion target:

$$\nu_\tau + N \to \tau^- + X, \tag{3.3}$$

where N is a target nucleon and X are all further products. The interaction is identified by the detection of the τ lepton by means of its characteristic decay topologies. There are two different ways in which a decay may be detected in
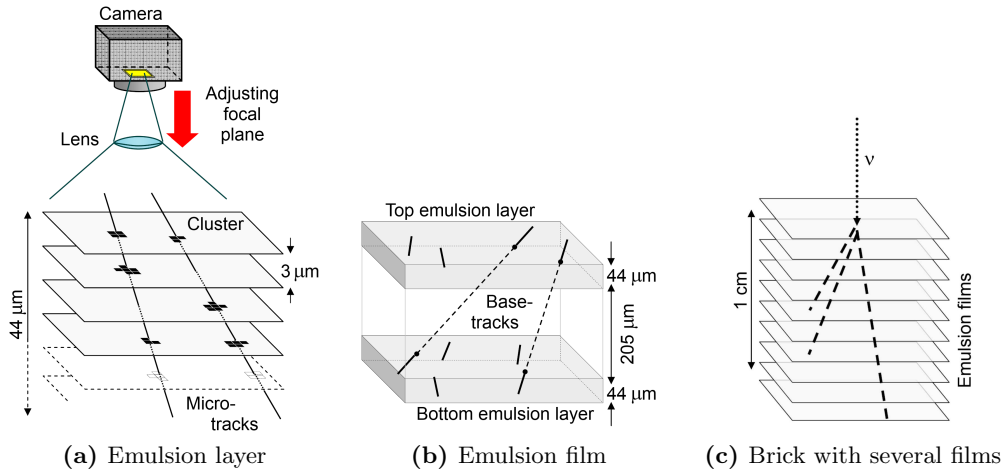
Figure 3.14: Each emulsion layer is scanned in 15 levels of depth (figure adapted from [Sir07]). A linear fit to several clusters is called a microtrack (a). The linking of two microtracks across the film's plastic base is called a basetrack (b). The fit of several basetracks reveals the particle's track through the brick (c).

an ECC brick. In the case of a so-called long decay, the τ lepton crosses at least one emulsion layer before it decays. Figure 3.6b shows an example of a τ^- that is produced in one lead plate and decays in the following one. Here, the kink angle at the τ decay vertex can directly be measured. If the τ decays in the same lead plate in which it was produced, it is called a short decay. In this case the impact parameter (IP), which is the shortest distance between the primary vertex and the extrapolated track of the charged daughter particle, is used to identify the τ lepton (see Figure 3.15).
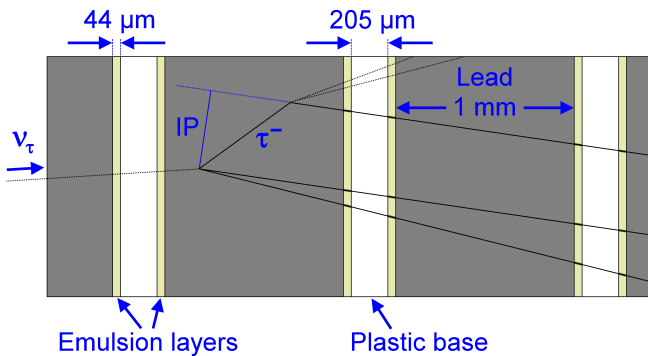

Figure 3.15: Schematic side view of an ECC brick showing a short τ decay, where a τ^- decays in the same lead plate in which it was produced

The dominant τ decay channels are listed in Table 3.3. The hadrons (mostly pions) and the electrons produce showers in the target. The charged pions primarily lose their energy by ionization, while for the electrons the emission of bremsstrahlung is the main source of energy loss. Due to the different nature of these processes, the corresponding shower profiles are different and can be

Table 3.3: Branching ratios of the dominant τ decay channels [O$^+$14]. h stands for a hadron (in most cases a pion) and n is the number of π^0 in the final state.

Decay Channel	Reaction	Branching Ratio
Hadronic, 1-prong	$\tau^- \to h^- + \nu_\tau \, (+ \, n\pi^0)$	48.1 %
Hadronic, 3-prong	$\tau^- \to h^- + h^- + h^+ + \nu_\tau \, (+ \, n\pi^0)$	14.9 %
Electronic	$\tau^- \to e^- + \nu_\tau + \overline{\nu}_e$	17.8 %
Muonic	$\tau^- \to \mu^- + \nu_\tau + \overline{\nu}_\mu$	17.4 %

used to distinguish hadronic and electronic τ decays [A$^+$07b]. Muons deposit much less energy along their flight path and travel long distances through the detector. They are identified by the electronic detectors and their charge and momentum is determined by the spectrometers.

There are three major sources of background for the oscillation search, which may mimic the τ decay topology. First of all, charmed hadrons may be produced in ν_μ interactions in the target, most frequently in the process:

$$\nu_\mu + N \to \mu^- + c, \tag{3.4}$$

N being a target nucleon and c a charm quark. The decay topology of the charmed hadrons (D^0, D^+, D_s^+ or Λ_c^+) is similar to the one of the τ lepton due to their comparable lifetimes. If the μ^- at the primary vertex remains undetected, the interaction 3.4 may be mistaken for a ν_τ event. However, in the muonic decay channel the charmed hadron can be identified by the detection of the μ^+ originating from the secondary vertex using the spectrometers' charge determination capability. Another background source comes from hadronic re-interactions. A 1-prong inelastic interaction of a primary hadron produced in a ν_μ NC event or in a ν_μ CC event where the primary muon escapes detection may also be mistaken for a τ signal. And finally, muons from ν_μ CC interactions undergoing large angle Coulomb scattering may contribute to the background. If the scattering occurs within a few millimeters from the primary vertex, the event mimics the muonic τ decay. The expected number of signal and background events per decay channel for the data subsample analyzed in [A$^+$14g] is given in Table 3.4.

3.5   Analysis Results

A first ν_τ candidate event was found in the analyzed subsample of the 2008/2009 data [A$^+$10b]. It occurred on 22 August 2009 in the target of SM 1.

Table 3.4: Expected number of signal and background events in OPERA based on the data subsample analyzed in [A$^+$14g]. The data set includes all 0μ events and the 1μ events with a muon momentum of less than $15\,\mathrm{GeV}$. For the 2008 and 2009 runs the two most probable bricks have been analyzed, while for the runs 2010–2012 only the most probable bricks have yet been considered. The event numbers are calculated using $\Delta m_{23}^2 = 2.32 \times 10^{-3}\,\mathrm{eV}^2$ and $\sin^2 2\theta_{23} = 1$ (source: [A$^+$14g]).

Decay Channel	Expected Signal	Expected Background		
		Charm Decays	Hadronic Re-interactions	Large Angle μ Scattering
$\tau \to 1h$	0.41 ± 0.08	0.015 ± 0.003	0.018 ± 0.005	—
$\tau \to 3h$	0.57 ± 0.11	0.152 ± 0.030	0.002 ± 0.001	—
$\tau \to e$	0.62 ± 0.12	0.027 ± 0.005	—	0.014 ± 0.007
$\tau \to \mu$	0.52 ± 0.10	0.003 ± 0.001	—	—
Total	2.11 ± 0.42	0.198 ± 0.040	0.021 ± 0.006	0.014 ± 0.007

Figure 3.16 shows the scanning results in an event display of the corresponding ECC brick. Tracks number 1–7 point to the primary vertex, track 8 is the decay daughter, and the electromagnetic showers $\gamma 1$ and $\gamma 2$ most likely point to the secondary vertex. Track 4 exhibits a kink topology with a kink angle of $(41 \pm 2)\,\mathrm{mrad}$ after a path length of $(1335 \pm 35)\,\mathrm{\mu m}$, qualifying as τ candidate. Tracks 1, 3, 5, 6 and 8 are associated with hadrons. The highly ionizing particle (track 2) is identified as a proton, and track 7 originates most likely from a neutral particle. The event satisfies all kinematical selection criteria for the $\tau \to 1h$ channel.

The second candidate was recorded on 23 April 2011, also in SM 1 [A$^+$13c]. Here, the τ decay shows a 3-prong topology (see Figure 3.17). Tracks 1 and 2 are connected to the primary vertex, while tracks 3–5 originate from the secondary vertex. Track 2 is the τ candidate with a track length of $(1466 \pm 10)\,\mathrm{\mu m}$. All other tracks are associated with hadrons. The secondary vertex is located inside the plastic base of an emulsion film, which is ideal to strongly constrain hadronic re-interactions as a source of the event. All kinematical selection criteria for the $\tau \to 3h$ channel are being satisfied.

The third candidate event occurred on 2 May 2012, leaving tracks in the target and the spectrometer of SM 1 [A$^+$14e]. The event display on the level of the extracted vertex brick is shown in Figure 3.18. Tracks 1 and 2 originate from the primary vertex, track 3 and the γ shower point to the secondary vertex. The particle associated with track 1 is identified as a hadron. Track 2
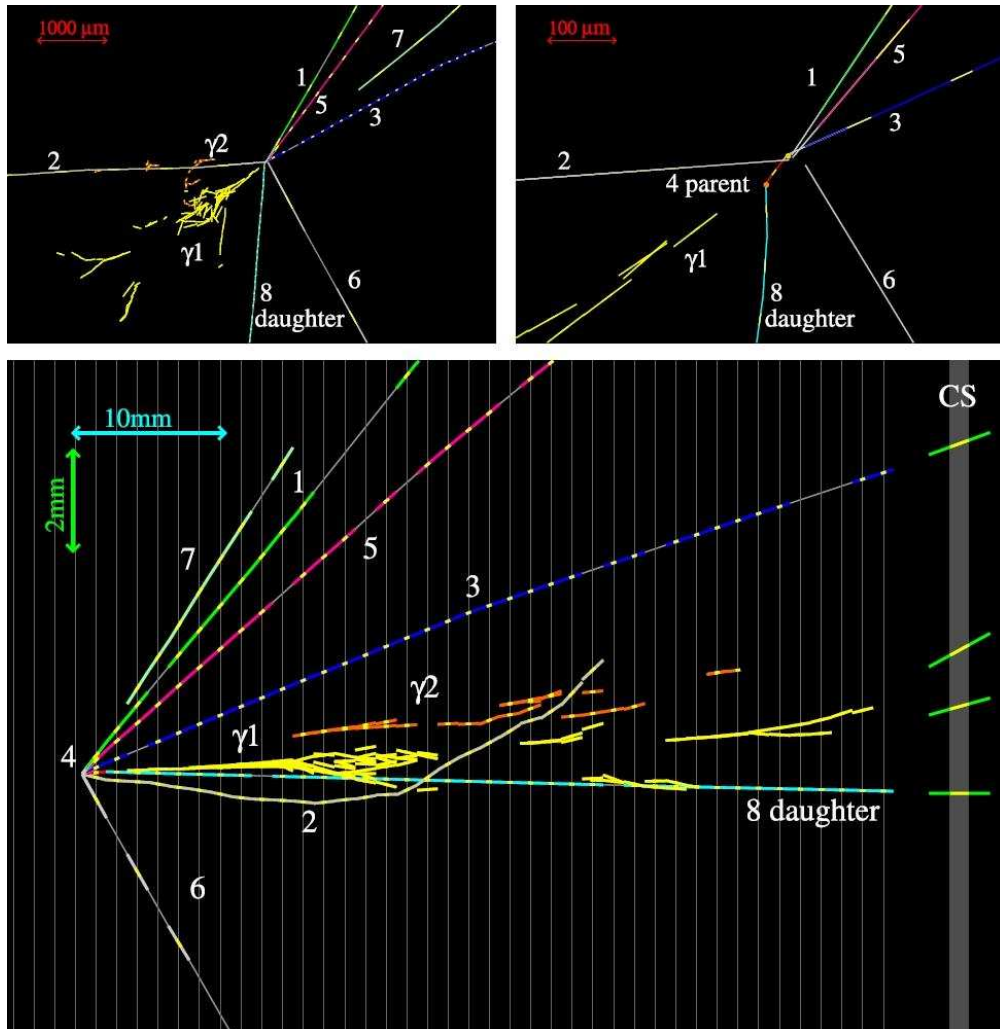
Figure 3.16: Event display for the first ν_τ candidate (figure taken from [A⁺10b]). The upper figures show the event in beam direction, the upper right one is a zoomed in version of the left one. The lower figure shows a view of the event perpendicular to the beam direction. The τ lepton (track 4) decays into one hadron (track 8).

is the τ candidate, decaying after a path length of $(376 \pm 10)\,\mu$m in a 1-prong decay with a kink angle of $(245 \pm 5)\,$mrad. The decay daughter (track 3) is identified by the electronic detectors as a muon. It stops in the first magnet arm after crossing six RPC planes. As the particle does not traverse one complete magnet arm, its charge and momentum cannot be determined by the PT. Instead the momentum is estimated from the track length. The charge is determined using a parabolic fit to the RPC data, indicating a μ^- with a significance of $5.6\,\sigma$. The event passes all kinematical selection cuts for a $\tau \to \mu$ decay.
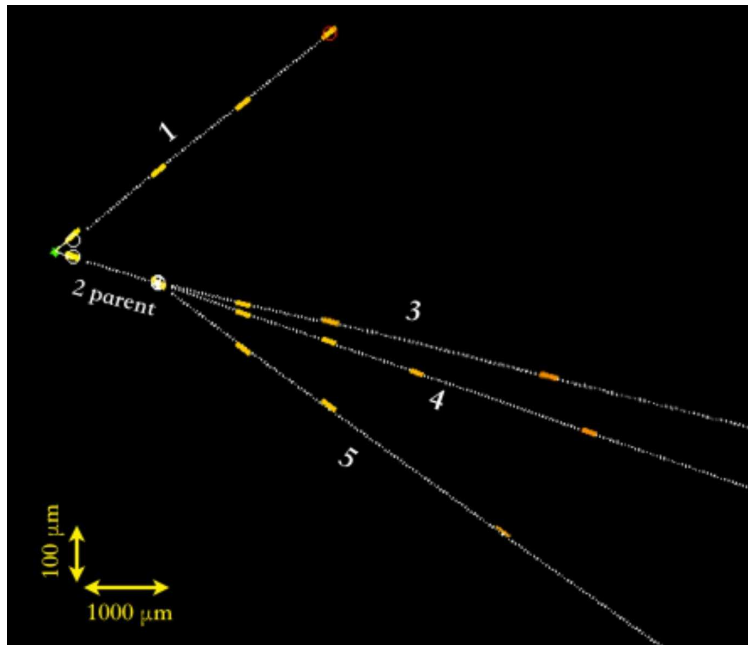
Figure 3.17: Event display for the second ν_τ candidate (figure taken from [DiC13]). The τ lepton (track 2) decays into three hadrons (tracks 3–5).
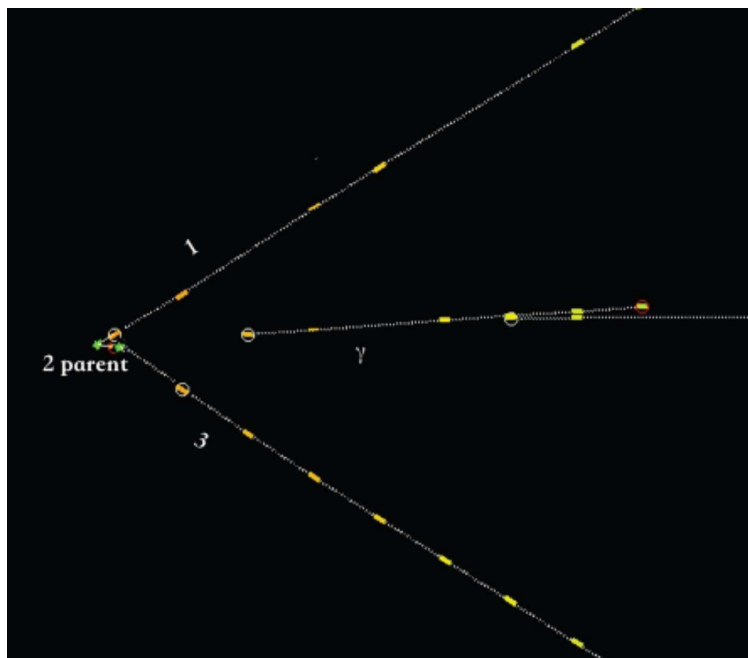

Figure 3.18: Event display for the third ν_τ candidate (figure taken from [DiC13]). The τ lepton (track 2) decays into a μ^- (track 3).

On 9 September 2012 a fourth ν_τ candidate event was recorded in SM 2 [A$^+$14g]. Figure 3.19 shows an event display of the electronic detectors and Figure 3.20 shows the scanning results of the vertex ECC brick. Track 1 is the τ candidate decaying after a flight length of $(1090 \pm 30)\,\mu$m. The only visible daughter track has a kink angle of $(137 \pm 4)\,$mrad with respect to the parent track. Tracks 2–4 and the two showers $\gamma 1$ and $\gamma 2$ point to the primary vertex. The momenta of all tracks reconstructed in the bricks are determined by Multiple Coulomb Scattering [A$^+$12c]. This way, track 2 can be associated with a hadron by ruling out the muon hypothesis due to its range/momentum ratio. Tracks 3, 4 and the daughter track are also identified as hadrons. The event satisfies all kinematical selection criteria for the $\tau \to 1h$ channel.

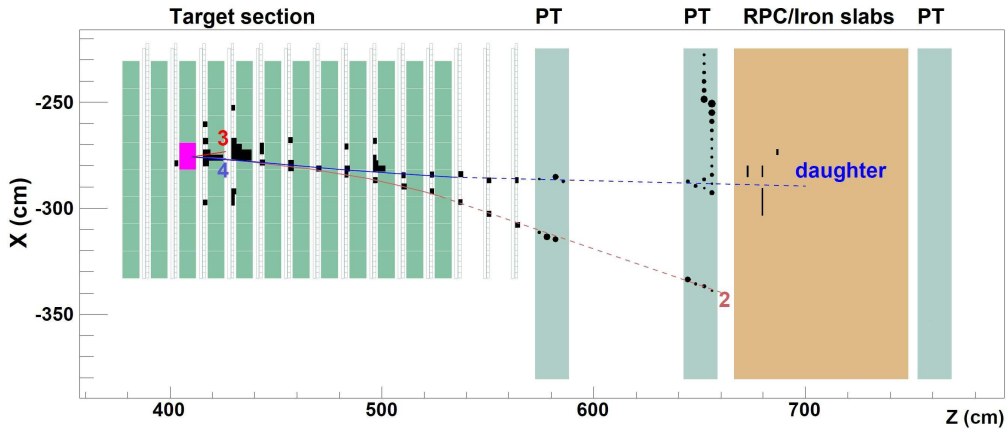**Figure 3.19:** Event display of the electronic detectors for the fourth ν_τ candidate (figure adapted from [A$^+$14g]). It shows a part of SM 2 in the xz-projection (top view). The vertex brick is highlighted. The unlabeled track in the second PT plane going in positive x-direction is consistent with a backscattered proton or pion from an interaction of the daughter particle.

Given the analyzed data sample and the number of expected background events (see Table 3.4), the observation of four ν_τ candidates establishes the $\nu_\mu \to \nu_\tau$ oscillation scenario with a significance of $4.2\,\sigma$ [A$^+$14g]. However, the search for further candidate events continues as the dataset is extended to the second most probable brick of the runs 2010–2012.

Despite OPERA being a highly specialized experiment dedicated to the detection of ν_τ interactions, also other analyses are conducted. For instance, the tracking capabilities of the emulsions are exploited to identify electrons produced in ν_e CC interactions. This way, $\nu_\mu \to \nu_e$ oscillations can be studied in appearance mode. In a first analysis using the 2008 and 2009
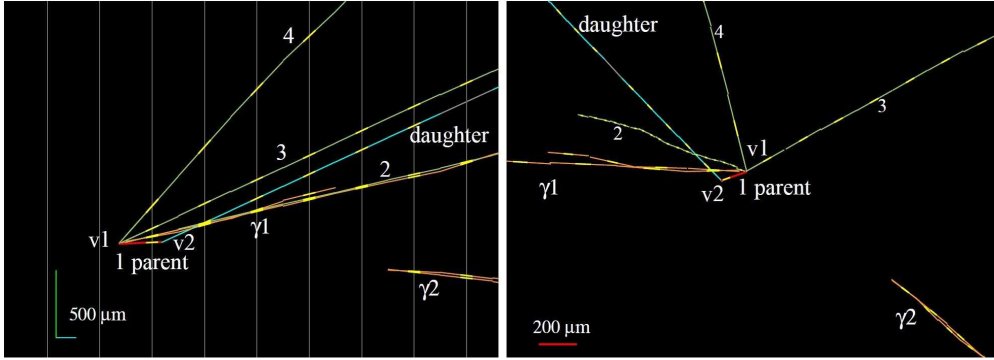
Figure 3.20: Event display of the vertex ECC brick for the fourth ν_τ candidate (figure taken from [A$^+$14g]). The left figure shows the event perpendicular to the beam direction, the right one is a view in beam direction. The τ lepton (track 1) decays into one hadron. The primary and the secondary vertices are labeled v1 and v2 respectively.

data, 19 ν_e candidate events were found. This number is compatible with the non-oscillation expectation of 19.8 ± 2.8 events in the three-flavor mixing model [A$^+$13d]. In addition, OPERA is able to set limits on the parameter space available for a non-standard ν_e appearance suggested by the results of the LSND and MiniBooNE experiments (see Figure 3.21).

Another analysis utilizes the spectrometers to determine the charge ratio of high energetic cosmic rays [A$^+$14f]. The muons' charge and momentum is measured by the PT. Muons reaching the OPERA detector in the underground laboratory with its shielding of 3800 meters water equivalent have a minimum surface energy of about $1.5\,\mathrm{TeV}$ [A$^+$10a]. The measurement of the muon charge ratio $R_\mu \equiv N_{\mu^+}/N_{\mu^-}$, i.e. the number of positively over negatively charged muons, was also done by other experiments. However, OPERA is able to contribute several data points at surface energies above $1\,\mathrm{TeV}$ (see Figure 3.22). Nevertheless, due to the increased number of charge-misidentifications and limited statistic at higher energies, the data cannot distinguish between different models for the prompt muon production in the atmosphere.
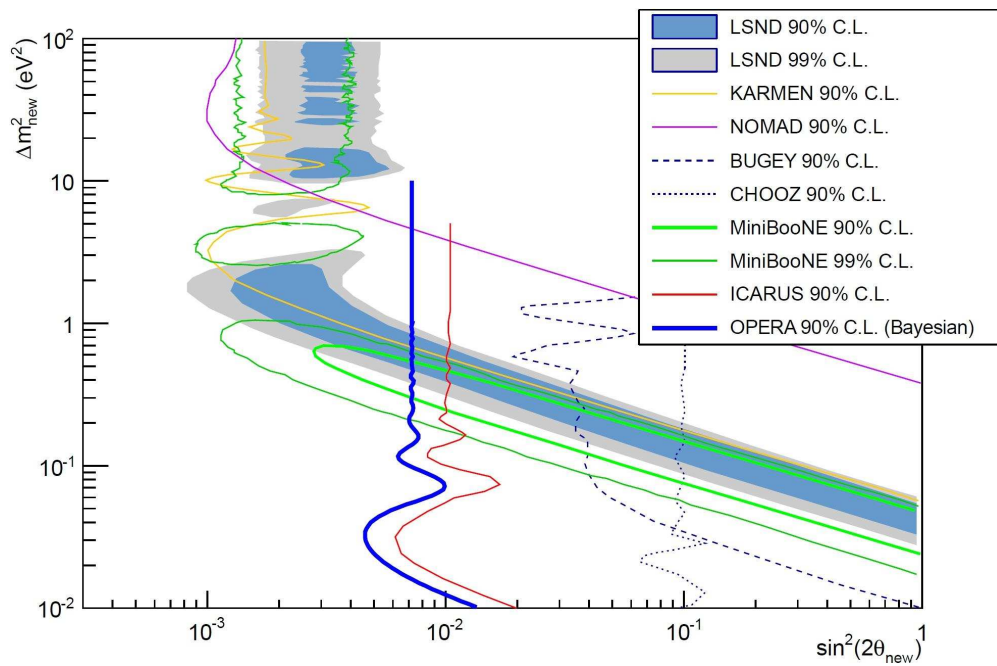
Figure 3.21: Exclusion plot for the parameters of the non-standard $\nu_\mu \rightarrow \nu_e$ oscillation. The entries for LSND and MiniBooNE correspond to the positive indications published by the two experiments. All other lines are exclusion limits (figure taken from [A+13d]).
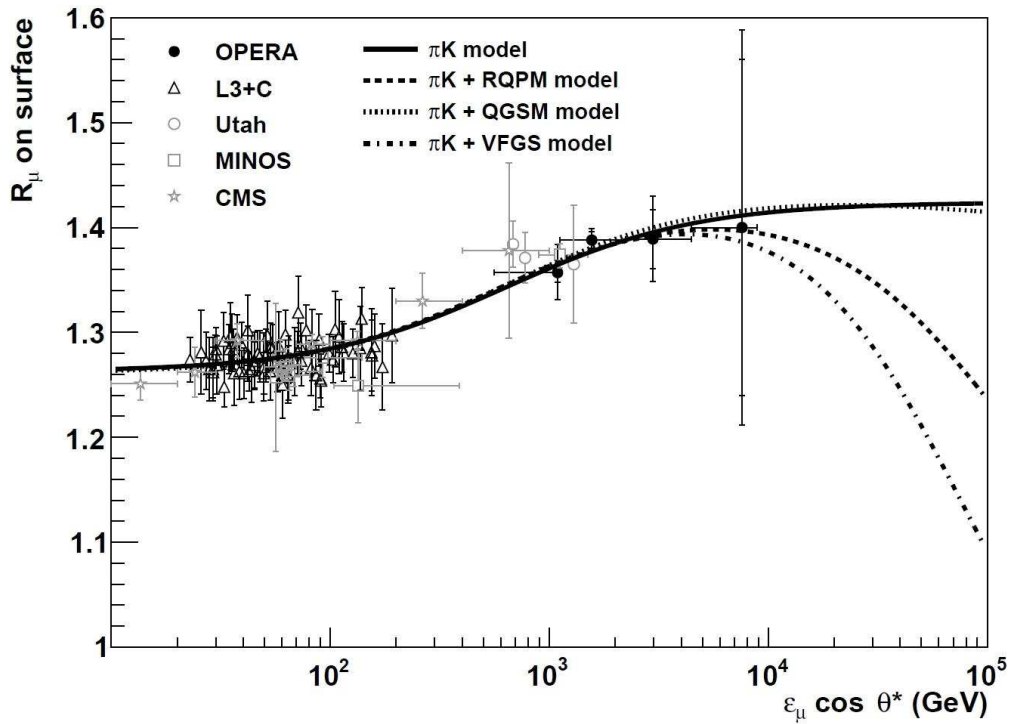
Figure 3.22: Muon charge ratio R_μ as a function of the vertical surface energy $\epsilon_\mu \cos\theta^*$, ϵ_μ being the muon energy at the earth's surface and θ^* being the zenith angle at the muon production point. The different lines are fits of the OPERA and the L3+C [A$^+$04a] data using different models for the prompt muon production in the atmosphere. The results of the other experiments are shown for comparison (figure taken from [A$^+$14f]).

Chapter 4

The Trigger System for the Drift Tube Detector

The readout of a drift tube for the purpose of obtaining track information on a charged particle requires two signals: one is the signal from the tube itself, induced by the particle crossing the drift gas, the other is an external reference signal that marks the time of the particle's passage through the detector and triggers the drift tube readout. The time interval between the reference signal and the drift tube signal depends on the distance which the electrons, that are set free in the drift gas by the ionizing particle, are drifting towards the anode wire. In this way, the spatial track information can be obtained from a time measurement.

The principle of the drift time measurement is illustrated in Figure 4.1. A charged particle travels through the detector and crosses the RPC planes dedicated to provide the trigger signal. After the time of flight t_{tof} it passes through a drift tube and ionizes the gas along its track. The free electrons closest to the anode wire require the time t_{drift} to drift to the wire and generate a signal. This signal propagates along the wire and reaches the readout end after the time t_{wire}. The drift tube signal is transferred to the input of a TDC board via a cable with the propagation delay t_{cable}[1] and starts a TDC measurement. Meanwhile, the signals from the dedicated RPC planes are processed by the trigger logic. A coincidence of at least two signals within a specified time interval is required to issue a trigger signal in order to minimize the trigger rate due to noise in the RPCs. The time interval $t_{trigger}$ after which the trigger signal is delivered to all connected TDCs as a common stop signal is deliberately prolonged by the stop delay. The length of

---

[1] The time interval t_{cable} includes the propagation time on the amplifier/discriminator board connected to the drift tubes. For the sake of simplification, these boards are omitted in Figure 4.1.
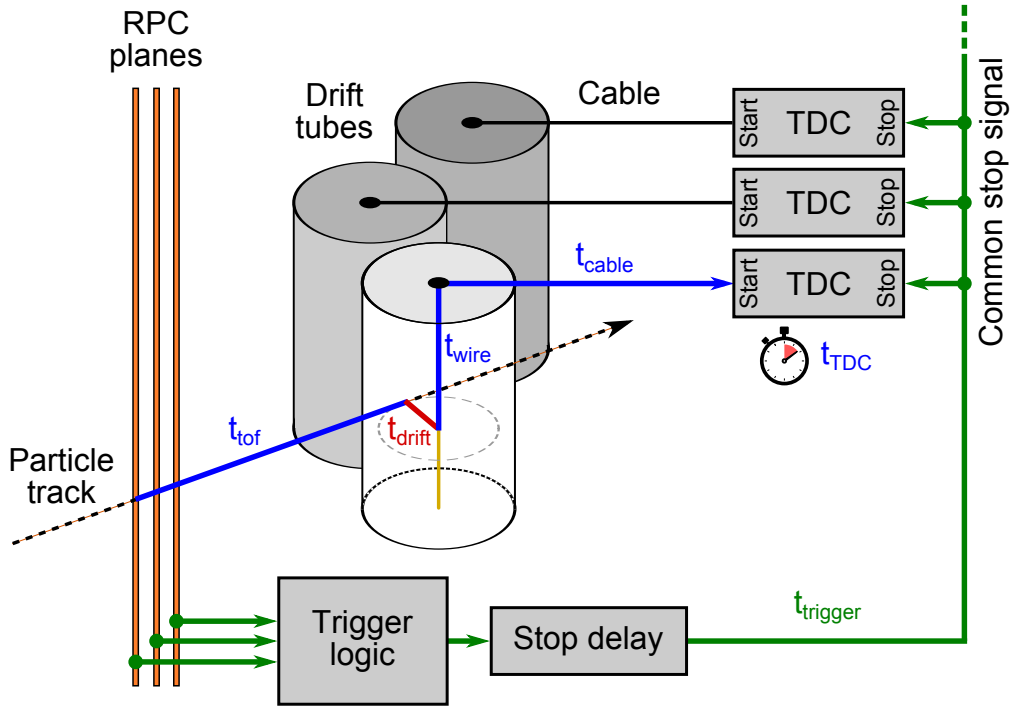
Figure 4.1: Simplified schematic of the drift time measurement. All time intervals used in this chapter and their definitions are listed in Appendix B, Table B.1.

the delay is chosen large enough, so that all drift tube signals are guaranteed to reach the TDC boards before the delayed trigger signal arrives and stops all TDC time measurements. Finally, t_{TDC} is the time interval measured by a TDC channel between the start and the stop signal. Appendix B contains a list with the definitions of all relevant time intervals used in this chapter.

Figure 4.2 shows the chronological order of the time intervals listed above in a schematic timeline. Here, the signals of two drift tubes are displayed. The essential parameter for the track reconstruction is the drift time t_{drift}. To obtain its value, all other time intervals have to be known. Depending on the particle's trajectory, the time intervals t_{tof} and t_{wire} have different values for each drift tube. They can be estimated using coarse 3D track information from the TT and the RPCs [Won07]. Also the delays t_{cable} of the drift tubes' readout cables are not necessarily the same for different tubes due to the use of various cable lengths. The individual values of t_{cable} have been determined in [Göl12] by means of test pulse measurements. As mentioned above, t_{TDC} is the value measured by the TDC. The determination of the many contributions resulting in the time interval $t_{trigger}$ is the main subject of this
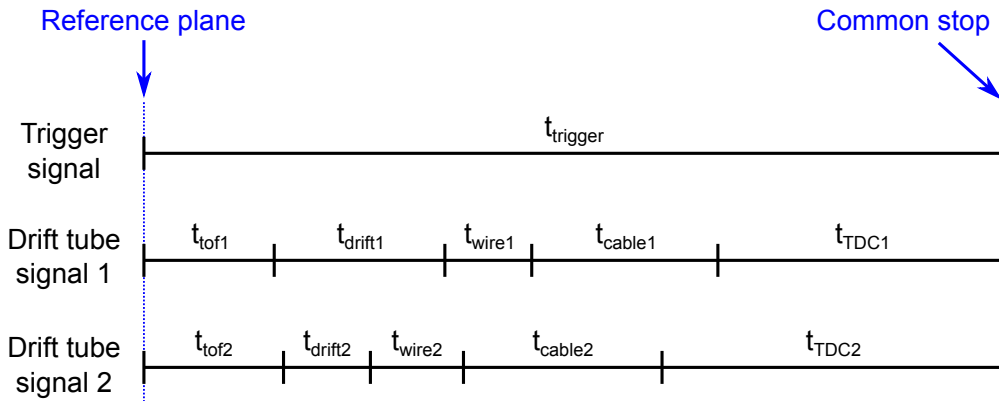
Figure 4.2: Schematic timeline illustrating the principle of the drift time measurement. Time is proceeding from left to right. The different time intervals are not to scale for better readability.

thesis. The subcomponents of this interval as well as all corresponding calibration methods used to determine their values are described in detail in Chapter 5.

In the following sections the technical specifications of the trigger system and the entire process of the trigger signal production are elaborated.

4.1 Concept and Layout of the Trigger System

The trigger system for the twelve drift tube walls of the OPERA detector is divided into two parts, one for each SM and serving six drift tube walls each. Since these two subsystems are equal in their general layout and functionality, all further descriptions will refer to only one SM, unless stated otherwise.

A so-called trigger station consists of three RPC/XPC planes, located in the proximity of a pair of drift tube walls (see Figure 4.3). There are three trigger stations per SM. The first one is made up of both XPC planes and the first RPC plane (RPC 1). The second trigger station is composed of the last RPC in the first magnet arm (RPC 11) and the first two RPCs in the second magnet arm (RPCs 12 and 13), while the third station consists of the last three RPCs in the magnet (RPCs 20 to 22). Since the noise rate of a single RPC plane is above $1\,\text{kHz}$ [A$^+$09b], while the highest event rate the DAQ system is able to process is of a few tens of Hertz, it is necessary to use a coincidence signal of more than one RPC plane to generate a trigger signal with a rate of a few Hertz. The distribution of the planes belonging to a trigger station is chosen in such a way that the trigger is optimized in terms of acceptance
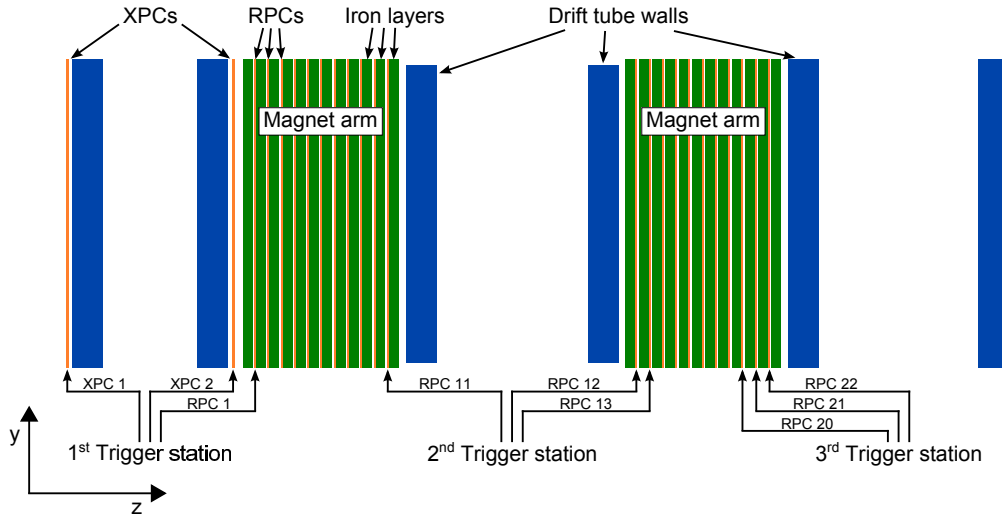
Figure 4.3: Schematic side view of one spectrometer with its six drift tube walls, arranged in pairs, and the corresponding three trigger stations, which are composed of three RPC/XPC planes each

for particles crossing the drift tube walls in beam direction (along the z-axis, see Figure 4.3). Nevertheless, in the given configuration the trigger system is also sensitive to the majority of atmospheric muons crossing two or more drift tube walls. In contrast to beam induced muons, the trajectories of which, on average, exhibit only minor deviations from the z-axis direction, atmospheric muons cross the detector with a wide-spread angular distribution, both in the xz- and in the yz-plane. This variety of tracks is of major importance to the alignment procedure for the drift tube detector because it increases the number of combinations for comparing the spatial orientation of single modules [Göl12]. In addition, it facilitates the analysis of a larger sample of atmospheric muons.

Particle tracks that are almost perpendicular to the z-axis, and which cross only one drift tube wall, are very unlikely to cross two RPC/XPC planes to produce a trigger signal. However, even if these tracks were recorded, the quality of the track reconstruction in the drift tubes would be insufficient. The drift tubes themselves offer no information on the y-coordinate of a particle transit. Therefore, the actual three-dimensional length of the track inside the drift tubes and the distance the signals have to propagate along the anode wires towards the readout electronics, are unknown. To compensate different times of flight and signal propagation times for the track reconstruction, external information on the y-coordinate is necessary. An estimate of the three-dimensional track can be obtained either by an interpolation

of hits in other electronic detectors (RPCs/XPCs, TT) on both sides of a pair of drift tube walls or by an extrapolation of a sufficiently long track on one side of the drift tubes [Won07]. Tracks crossing only one drift tube wall rarely fulfill this requirement and therefore do not need to trigger a readout.

When a charged particle crosses an RPC chamber, a signal is induced in the readout strips closest to the interaction point and propagates to the ends of the strips. To gather the tracking information inside the magnet arms, all RPC and XPC channels are read out by transferring the signals directly from the ends of the strips to the readout electronics on top of the detector via twisted pair cables. This is possible because the RPCs are operated in streamer mode, generating signals with an amplitude of several tens of mV, which do not need further amplification to be transmitted over up to 20 m of unshielded twisted pair cable. The chosen operation mode and readout design have the advantage of saving costly front-end electronics, but the use of single-ended signaling over such long cables spoils the events' timing information. The intrinsic time resolution of the RPC signal is of the order of a few nanoseconds [B$^+$12c]. However, such a precise timing is not essential for the tracking inside the magnets, given the low interaction rate in OPERA, yielding a very low probability of a coincidence of two particle interactions inside the 500 ns time frame, attributed to an event. In contrast, for the trigger signal of the drift tube detector the time resolution is of great importance, since it directly limits the spatial resolution that can be achieved for the tracking inside the drift tubes. For this reason the XPCs and the dedicated RPC planes listed above are instrumented with so-called timing boards (see also Section 4.1.1). These compact electronic boards are directly mounted to the sides of the RPC/XPC planes (see Figure 4.4), parallel to the tracking readout cables, and convert the incoming detector signals into LVDS signals before they are sent over additional twisted pair cables. This way, the detector's intrinsic time resolution is preserved for the trigger system. There are 14 timing boards attached to an RPC plane. For details on the timing boards, their exact distribution on the RPC planes and on the readout of the XPC signals used for the trigger system, see Section 4.1.1.

The twisted pair cables labeled A′ in Figure 4.4 are 16–18 m long and connect the timing boards with the so-called OPE^2 boards. There is one twisted pair cable per two timing boards, that is seven cables per RPC plane. The OPE boards are located on top of the OPERA detector. They provide the logic OR of all signals coming from one plane (see also Section 4.1.1). The
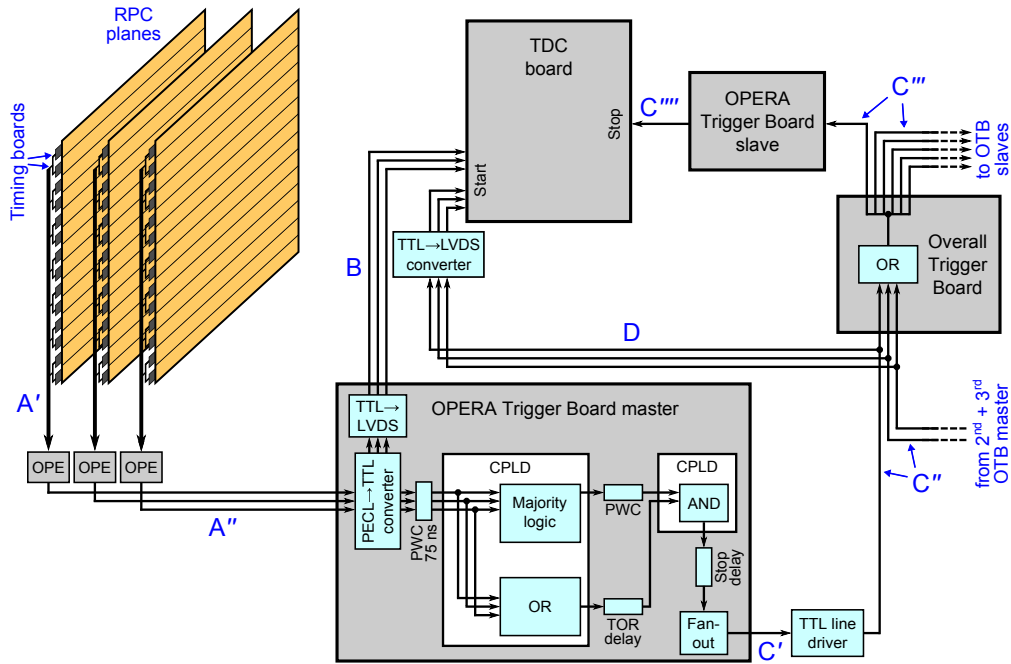
---

^{2} OR plane electronics

Figure 4.4: Schematic overview of one trigger station and an Overall Trigger Board. There are three trigger stations per SM, sharing one Overall Trigger Board which distributes the common stop signal to all six OPERA Trigger Board slaves of the same SM. For the sake of clarity, the figure only shows one of the two slave boards of the trigger station and only one TDC board. Each slave board can supply up to nine TDC boards with the stop signal. The OPERA Trigger Board master and slave, as well as the Overall Trigger Board are also shown in a simplified way. For detailed block diagrams of these boards see Figures 4.8, 4.9 and 4.11.

OPE outputs are PECL[3] signals, transmitted over twisted pair cables (A″ in Figure 4.4) to the OPERA Trigger Board (OTB) master. Both the plane OR signals and the individual timing board signals are forwarded to the OTB master. At its input stage the signals are converted to TTL[4]-compatible logic levels. Via TTL to LVDS converters and twisted pair cables (B in Figure 4.4) the plane OR signals are transmitted to free input channels of the same TDC boards, which are used for the readout of the drift tubes. The measurement of the arrival time of the trigger plane signals enables the determination of the chronological order in which the signals reach the OTB master. Moreover, it facilitates the measurement of propagation delays of the signal paths (see

---

[3] Positive emitter-coupled logic, a standard for differential signaling, using a common-mode voltage of about 3.8 V and a differential voltage of about 800 mV

[4] Transistor-transistor logic, a class of digital integrated circuits, using a supply voltage of 5 V, a voltage level of 0 V–0.8 V for logic 0 and 2 V–5 V for logic 1

Chapter 5) and, once calibrated, a time of flight measurement within the spectrometers. Also, 12 out of the 14 individual timing board signals are passed on to TDC boards. The signals from the topmost and the bottommost timing boards are discarded because the TDC boards only have input connectors for 12 channels.

The OTB master offers a variety of settings, in particular a choice of different trigger conditions (see Section 4.1.2). When the required condition is fulfilled, a trigger signal is generated and sent through a TTL fan-out over a 10 cm long coaxial cable[5] (C′ in Figure 4.4) to a TTL line driver. In the original design of the trigger system it was intended for each trigger station to produce a stop signal only for its two corresponding drift tube walls [Z$^+$05], using coaxial cables of 1 m in length. In the implemented setup the OTB master output signals are sent over 15 m long coaxial cables (C″ in Figure 4.4), necessitating the use of additional TTL line drivers. For details on all characteristics and features of the OTB, see Section 4.1.2.

The output signals of all three trigger stations of the same SM are collected at the Overall Trigger Board (OVTB) where the logic OR of the signals is built (see also Section 4.2.2). The OR signal is sent over a fan-out and 15 m long coaxial cables (C‴ in Figure 4.4) to all six OTB slaves of the same SM. Each slave board converts the incoming TTL signal again to LVDS and distributes the signal to all TDC boards plugged into the same electronics crate as the OTB slave.

Despite being separate boards with unconnected circuits, the master and the slave section of the OTB are both integrated in the same printed circuit board. There are six of these boards per SM, one in each electronics crate housing TDC boards and OSUBs. All six OTB slave sections are in use to distribute the stop signals over the crates' backplanes, but only three of the master sections are utilized, matching the number of trigger stations in each SM. The remaining three OTB masters are idle and are kept as potential replacement for broken boards.

Each OTB is plugged into the central slot of the crate (see Figure 4.5). Up to nine TDC boards are housed in the same crate, left and right of the OTB. The TDC boards receive the common stop signal through the crate's backplane, where twisted pairs of conductors (C⁗ in Figure 4.4) connect the OTB slave with all slots assigned to TDC boards. These twisted

---

[5] All coaxial cables used for the trigger system are from the manufacturer LEMO and have LEMO 00 connectors.
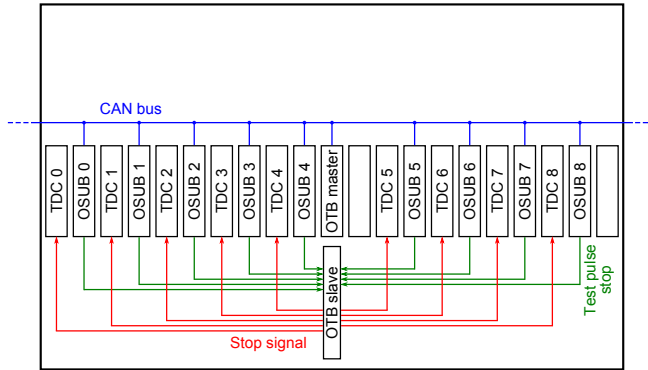
Figure 4.5: Crate backplane: The stop signal is distributed from the OTB slave to all TDC boards in the crate via twisted pairs of conductors. The maximum difference in length between these cables is below 18 cm. The connections between the OSUBs and the OTB slave are used for the OSUB test pulse feature.

pair cables vary slightly in length, depending on the distance of the TDC board slot from the central slot. The maximum difference in cable length is below 18 cm. The OSUBs are also connected with the OTB slave through the crate's backplane. When the OSUB test pulse feature is invoked by a CAN[6] bus command, the OSUB generates a stop signal which is sent over the backplane to the OTB slave and from there distributed to the TDC boards the same way as the stop signals coming from the trigger system [Göl12].

4.1.1   Timing Boards and OPE Boards

The signals on the RPC/XPC readout strips are picked up by the interconnection boards (see Section 3.2.3). Each board is connected to 16 readout strips and relays their signals to two different output connectors. One is for the twisted pair flat cable that directly transfers the signals to the readout electronics for the tracking. The other connector is a socket on which the timing board is mounted. For each of its 16 channels the timing board has a MAX4412[7] operational amplifier with a high-impedance input for minimum degradation of the signal used for the tracking. The amplified signal is sent to a MAX9010 high-speed comparator, acting as a discriminator with an adjustable threshold. Subsequently, the logic OR of all signals on the 16 channels is built, shaped to a pulse width of 200 ns and sent as LVDS output over a twisted pair cable to the OPE board [C+09].

---

[6] Controller Area Network

[7] Vendor: Maxim Integrated Products, USA

The OPE boards are located inside electronics racks on top of the OPERA detector. In addition to delivering the signals from the trigger planes to the OTB master, they have several tasks related to the timing boards. Each OPE board is connected to 14 timing boards. The input signals are processed by LVDS receivers before their logic OR is built. The OR signal as well as the signals on all 14 channels are output as PECL signals with a pulse width around 110 ns and are transmitted via twisted pair flat cable to the OTB master. The OPE contains electronic scalers to count the rates of the signals [F$^+$09]. It also provides the power supply for the timing boards and a DAC/ADC[8] logic to set and readout their discriminator thresholds. Moreover, the OPE can send test pulses to each individual timing board, which are transmitted to the inputs of the operational amplifiers and therefore take the same path as the signals coming from the detector through the interconnection board. The OPE itself is operated by the RPC slow control system over a CAN bus [C$^+$09]. This way, the timing board thresholds can be set and read out, test pulses can be generated, and the values of the OPE scalers can be read out and stored in the slow control database.

Only half of the readout strips of the designated RPC/XPC planes contribute to the trigger system: from the RPCs the y-coordinate (horizontal strips), and from the XPCs the u-/v-coordinate of XPC 1/XPC 2 respectively are used. All these signal strips are accessible from the sides of the detector, even after the installation of all detector components. The interconnection boards for the signal pick up on the vertical RPC strips are on top of the detector planes and inaccessible since the installation of the magnets' top return yoke. And the connectors for the v-/u-coordinate of XPC 1/XPC 2 respectively are on the top and bottom of the XPC planes and more difficult to access than their counterparts on the sides, so they were also not considered for the installation of the trigger system electronics. The exact distribution of the timing boards on the XPCs is shown in Figure 4.6. It is exactly the same for both SM. As XPC 1 is located directly behind the target it is smaller in width to allow for enough clearance for the BMS to reach all target walls. 27 timing boards are installed to read out the 416 slanted signal strips, which cover the whole surface of XPC 1. Two timing boards (TB 1 and TB 27) are connected to only eight channels each. XPC 2 is equipped with 28 timing boards, of which TB 14 and TB 15 are each connected to eight channels only. The lowest eight signal strips on the rock side and the highest eight on the corridor side are not read out by a timing board [S$^+$08]. The fraction of the area not covered for the generation of a trigger signal corresponds to 1.2 ‰ of the XPC 2 surface. As the OPE boards can handle only up to 14 timing

---

[8] DAC: digital-to-analog converter, ADC: analog-to-digital converter
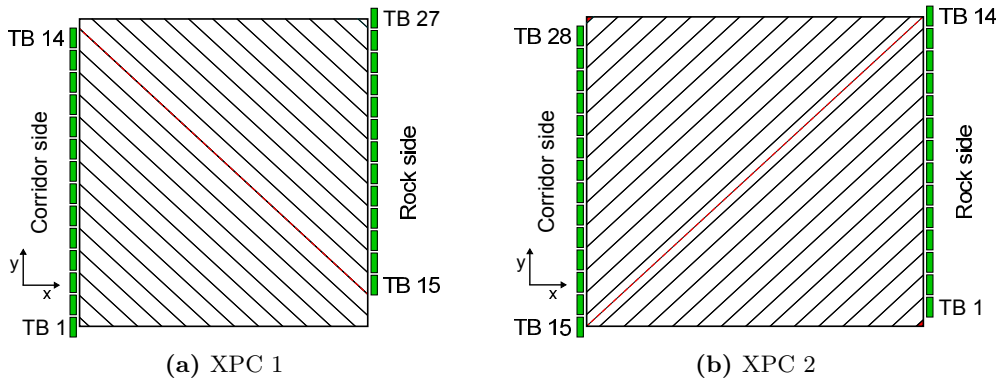
(a) XPC 1　　　　　　　　　　　**(b)** XPC 2

Figure 4.6: Timing board (TB) distribution on the XPCs. It is exactly the same for both SM. The lower rock side corner and upper corridor side corner of XPC 2 are not covered by timing boards [S+08].

boards, there are two OPE boards for each XPC, one for the corridor side and one for the rock side timing boards. For the RPCs one OPE board per plane is sufficient, since each of the seven rows of RPC detector units has 32 horizontal readout strips, so that one timing board is connected to half an RPC row for a total of 14 boards on each trigger plane. As it was not possible to install all timing boards on the designated RPCs planes and in a fully symmetric pattern, in some cases they had to be relocated. Their position was shifted horizontally, so that all trigger planes still cover the whole detector surface in the xy-projection and remain sensitive to tracks in z-direction. The exact positions in which the timing boards are installed on the RPCs are shown in Figure 4.7. They differ slightly for the two SMs. Note that in SM 2 there are no timing boards installed on RPC 11, the plane originally being designated as a trigger plane (see Figure 4.3). Instead all timing boards had to be moved to RPC 9 and RPC 10. Regardless of any shift of positions in z, all timing boards on the RPCs are installed on the corridor side.

4.1.2　OPERA Trigger Board

The OTB master has five input connectors for twisted pair flat cables. For the first trigger station of each SM all inputs are used, since each side of the two XPCs is read out over individual cables and the fifth cable comes from the one RPC plane. For the other trigger stations, which use the signals from three RPC planes, two of the input connectors are left empty. First, the signals are converted from PECL to TTL (see Figure 4.8). To transmit the OTB input signals to TDC board input channels for timing measurements, the signals are fanned out to TTL to LVDS converters and relayed to output connectors. The plane OR signals are sent over one twisted pair flat cable, and the individual
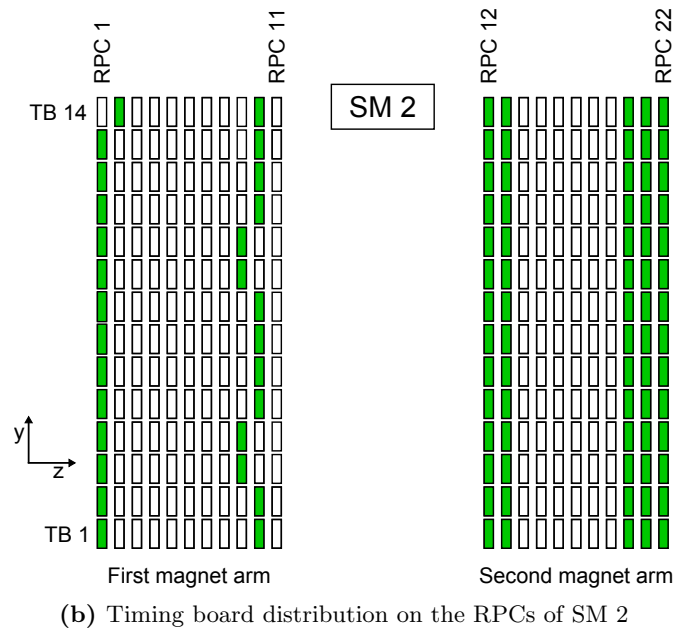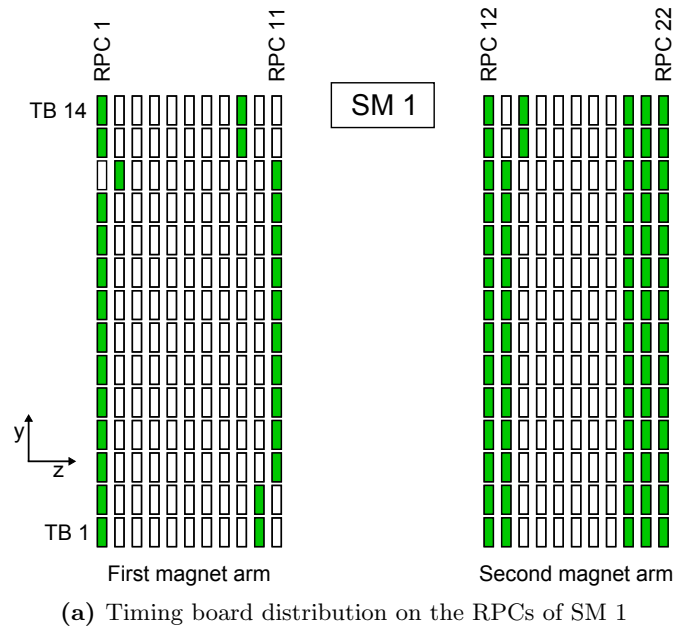
(a) Timing board distribution on the RPCs of SM 1

(b) Timing board distribution on the RPCs of SM 2

Figure 4.7: Timing board distribution on the RPCs. The boards had to be installed in slightly different positions in the two SMs. All timing boards on the RPCs are installed on the corridor side (figure adapted from [S⁺08]).

signals from 12 out of 14 timing boards per trigger plane are sent over separate cables. On the OTB master the TTL signals are shaped to a pulse width of

75 ns (see also Section 4.2.1) before they pass through a CPLD[9]. The CPLD contains a mask stage, where each individual channel can be masked, either to stop the trigger signal flow during installation and testing or to permanently deactivate the two unused channels in the second and third trigger station of each SM. By default, all channels are masked, in order to prevent possible bursts of trigger signals after a power cycle of the OTB. Following the CPLD is a programmable delay line that can be used to delay the signals on individual channels to compensate for potential differences in propagation delays. During detector operation all five delay values (CE0 to CE4 in Figure 4.8) were set to zero at all times. As a next step, the signals enter the CPLD again, where the majority logic is implemented. Four different trigger conditions can be selected: 2 out of 3, 3 out of 4, 4 out of 5 or a random trigger (one signal on any of the five channels). For the trigger stations using XPC signals, the CPLDs are programmed with an additional feature. Before entering the majority logic, the signals from the two sides of each XPC are passing through an OR gate. This way, the number of signals evaluated by the trigger logic is reduced to three, matching the number of physical trigger planes.[10] During all OPERA runs since the beginning of 2008 all trigger stations were operated with a 2 out of 3 majority, so that any two coinciding signals out of the three signals entering the majority logic generated a trigger signal. A coincidence is given whenever there is any kind of overlap of the two signals. The resulting majority output signal (MOUT in Figure 4.8) is shaped to a defined width between 0 and 255 ns by a programmable pulse width controller (PWC) and is then labeled MIN. To preserve the timing information of the first signal that arrives at the OTB, all signals TR0 to TR4 are also fed into an OR gate on the CPLD, in parallel to the majority logic. The first signal passes the OR and is then delayed by a programmable delay line. The output of the delay line is labeled TORIN and is transmitted together with the signal MIN to another CPLD with an AND gate. If the width of the MIN signal (CE7 in Figure 4.8) and the size of the delay (CE5) are chosen adequately, the output signal TROUT of the AND gate is generated when the signal TORIN arrives at its input. This way, the exact moment, when the trigger signal is produced, does not depend on the arrival time of the second signal, which fulfills the trigger condition. Instead, the trigger signal is always issued a fixed time interval after the first signal has reached the OTB.

---

[9] Complex programmable logic device, an integrated circuit device with non-volatile memory. CPLDs are functional directly after power-on and are mainly used as programmable logic gates.

[10] This feature is not shown in Figure 4.8. For the trigger stations with XPCs the logic OR of the signals TR1 and TR2 and of the signals TR3 and TR4 are built. The majority logic then evaluates the signals TR0 (from the RPC plane), TR12 and TR34.
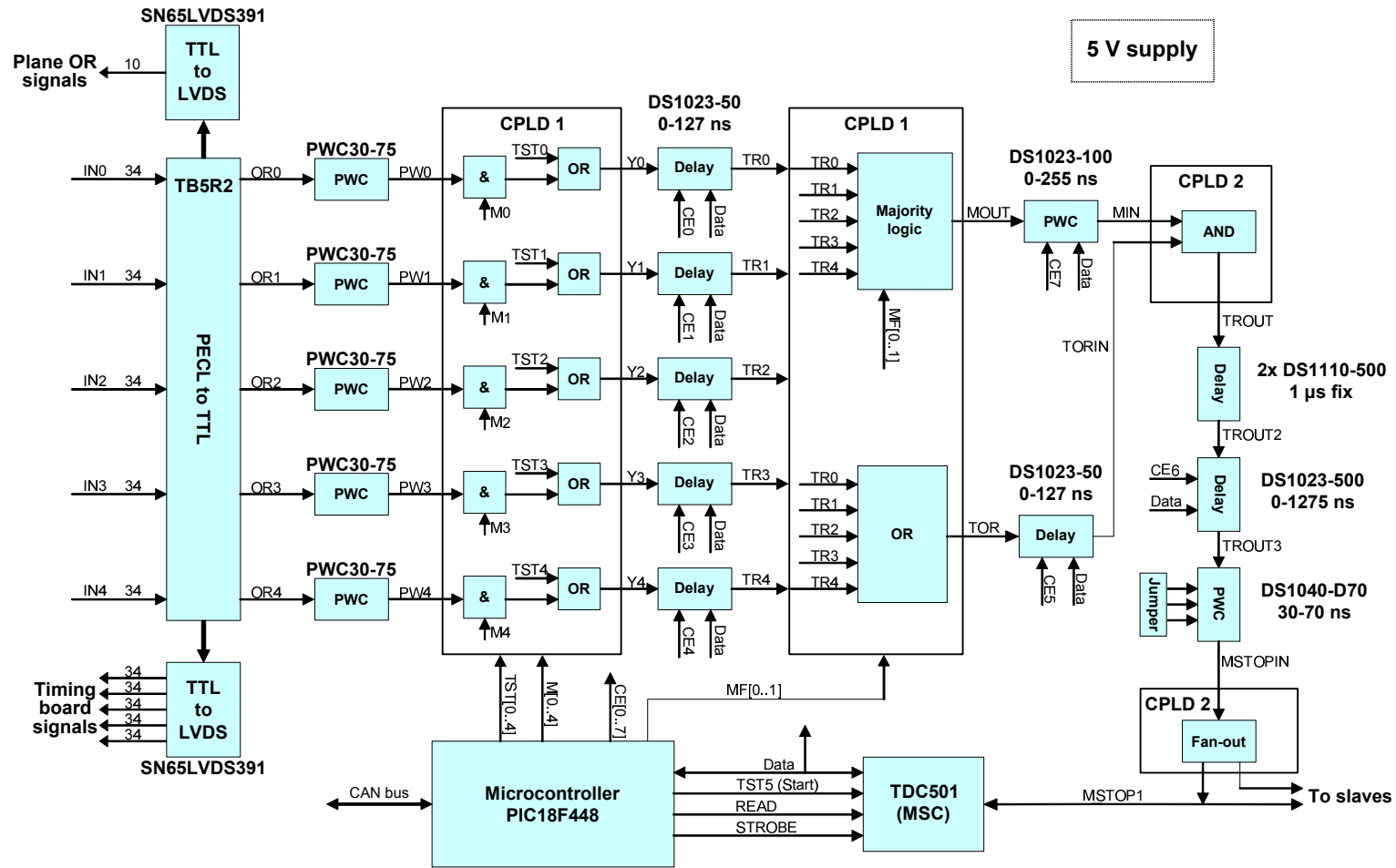
Figure 4.8: Block diagram of the OTB master for a trigger station using input signals from three RPC planes (figure adapted from [F⁺09])

The maximum delay between the signals from two different trigger planes within the same trigger station occurs, when a charged particle crosses the detector diagonally, so that the track has a maximal elongation in x and y and crosses the first plane close to a timing board and the second plane near the far end, more than eight meters away from the timing board. In this case, the particle's time of flight between the two planes and the signal propagation time on the second plane's readout strip add up to about 75 ns. Accordingly, a pulse width of this value was chosen for the shaping of the input signals on the OTB, so that tracks with the greatest possible signal delays between trigger planes can still fulfill the majority condition. Signals with even greater delays, which cannot be induced by the same particle, are ruled out, because their 75 ns wide signals do not overlap inside the majority logic.

For all OPERA runs a value of 200 ns was chosen for the pulse width of MIN and one of 105 ns for the delay of TOR. If the two signals that fulfill the majority condition arrive simultaneously at the OTB, the TORIN signal is released approximately in the middle of the 200 ns time interval. If the two input signals are as much as 75 ns apart, then the TORIN signal is transmitted about 30 ns after the leading edge of the MIN signal. This leaves a sufficiently long time interval to account for possible inaccuracies in the settings or propagation delays of any electronics components and to ensure that the TORIN signal is never released before the MIN signal.

The TROUT signal is passing through three delay lines, two with a fixed delay of 500 ns each and one with a programmable delay of up to 1275 ns. The width of the stop signal can be selected between 30 ns and 70 ns in steps of 10 ns by placing the appropriate jumpers on the OTB master. Until 13 November 2008 the pulse width of the OTB master output was set to 50 ns, and it was then changed to 70 ns for the first tests of the OVTB and for all following runs (see Section 4.2.2). On the second CPLD, in addition to the AND gate, a fan-out is implemented, transferring the signals to two LEMO output connectors and an on-board TDC chip. The settings of all programmable devices on the OTB master are controlled by a microcontroller[11], which is operated by the slow control system via a CAN bus[12]. The microcontroller also features the possibility to generate test pulses for measuring the signal propagation time on the circuits of the OTB. Test pulses are sent to the on-board TDC to start the time measurement, and are simultaneously fed into the first CPLD, just behind the mask stage. From there the signals take the same path as signals coming from the detector. The TDC measurement is

---

[11] PIC18F448, Microchip Technology Inc.

[12] For details on the slow control system and software see [Göl06].

stopped when the stop signal produced by the test pulses is fanned out by the second CPLD. This way, the signal delay of each OTB master can be measured in-situ with nanosecond precision, excluding the delays of the PECL to TTL converter, the input pulse width controller and the mask stage, but including all adjustable delay lines and pulse width controllers. The TDC is read out by the microcontroller and the measured values are stored in the slow control database.

The OTB slave has a LEMO input connector, over which it receives the TTL stop signal from the OVTB (see Section 4.1). Over the crate backplane, also the OSUBs can send stop signals to the slave board as part of a test pulse feature for the verification of the readout functionality for the drift tubes (see Figure 4.5). The logic OR of the stop signals from the master board and from up to nine OSUBs is built inside another CPLD and is passed on to a fan-out with a ninefold output. After conversion from TTL to LVDS the stop signal is distributed over the crate backplane to up to nine TDC boards (see Figure 4.9).
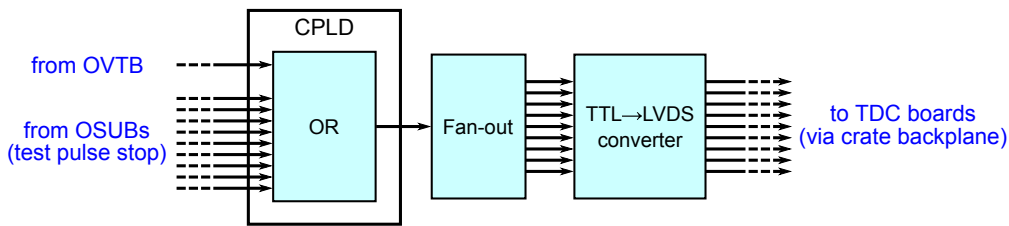

Figure 4.9: Block diagram of the OTB slave. The slave board manages the distribution of stop signals coming either from the OVTB or from the OSUBs of the same crate, when test pulses are generated.

The settings of all adjustable components on the OTBs over the time of the OPERA physics runs are listed in Table 4.1, including the few changes applied in 2008. The values for the runs 2009–2012 were constant and are listed in the last column.

4.2   Hardware Modifications

The installation of the drift tube detector was completed in 2007, and several short commissioning runs with and without CNGS beam took place in the years 2006 and 2007. The first physics run started on 18 June 2008. During the commissioning phase, and in the case of the OVTB and the LVDS converters also after the start of the physics program, some changes have been made to

the trigger system in order to improve its performance or to correct technical defects. These hardware modifications and the times they were implemented are described in the following four sections.

Table 4.1: Settings of all adjustable components on the OTBs over the time of the OPERA physics runs (18 June 2008 to 3 December 2012, with interruptions during winter). The devices and signals are named according to the labels in Figure 4.8. For the second and third trigger station in each SM, the unused fourth and fifth input channels were masked at all times (M3 and M4).

	16 June 2008 − 8 July 2008	9 July 2008 − 12 Nov. 2008	13 Nov. 2008 − 3 Dec. 2012
TR0–TR4 delay	0	0	0
Majority logic	2 out of 3	2 out of 3	2 out of 3
MIN pulse width	200 ns	200 ns	200 ns
TOR delay	105 ns	105 ns	105 ns
TROUT3 delay 1 / 1 [†]	485 ns	490 ns	490 ns
TROUT3 delay 1 / 2	490 ns	490 ns	490 ns
TROUT3 delay 1 / 3	495 ns	495 ns	495 ns
TROUT3 delay 2 / 1	490 ns	490 ns	490 ns
TROUT3 delay 2 / 2	480 ns	480 ns	480 ns
TROUT3 delay 2 / 3	500 ns	500 ns	500 ns
MSTOPIN pulse width	50 ns	50 ns	70 ns

[†]Notation: SM number / number of the trigger station in the corresponding SM

4.2.1   Pulse Width Controllers

During the commissioning runs in March/April and July 2007 the width of the trigger signal from RPC 22 in SM 1 (see Figure 4.7) was monitored [Ste08]. The signal width was deduced from the time distribution of the corresponding plane OR signal with respect to the common stop signal. The timing was measured with a TDC board, using the signal path B in Figure 4.4. It became apparent that the signal width was not constant in time but underwent several changes between the values of 113 ns and 150 ns. Similar effects were seen on further trigger planes as well. Since the origin of these changes remained unknown, pulse width controllers were installed on the OTB masters, shaping all input signals to 75 ns, independent from their initial pulse width, to guarantee a constant timing for the trigger system (see Section 4.1.2). This way, the programmable pulse width of the MIN signal and the delay of the

TOR signal (see Figure 4.8) could be set to constant values of 200 ns and 105 ns respectively, without risking to loose trigger signals, should the input signal widths be too small, or to generate the trigger signal too late, should the input signal width be larger than the TOR delay. All OTB masters were equipped with pulse width controllers before the beginning of the 2008 physics run, and have worked without malfunction since.

4.2.2 Overall Trigger

The geometrical acceptance of an RPC plane is about 97 % on account of several areas being insensitive to crossing particles, e.g. the rims of the 21 individual RPCs, the holes left for the magnets' supporting bolts, or the polycarbonate spacers inside the chambers (see Section 3.2.3). The RPCs are identical in structure and aligned along the z-axis direction, because the RPC rows are suspended by the same supporting bolts going through the iron slabs of each magnet arm. Therefore, the areas causing the reduced acceptance are also aligned in z, so that particle trajectories at a small angle to the z-axis, e.g. trajectories of CNGS beam induced particles, have an increased probability of crossing insensitive areas in several neighboring planes. If a particle fails to produce a signal in just two trigger planes of the same station, the generation of a trigger signal in that station is already impossible. For particles coming in at greater angles to the z-axis, e.g. atmospheric muons, the timing board distribution over more than three RPC planes in several of the trigger stations implicate further gaps (see Figure 4.7[13]). Moreover, the actual efficiency of any individual RPC or XPC plane can drop far below the value of 97 % due to the loss of readout channels, short circuits in the high voltage supply, or inhomogeneities in the surfaces of the resistive plates, leading to areas with reduced or even no particle detection sensitivity. Should planes contributing to the drift tube trigger system be affected by such deterioration, the efficiency of the trigger would also be diminished. To counter these effects, the trigger system was modified and supplemented with the so-called overall trigger. Instead of giving a trigger signal only to the two drift tube planes closest to the trigger station which generated it, the trigger signal from any of the three stations in each SM is distributed to all six drift tube planes of the same SM. So if, for example, a charged particle crosses four drift tube planes, but only one trigger station fires, then still all drift tubes are read out due to the distribution of the stop signal to all TDC boards of the corresponding SM.

---

[13]Note that for illustrative purposes concerning the timing board distribution Figure 4.7 is not to scale. The width in z-axis direction of the gas-filled chambers is only 2 mm, whereas the chambers in neighboring planes are 68 mm apart in z. Therefore, the gaps for trajectories at large angles to the z-axis are much larger than they appear in the figure.

The downside to one common stop signal per SM is an increased spread of the time distribution of the trigger signal with respect to the particles' arrival times at the drift tubes. If the readout of a drift tube plane is not triggered by the closest trigger station, but by another one further away, then the particle's time of flight between the RPC/XPC plane, which generated the trigger signal, and the drift tube plane, which is read out, is increased compared to individual trigger signals for each station. This has to be considered and corrected in the PT track reconstruction software. In case of a misidentification of the trigger signal generating plane, the consequentially assigned time of flight correction is calculated wrongly and decreases the spatial resolution of the drift tubes.

The first implementation of the overall trigger was done in 2007, using NIM[14] components. A schematic overview of the NIM overall trigger is shown in Figure 4.10. The TTL outputs of all three OTB masters of each SM were transmitted via coaxial cables to TTL to NIM converters before the logic OR was built. The output of the NIM logic unit was shaped to a pulse width of 80 ns and relayed to a fan-out unit and a counter. The counter was used to visually monitor the overall trigger rate. The six fanned out signals were converted back to TTL levels and transmitted via coaxial cables to all OTB slaves of the same SM. Two of these NIM setups were installed on the OPERA detector, one for each SM. They were in use during the last commissioning runs in 2007 and during the entire CNGS beam run of 2008.
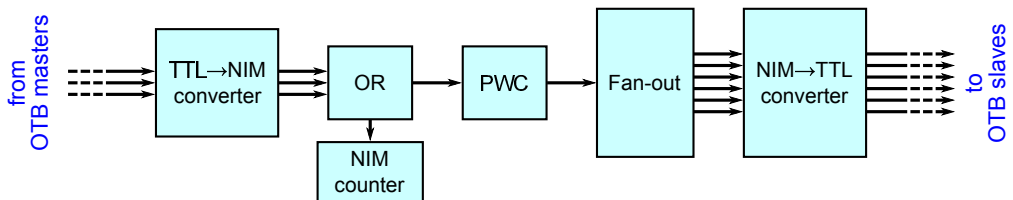

Figure 4.10: Block diagram of the first overall trigger implementation, using NIM components

In 2008 dedicated printed circuit boards were developed to replace the NIM electronics components and to add further functions to the overall trigger (for details see [Jes09]). The OVTB has an input stage for up to seven TTL signals (see Figure 4.11), requiring a pulse width of at least 60 ns. For this

---

[14]Nuclear Instrumentation Module, a standard for electronics components first used in nuclear and high-energy physics, defining both electrical and mechanical specifications
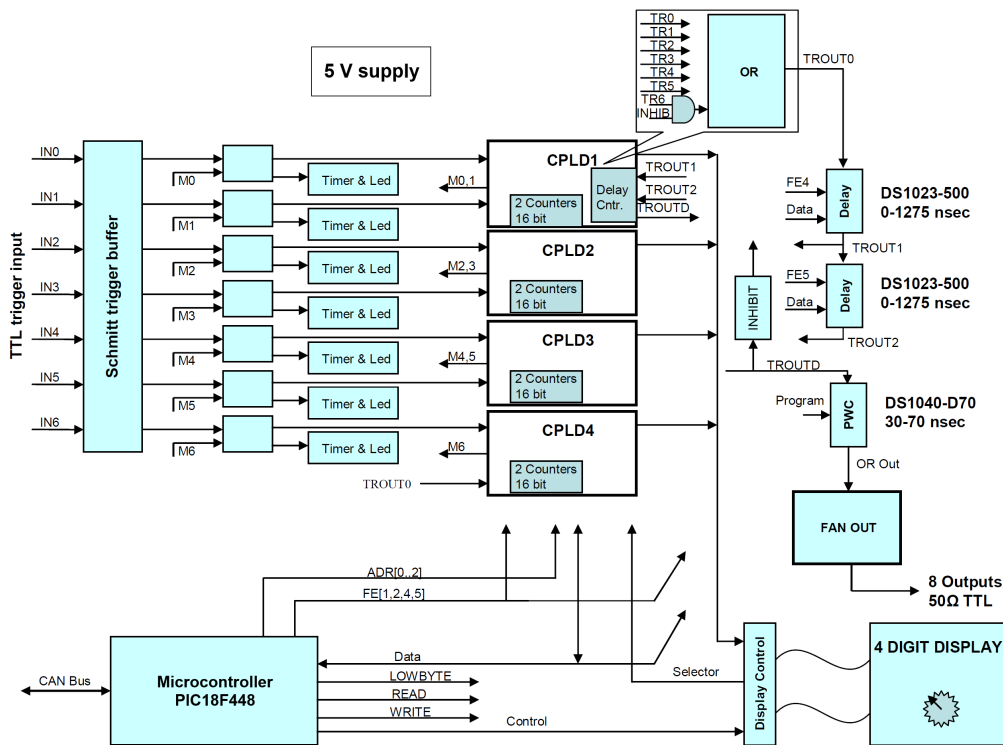
Figure 4.11: Block diagram of the OVTB (figure adapted from [Sch09])

reason, the width of the OTB master output signals was changed from 50 ns to 70 ns when the OVTBs were installed (see Section 4.1.2). Each input channel can be disabled by a programmable mask stage, an LED[15] indicates each enabled input. A second LED per channel signals incoming pulses. Counters for all input channels and for the OVTB output are implemented on the four CPLDs. The logic OR of all seven input signals is built and can be delayed by programmable delay lines in steps of 5 ns up to a total of 2550 ns (FE4 and FE5 in Figure 4.11), adding to the intrinsic delay of the OVTB of 50 ns ± 1 ns [Jes09]. The OR signal is shaped by a programmable pulse width controller and fanned out to eight TTL outputs. Outgoing pulses are also visualized by a flashing LED for an easy on-site check of functionality. An external four-digit display shows the current value of any of the eight counters, selected using a rotary switch. By software control the display can be changed to frequency output instead. All programmable devices are controlled by a microcontroller which also reads out the counters. In the same way as on the OTB, the microcontroller itself is operated via CAN bus by the PT slow

---

[15]Light-emitting diode

control system. The counter readouts can be stored automatically in the slow control database at chosen intervals.

The two OVTBs were installed on 13 November 2008 after the end of that year's CNGS beam run. They were used for all data taking since, starting with a test run without neutrino beam until 20 November 2008. An additional feature of the OVTB, the so-called crossover trigger, is described in the following Section 4.2.3. Due to severe problems arising from the additional cable connection between the two SMs, this feature was disabled and the corresponding cables were removed shortly after the installation of the OVTBs.

The settings of the adjustable components on the OVTBs since their installation are listed in Table 4.2. With the exception of the disabling of the crossover trigger, the values remained constant during the runs 2009–2012.

Table 4.2: Settings of the adjustable components on the OVTBs since their installation. The signals are named according to the labels in Figure 4.11. The unused input channels IN3–IN5 were masked at all times. Channel IN6, dedicated to the crossover trigger, was masked since 3 July 2009. The current frequencies of all incoming and outgoing signals were automatically stored in the slow control database every second with 1 Hz accuracy since the OVTBs' installation.

|	13 Nov. 2008 – 3 July 2009	3 July 2009 – 3 Dec. 2012
TROUT1 delay	0	0
TROUT2 delay	0	0
INHIBIT delay	500 ns	—
OR Out pulse width	70 ns	70 ns

4.2.3   Crossover Trigger

The purpose of the crossover trigger was to further increase the trigger efficiency by interconnecting the OVTBs of the two SMs. In principle, triggering the readout of all twelve drift tube planes over a single OVTB with just one common stop signal is a feasible option. Nevertheless, it was not chosen, because it would have increased the average time of flight between the triggering plane and the drift tubes substantially, giving rise to a larger error on the spatial resolution of the drift tubes (see Section 4.2.2). Instead, each of the two OVTBs handles the trigger signals of the corresponding SM individually. But in addition to the three trigger station inputs per SM, the output of the first OVTB is connected via a 20 m coaxial cable to a fourth input channel of

the second OVTB and vice versa. Should one SM fail to produce a stop signal, a potential trigger signal from the other SM guarantees the drift tube readout for the entire detector. Despite the increased time of flight in such cases, a crossover trigger signal then constitutes a gain in data quality, since without it, one of the SMs would not be read out at all. The signal propagation delay on the coaxial crossover cables of about 100 ns is larger than the maximum possible time of flight between the two spectrometers plus a potentially longer propagation time on the RPC/XPC strips of the trigger planes in SM 2 along the particle flight path. This ensures that the crossover trigger signal is only a fall-back option and that the two SMs are triggered individually if they each generate their own trigger signal. To prevent the crossover signal from causing a feedback loop, it is relayed to a special input channel (IN6 in Figure 4.11). Signals on this channel do not enter the OR logic directly, but through a logic AND gate together with the logic NOT of a second signal. This so-called INHIBIT is branched off when an OR signal is generated and redirected to the inverter input of the AND gate. The inverted INHIBIT disables the input for the crossover signal from the other SM. Its level is kept high for a programmable period of time. The delay for the trailing edge of the INHIBIT has to be longer than the propagation delay of the returning crossover signal from the other OVTB on the coaxial cables and electronics circuits to avoid a feedback loop. For details on the crossover trigger see [Jes09][16].

The two coaxial cables were installed together with the OVTBs on 13 November 2008, and the crossover trigger was activated. Due to different ground levels of the two OVTBs, which are housed in separate electronics crates on the top platform of the OPERA detector, the cable connection between them led to uncontrolled effects on the boards, causing a severe reduction of the trigger efficiency in SM 2. Figure 4.12 shows the average trigger efficiency for each of the six trigger stations with a bin width of twelve hours. Each bin corresponds to a so-called extraction, the data output of half a day of detector operation. In Figure 4.12a the last 13 days of the 2008 run are shown, and in Figure 4.12b the first 31 days of the 2009 run. In between the two runs were several months of beam and detector shutdown. The efficiency drop at the end of the 2008 run, when the OVTBs were installed, can clearly be seen for all three trigger stations of SM 2. Unfortunately, this effect remained unnoticed during the short test run, since it had no visible impact on the trigger rates, which were monitored during the test. The trigger rates are highly dominated by random coincidences due to noise in the RPC planes (see Section 4.1). The change in the general level of the trigger efficiency in SM 2 from 2008 to 2009 cannot be linked to any specific source. The trigger efficiency is dependent on

---

[16]In [Jes09] the crossover trigger is referred to as "X-Trigger".
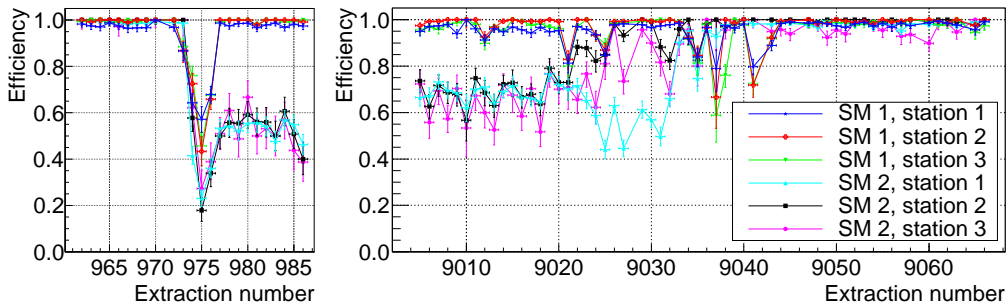
(a) Final 13 days of the 2008 cosmic run (8 to 20 November 2008)

(b) First 31 days of the 2009 run (1 June to 1 July 2009). From extraction 9024 to 9042 several tests on the trigger system were conducted, manipulating the trigger efficiency values.

Figure 4.12: Average trigger efficiency for each of the six trigger stations during the time the crossover trigger was activated. A so-called extraction is the data output of twelve hours of detector operation.

the efficiency of the RPCs and XPCs, which in turn vary strongly with changes in the number of functional readout channels, the high voltage supply, or the gas density and quality inside the detector planes. A detailed description of the definition and determination of the trigger efficiency is given in Section 4.3.

When the drop in efficiency of roughly 30 % became apparent at the beginning of the 2009 run and the link to the crossover trigger was discovered on 19 June 2009 (corresponding to extraction 9042, see Figure 4.12b), the crossover feature was deactivated through the slow control system. After the deactivation, the efficiencies went back to the same values as before the OVTB installation. On 3 July 2009 on-site measurements revealed the existence of ground loops between the two OVTBs [Pao09]. Bipolar signals of up to $\pm 300 \, \text{mV}$ between the ground of the OVTB in SM 1 and the outer conductor of the unplugged crossover trigger cable from SM 2 were measured using an oscilloscope. The noise signals in the opposite direction (SM 2 OVTB to SM 1 crossover cable) reached up to $\pm 450 \, \text{mV}$. Although the software deactivation of the crossover trigger was sufficient to bring the trigger efficiencies back to the required level, the two crossover cables were unplugged at both ends to rule out any further negative effects due to the ground loops.

Any data affected by the uncontrolled functioning of the crossover trigger is not considered for the trigger calibration (see Chapter 5). This applies to the trigger time recordings for extractions 973–987 and 9000–9042. As a precaution, the extractions 9043–9070 are also omitted for the analysis within this thesis in order to avoid any potential influence of the deactivated but still installed crossover trigger. If these datasets are used for any analy-

ses of the electronic detector data sensitive to the absolute interaction rate, the reduced trigger efficiency in this period of time has to be taken into account.

4.2.4 LVDS Converters

For one of the calibration steps it is essential to identify which of the three trigger stations in each SM generated the overall trigger signal for a specific event (see Section 5.4). To obtain this information, the arrival times of all OTB master output signals at the OVTB input have to be determined. This can be done by using the timing measurements of the trigger signals, which are branched off to the TDC boards. Here, the different propagation delays on the OTB masters, the TTL line drivers and the cables B, C′ and C″ (see Figure 4.4) have to be considered. But the uncertainty on the propagation delays on these long signal paths of the yet uncalibrated trigger system would make tight selection cuts necessary to securely identify the first signal and, as a consequence, would severely reduce the statistics for this calibration step. Therefore, an additional feature was installed in 2009: all signals coming from the three OTB masters are branched off directly before they enter the OVTB input. They are transmitted via 1 m coaxial cables (labeled D in Figure 4.4) to a small circuit board on which the incoming TTL signals are converted to LVDS. The circuit board is directly plugged into a free input connector of a TDC board, so that the converted signals are transmitted without any significant propagation delay. Since this signal path is very short and of equal length for all signals and contains no adjustable devices, the uncertainty on the chronological order of the signals is small, even if they arrive within a few nanoseconds (see Section 5.3). Thus it is possible to utilize a large number of signals for the calibration step described in Section 5.4.

The circuit board is connected via an external cable to the backplane power distribution of the crate, in which the TDC board is housed. The 5 V supplied by the crate are converted on the board to 3.3 V. The LVDS converter board shown in Figure 4.13 was produced as a spare part and is provided with an additional feature in contrast to the two boards installed at the OPERA detector. Next to the two four-channel differential line drivers[17] (labeled B), converting the TTL input signals (A) to LVDS levels for the output (C), the circuit board also contains a differential receiver[18] (E). An LVDS signal, which is fed into the 23rd and 24th position (D) of the ribbon cable socket, is converted to TTL levels and output over an extra LEMO 00 connector (F).

---

[17]Texas Instruments SN65LVDS391

[18]Texas Instruments SN65LVDS33

This feature was used for calibration measurements on twisted pair ribbon cables (see Section 5.3).
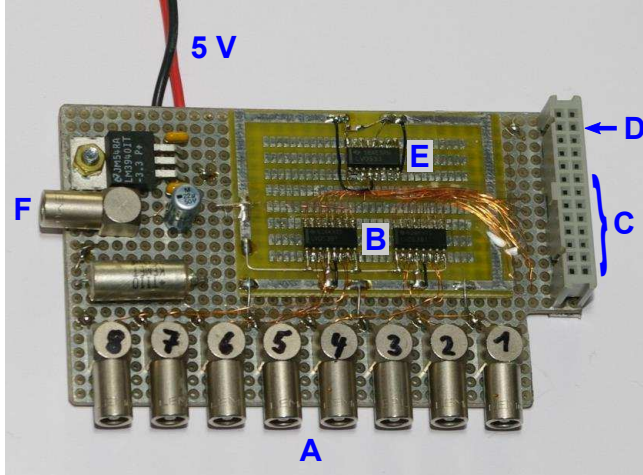

Figure 4.13: Circuit board with eight LEMO 00 input connectors (A), two four-channel differential line drivers (B) and eight LVDS output channels (C). The LVDS to TTL conversion feature (D, E and F) added to this specific board was used for calibration measurements on twisted pair ribbon cables.

To make the OVTB timing information accessible for analysis in the OPERA software, the classes `SOverallTriggerDigit` and `RSOverallTriggerDigit` were added to the `OpData` and `OpRData` packages respectively. `OpData` is the package for the transient data, used inside the analysis software framework, while `OpRData` is used for the persistent data stored in `ROOT`[19] format. Since the two classes have the same general functionality, only the members of the `OpData` class are listed here. The data is made available in a `TList`. For each entry of the list, the SM number is stored in `Int_t m_sm` with the values 1 or 2, the number of the trigger station in `Int_t m_overallTriggerCh`, ranging from 1 to 3, and the time in nanoseconds in `Float_t m_time`. As for the drift tube data, the value t of `m_time` is converted in the way

$$t = 2000\,\text{ns} - t_{TDC}, \tag{4.1}$$

where t_{TDC} is the time interval measured from the start signal at the TDC board input channel to the arrival of the delayed common stop signal. Therefore, the signal reaching the TDC board first, has the smallest value of `m_time`. The structure and functionality of the OPERA software is described in more detail in [Won07].

The LVDS converter boards were installed at the beginning of the 2009 run and are delivering data since extraction 9039 (17 June 2009).

---

[19]ROOT is a data analysis framework developed by CERN.

4.3 Trigger Efficiency

The trigger efficiency is the percentage of a defined category of events for which a trigger signal is generated. It can be used as an indicator for the functionality and performance of the trigger system and the drift tubes. The loss of a trigger plane or a drift tube plane causes a visible reduction of the efficiency. During the OPERA detector runs the trigger efficiency was determined for each trigger station and data extraction, that is twice a day, and if the value for any station dropped below a specified threshold, a warning was issued by the slow control software. This way even small hardware failures were noticed with a maximum delay of about twelve hours. In addition to its use as a monitor for the stability of the detector operation, the knowledge of the trigger efficiency is essential for all analyses that are based on absolute numbers or ratios of certain event types using the PT data or the trigger time information.

To calculate the trigger efficiency for a specific station, the number of events with one or more tracks crossing the corresponding pair of drift tube walls (see Figure 4.3) has to be determined. The OPERA reconstruction software uses a Kalman algorithm to reconstruct tracks in two projection planes, the xz- and the yz-plane. Within the software a detector hit in one projection plane is called a "digit". In order to identify tracks passing through a pair of drift tube walls, Kalman tracks containing at least one digit with a lower z-coordinate than the drift tubes, and one or more digits with a higher z-coordinate are selected. Since the different electronic detectors have different dimensions in x and y, a further test is necessary to determine if a track actually crossed a particular PT wall. Therefore, a linear regression with all digits of the respective Kalman track, except for any potential PT digits, is performed.[20] For each drift tube wall a test plane is defined: in z the plane is in the middle of the wall, between the second and the third layer of drift tubes, in y it has the same dimensions as the drift tubes, and in x it extends to the tangent to the two outermost tubes. A track intersecting this plane crosses at least one drift tube of the corresponding wall. If the straight line resulting from the linear regression intersects at least one of the planes of a pair of drift tube walls, the event is selected and the denominator for the calculation of the trigger efficiency of the respective trigger station is incremented by one. If also a minimum of one drift tube digit is recorded for the same drift tube walls, the

---

[20]The fact that the tracks of charged particles passing through the detector are never linear but slightly deflected by scattering and the spectrometers' magnetic fields is ignored at this point. For the purpose of determining if a track crosses a drift tube wall, this approximation is sufficiently accurate.

enumerator is incremented by one as well. The resulting fraction for all selected events in a chosen time interval is the trigger efficiency for the respective station.

However, this method does not work for the very last trigger station in beam direction, since there are no further electronic detector planes behind the last pair of drift tube walls. It is therefore not possible to verify if a particle actually passed through these drift tubes without using the PT information itself. Here instead, only tracks are selected for which the last RPC plane[21] contributes at least one digit to the Kalman track. Additionally, the linear regression of the track digits is used to check whether the extrapolated straight line intersects at least one of the two PT planes. To test if this method yields similar results for the trigger efficiency of the last station as the method described above does for the other five stations, both methods are applied to the third station of SM 1. This station is almost equal in structure to the third station of SM 2 (see Section 3.2.3 and Figure 4.7). Figure 4.14 shows the trigger efficiency of the third station in SM 1 during the OPERA run 2012. For testing the extrapolation method, a minimum of one digit in RPC 22 of SM 1 is required, and the linear regression is performed using only SM 1 track digits to replicate the setup of the third station in SM 2 as good as possible. Within the statistical error margins both methods give the same results, justifying the use of the extrapolation method for the last station of SM 2. As a side note, the sudden decrease of the trigger efficiency around extraction 12365 is due to the loss of two and a half timing boards distributed over all three trigger planes of the station.

Figure 4.15 shows the trigger efficiency for each of the six trigger stations during the detector runs 2009–2012. Extractions affected by corrupted data or documented interventions on the spectrometers are omitted. The numbers of all the extractions used for the calculation of the trigger efficiency are listed in Table C.1, all omitted extractions are listed in Table C.2.[22] The data includes both cosmic and ontime events. In 2009 (Figure 4.15a) the efficiency drops for several extractions down to 85–95 %. These incidents are not documented in the detector logbooks but are probably due to interventions on the spectrometers' hardware or the DAQ system. Since the beginning of the 2010 run, the efficiency of all trigger stations is stable at a level between 95–100 %. A small percentage of the tracks is always lost for the trigger because of the RPCs'

---

[21] RPC 22 (see Figure 4.3) is the last active plane inside the SM 2 magnet. Nevertheless, there is still a layer of passive material, i.e. one 5 cm iron slab, between this plane and the drift tubes. Therefore, a digit in RPC 22 does not guarantee that the track continues behind the magnet.

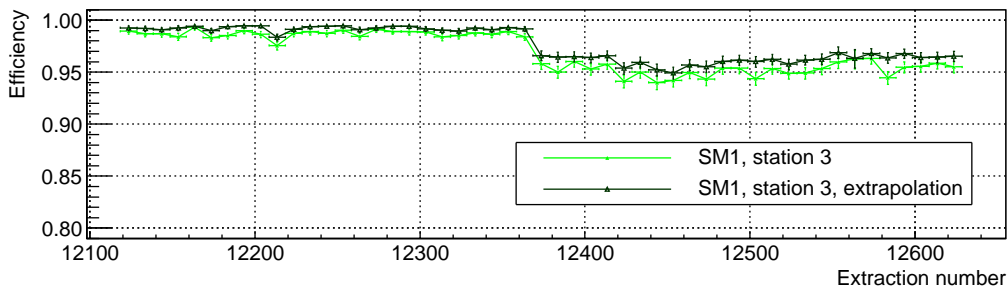[22] The same dataset is used for the calibration of the trigger system (see Chapter 5).

Figure 4.14: Trigger efficiency of the third station in SM 1 during the OPERA run 2012. Both methods described above are applied. The method necessary for the last station in SM 2 is labeled "extrapolation". The bin width is ten extractions, the error bars represent the statistical errors.

limited geometrical acceptance which is explained in Section 4.2.2. Over the years 2010 to 2012 a slight decrease of the overall trigger efficiency is visible. This can be attributed to a slow but continuous degradation of some of the RPCs and parts of the electronics. As the XPCs and RPCs are embedded in the detector structure in such a way that repairs or replacements after their installation are impossible, the areas becoming less efficient or failing completely add up over time.

In Figure 4.16 different hardware-related causes for inefficiencies are illustrated using hit maps of selected XPC/RPC trigger planes for the 2012 data. The RPC hit maps display unambiguous hits, i.e. hits with exactly one x- and one y-readout signal per plane and event, if the hits are part of a Kalman track. As the XPCs are not used for the Kalman track reconstruction, here, all unambiguous hits are displayed. The detector areas connected to timing boards are marked by red frames, the edges of the timing boards are indicated by horizontal blue lines. Figure 4.16a shows the hit map of XPC 1 in SM 2. Several less efficient areas are visible, especially close to the edges of the 21 individual chambers which are arranged in three columns and seven rows. The diagonal pattern is due to broken readout channels. Either the corresponding diagonal signal strips are disconnected, the strands of the twisted-pair cables for the signal transmission severed, or the front-end electronics of the respective channels is broken. The RPC signal strips run horizontally and vertically. In Figure 4.16b several broken vertical strips are visible in the hit map of RPC 1, SM 1. In addition, the side of the RPC towards higher x-values exhibits less hits than the rest of the plane. On this side the RPC chambers are supplied with fresh gas. The gas flows horizontally through all three chambers of the same row towards the exhaust on the opposite side. The decreased number of hits in this area may be related to the
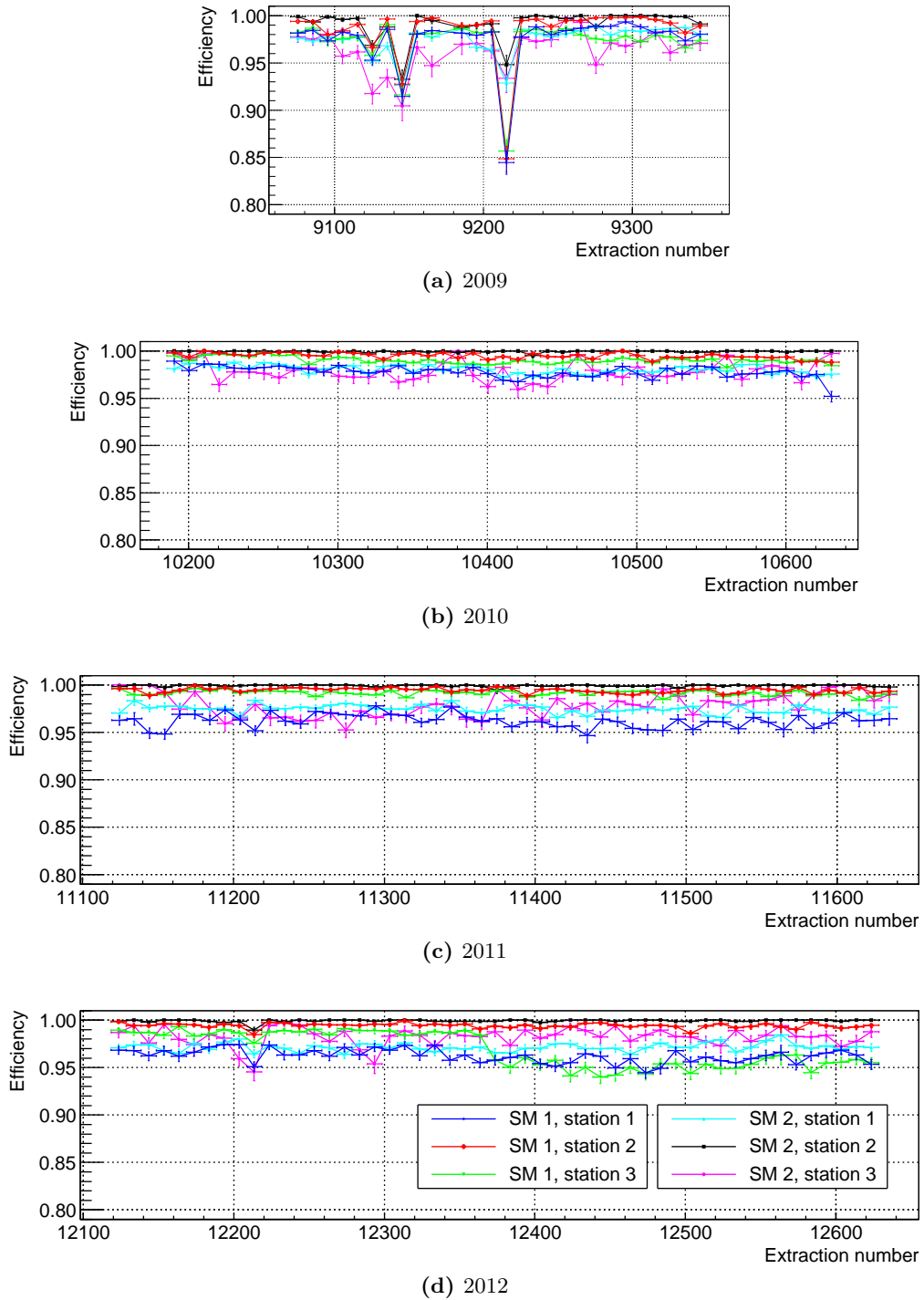
(a) 2009

(b) 2010

(c) 2011

(d) 2012

Figure 4.15: Trigger efficiency for each of the six trigger stations during the detector runs 2009–2012. The efficiencies are averaged over ten extractions which is equivalent to five days of detector operation. The error bars represent the statistical errors.

proximity to the gas inlets. However, this phenomenon remains unexplained but is present for most of the RPC planes. Figure 4.16c shows a row of RPC chambers in RPC 12, SM 1, that is completely disabled due to leakage currents in the high voltage system. Furthermore, half of the upper row in the same plane shows a reduced number of hits compared to the well-performing rest of the RPC plane. The size and location of the affected detector part suggests that the reason for this is a broken or disconnected twisted pair cable. Note that the hit maps add up all hits of the entire 2012 run. If a part of the detector failed during the run, the hit map still contains the hits before the failure. The effect of one further type of hardware failure is demonstrated in Figure 4.16d. It also depicts the hit map of RPC 12, SM 1, but here
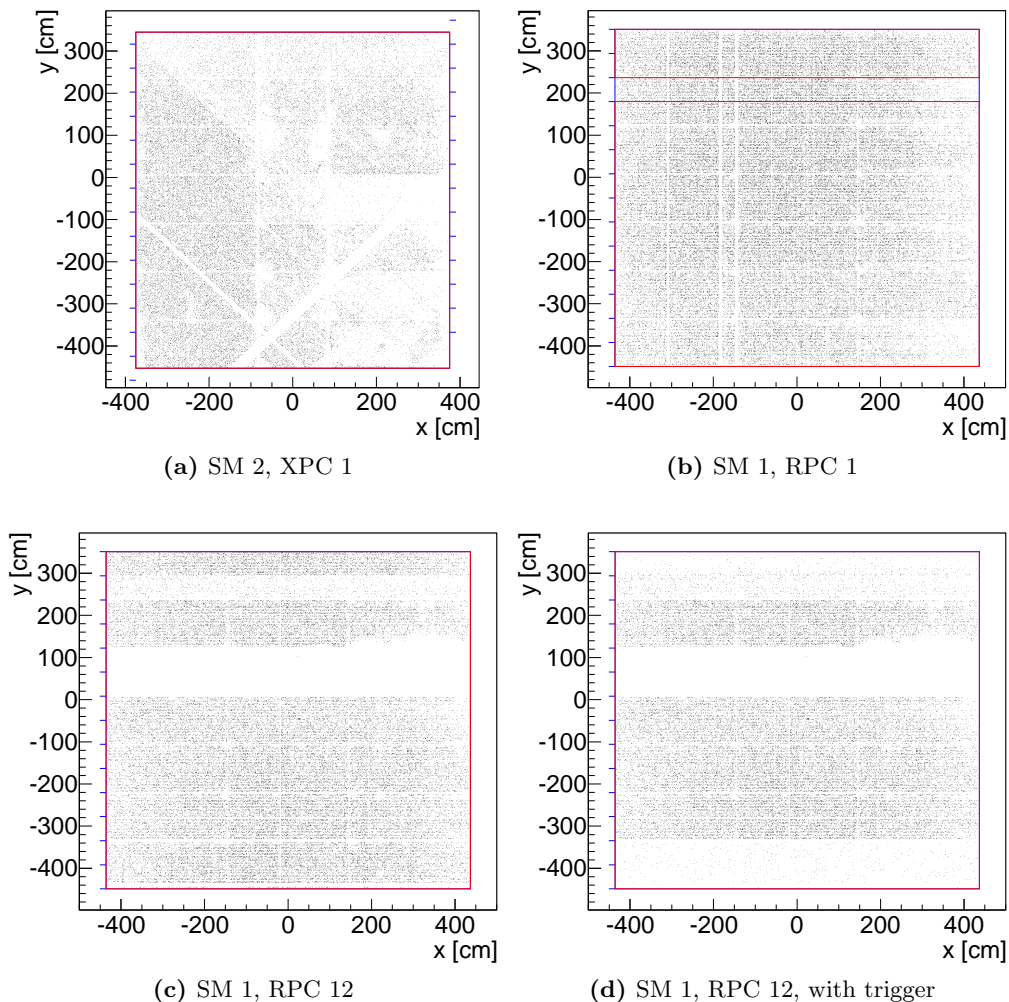

(a) SM 2, XPC 1

(b) SM 1, RPC 1

(c) SM 1, RPC 12

(d) SM 1, RPC 12, with trigger

Figure 4.16: Hit maps of selected XPC/RPC planes for the detector run 2012, illustrating different inefficient areas in the detector. The planes are viewed against beam direction. The detector areas connected to timing boards are marked by red frames.

the hits are only displayed if a trigger signal from the corresponding timing board is recorded. Accordingly, the comparison with Figure 4.16c reveals the loss of two timing boards on the bottom of the plane as well as the topmost one.

Chapter 5

Timing Calibration of the Trigger System

The spatial information on a particle's trajectory through the PT is derived from the time difference between the signal on the drift tube wire and the deliberately delayed trigger signal (see Chapter 4). Therefore, the timing resolution of the PT readout directly limits the spatial resolution of the drift tube detector. In order to achieve the desired momentum resolution of less than 25 % for all muon momenta up to 25 GeV, the error on the coordinate measurement must not exceed 600 μm, as elaborated in [Z$^+$05].

The error is composed of the uncertainty due to the mechanical misalignment of the drift tubes and the intrinsic error of the drift time measurement. The alignment error in turn consists of three parts: the error on the alignment of the individual wires inside the modules, the modules themselves and the drift tube walls. The wire misalignment was determined in [Len07] using a test setup with two modules from the PT mass production. The resulting value of 183 μm is slightly worse than the precision of 150 μm anticipated based on the module design. However, for the module and wall alignment statistical errors as low as 32 μm and 8 μm were achieved respectively [B$^+$14b]. Adding the alignment and drift time error in quadrature yields a maximum acceptable uncertainty on the drift time measurement of 570 μm in order to stay below a spatial resolution of 600 μm.

While the alignment error is constant, the effect of the four main uncertainties on the time measurement vary with the distance between track and signal wire:

- σ_{ion}, statistical distribution of the primary ionization clusters

- σ_{diff}, diffusion of the electrons by means of multiple scattering in the drift gas

- σ_{tube}, time resolution of the drift tube signal

- $\sigma_{trigger}$, time resolution of the trigger signal.

According to [Zim99] σ_{ion} is:

$$\sigma_{ion} = \sqrt{\frac{j^3}{4n_p^2(j^2 + 4n_p^2 r^2)}}. \tag{5.1}$$

r is the shortest distance between the particle track and the wire, n_p is the number of clusters per unit of length, and j is an index assigned to the clusters in ascending order according to their distance from the wire, cluster $j = 1$ being the closest. n_p depends on the mean atomic number $\overline{Z}$ of the gas and can be approximated by:

$$n_p = \overline{Z} \cdot 1.45\,\mathrm{cm}^{-1}. \tag{5.2}$$

For the PT gas mixture the value of $\overline{Z}$ is 18.8. Due to the stochastic distribution of the primary ionization clusters, the distance of cluster number j from the anode wire is not necessarily the shortest distance between track and wire. Furthermore, depending on the discriminator settings the accumulated charges of several clusters may be necessary to exceed the threshold. In the case of the OPERA drift tube specifications and settings (see Section 3.2.3) three clusters are needed on average to produce a signal [Jan08].

The error due to electron diffusion is given by:

$$\sigma_{diff} = \sqrt{\frac{2kTp\ln(r_c/r_a)}{eVp_0}} \cdot r, \tag{5.3}$$

k being the Boltzmann constant, T the temperature, p the pressure, r_c the cathode radius, r_a the anode radius, e the elementary charge and V the applied high voltage [Zim99]. T is set to $290\,\mathrm{K}$, the approximate average temperature at the detector, and $p = p_0$ since the tubes are operated at constant pressure.

The value for σ_{tube} contains the uncertainties on the timing of the signal from the drift tube to the TDC board. It was determined by a test pulse measurement (see Section 3.2.3): $\sigma_{tube} = 1.6\,\mathrm{ns}$. $\sigma_{trigger}$ comprises all errors on the trigger signal's timing, from the point of the signal production inside the RPC to the arrival of the stop signal at the TDC. A realistic estimate for the time resolution of the trigger signal $\sigma_{trigger}$ is a value in the order of $5\,\mathrm{ns}$. Since both σ_{tube} and $\sigma_{trigger}$ contain the uncertainty of the TDC measurement of $1.5\,\mathrm{ns}$ [MSC04], this value is once subtracted in quadrature. σ_{tube} and $\sigma_{trigger}$ are then converted from an error in time to a spatial error by means of the drift velocity. Due to the choice of the gas mixture for the PT, the drift velocity is

strongly dependent on the drift distance r. It is determined by using the time to distance relation which can be approximated by the following function [Won07]:

$$r(t) \approx 0.05798 \cdot t^{0.4791}. \tag{5.4}$$

Finally, the total intrinsic error of the drift time measurement is:

$$\sigma_{time} = \sqrt{\sigma_{ion}^2 + \sigma_{diff}^2 + \sigma_{tube}^2 + \sigma_{trigger}^2}. \tag{5.5}$$

σ_{time} and all four of its components are plotted in Figure 5.1. Since a drift tube wall has more than two hits for an average event and therefore provides at least two measurements, the errors are divided by $\sqrt{2}$. For all drift distances
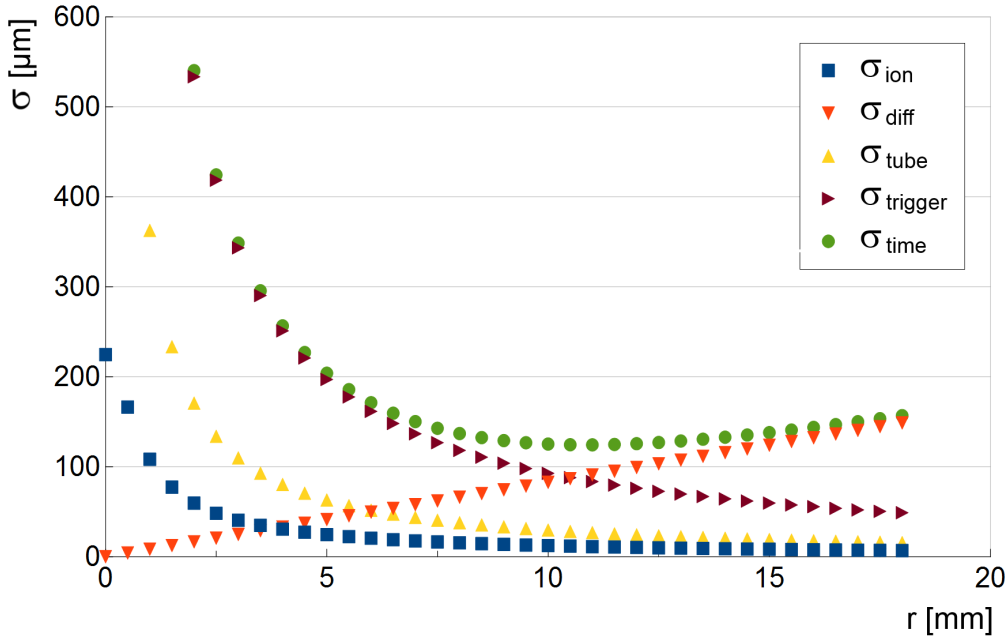
Figure 5.1: The intrinsic error of the drift time measurement σ_{time} and its four components: the error due to the primary ionization statistic σ_{ion}, the error due to electron diffusion σ_{diff}, the time resolution of the drift tube signal σ_{tube} and the time resolution of the trigger signal $\sigma_{trigger}$

of at least $2\,\text{mm}$ the PT's spatial resolution is within the designated limit. At shorter distances the uncertainties on the trigger signal timing become dominant. However, on average even events with very small drift circles achieve a sufficient track resolution due to the compensating effect of larger drift circles.

The timing calibration of the trigger system is not only essential to reach the desired momentum resolution but also for its use as a time of flight detector for atmospheric muons. A timing precision of a few nanoseconds for the trigger

signal is necessary to be able to distinguish between upgoing and downgoing particles which, at best, travel a few meters between different trigger planes. Without accurate signal delay corrections, the timing information is spoiled by various effects. For instance, depending on the point of interaction within an RPC plane, either close to or far away from the readout side, the propagation delay on the signal strip can deviate by up to 40 ns. The lengths of the twisted pair cables that are used to transfer the signals from the detector front-end to the trigger electronics differ by up to 10 m, yielding a difference in delay of about 50 ns. Even the way the cables are installed may cause deviations in the timing. A test on a 10 m twisted pair cable using LVDS signals and an oscilloscope showed that the propagation delay increases by about 5 % when the cable is coiled up as compared to a straightened cable.

There are three different signal paths the propagation delays of which have to be known in order to benefit from the timing measurements of the trigger signals on the TDC boards. The paths are named A, B and C, and the corresponding signal delays are t_A, t_B and t_C (see Figure 5.2). An overview of all time intervals defined in this chapter is given in Appendix B, Table B.2. For a detailed schematic of the trigger system, including the labels of the different cables (A′, A″, etc.), refer to Figure 4.4.

Path A starts at the end of the RPC/XPC readout strip and includes the interconnection board (see Section 4.1.1), the timing board, the twisted pair cable A′, the OPE, the twisted pair cable A″, and the PECL to TTL converter at the OTB input stage. Behind the converter the paths B and C branch off. Path B consists of the TTL to LVDS converter on the OTB and the twisted pair cable leading to the TDC board input stage. Path C includes the entire trigger signal path on the OTB master with the exception of the PECL to TTL converter, plus the short coaxial cable C′, the TTL line driver, the coaxial cable C″, the OVTB, the coaxial cable C‴, the OTB slave and the crate's backplane C⁗ which delivers the stop signal to the TDC board.

A selected dataset of 1696 extractions from the OPERA runs 2009–2012, corresponding to about 850 days of detector runtime, is used for all calibration steps, unless stated otherwise. The 2008 data is not used for the calibration because essential parts of the trigger system, namely the overall trigger (see Section 4.2.2) and the LVDS converters (see Section 4.2.4), were exchanged or added afterwards. Any data taking periods with known problems concerning hardware or software, with a special focus on the PT trigger system, are excluded from the dataset by omitting the entire extraction files which are affected. The numbers of all the extractions used for the calibrations and of the ones omitted are listed in Appendix C.

Figure 5.2: Simplified schematic of the trigger system illustrating the three signal paths to be calibrated, the corresponding time intervals t_A, t_B and t_C, as well as all further time intervals used for the calibration. Paths B and C branch off at the end of path A, behind the PECL to TTL converter at the OTB master input stage. All time intervals used in this chapter and their definitions are listed in Appendix B, Table B.2.

Since the propagation delay corrections for path C are needed for the calibration of path B, and these results in turn are needed to calibrate path A, the different calibration steps are presented in the order: path C (see Section 5.2), path B (see Section 5.4), path A (see Section 5.5). All resulting correction values shown in this chapter are relative corrections with respect to the first RPC plane of the corresponding SM. For the PT track reconstruction the absolute delay of the stop signal with respect to the time of the particle's passage through the drift tubes has to be known. The constant timing offset for the first RPC plane of each SM is determined using the track reconstruction software (see [Won07]) and is added in the software as a general offset to all relative correction values of the respective SM.

5.1 Principle of the Time of Flight Measurement

For each individual event and each SM, the trigger station which sends the stop signal that reaches the OVTB input first is the one providing the common

stop signal for the readout of all TDC boards of the same SM. Within this specific station, the trigger plane the signal of which is the first to reach the OTB input, provided a second signal follows within 75 ns to fulfill the majority condition, is the plane delivering the stop signal to the OVTB. This process is described in detail in Sections 4.1 and 4.2.2, and illustrated by the schematic timeline in Figure 5.3. It shows the two signals of a trigger station producing the common stop signal. It is assumed that both signals are induced by the same particle crossing the detector. Time is proceeding from left to right. The first point in time is the instant when the particle crosses an arbitrarily chosen reference plane parallel to the trigger planes (parallel to the x-y plane, see Figure 3.5). t_{tof} denotes the particle's time of flight from the reference plane to the individual trigger plane. t_{prop} is the propagation time of the RPC/XPC detector signal on the readout strip, from the point of the particle interaction to the end of the strip where the readout electronics is attached. t_A and t_C refer to the signal propagation delays on the corresponding signal paths (see Figure 5.2 and Table B.2). At the point in time marked "OVTB input" the signals from all three trigger stations of the same SM join at the OVTB input stage. In the example shown in Figure 5.3 the upper signal is the first one in its trigger station as well as the first one at the OVTB. Therefore, at the end of
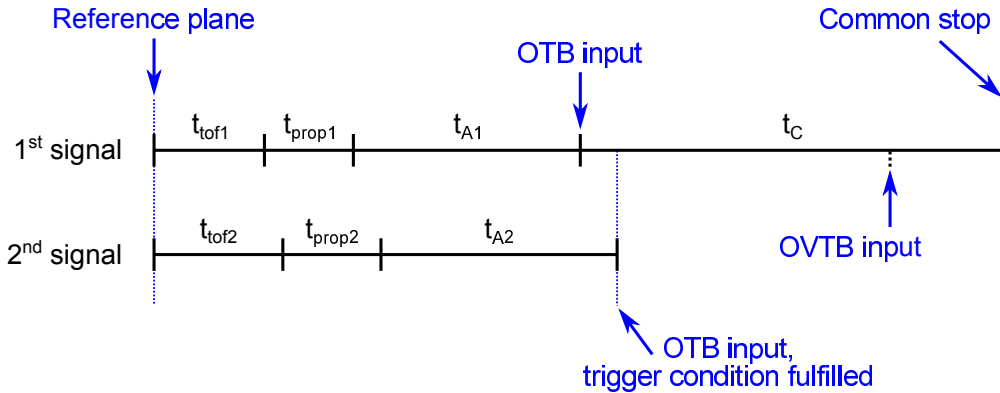
Figure 5.3: Schematic timeline for the production of the common stop signal. Time is proceeding from left to right. The different time intervals are not to scale for better readability. For an overview of the time intervals used in this chapter see Table B.2.

the time interval t_C the common stop signal is delivered to all TDC boards in the corresponding SM. Note that the different time intervals in the schematic figure are not to scale and were modified in length for better readability. For example, in reality t_C is about 100 times longer than the average propagation time t_{prop} on the RPC readout strips. The total time a trigger signal takes from the production of the detector signal inside the RPC plane to the delivery of the common stop at the TDC boards is of the order of 2 μs.

The time of flight measurement using signals of the PT trigger system bases on the fact that all incoming trigger signals are branched off to start a TDC, and that all TDCs within each SM are read out simultaneously upon the arrival of the distributed common stop signal. Figure 5.4 exemplarily shows the schematic timeline for any two signals coming from trigger planes in the same SM caused by the same particle crossing the detector. If for each signal the estimated propagation time on the RPC/XPC readout strip t_{prop}, the specific signal propagation delays t_A and t_B and the time t_{TDC}, measured by the corresponding TDC channel, are added up, the difference between these two sums corresponds to the particle's time of flight between the two trigger planes. In fact, the determination of the time and the direction of flight between planes belonging to different trigger stations using just the timing information is only possible since the introduction of the overall trigger and the consequentially shared time reference within each SM (see Section 4.2.2). In addition, due to the global readout of all TDC channels for each event, also singular signals from the two stations which do not contribute to the production of the corresponding stop signal and would not have generated a trigger signal in their own station can be used for a time of flight measurement. Especially these timing data from planes far apart increase the value of the timing information. The longer the flight distance between the points of measurement, the smaller is the relative error on the timing information and therefore also on the determination of the direction of flight.
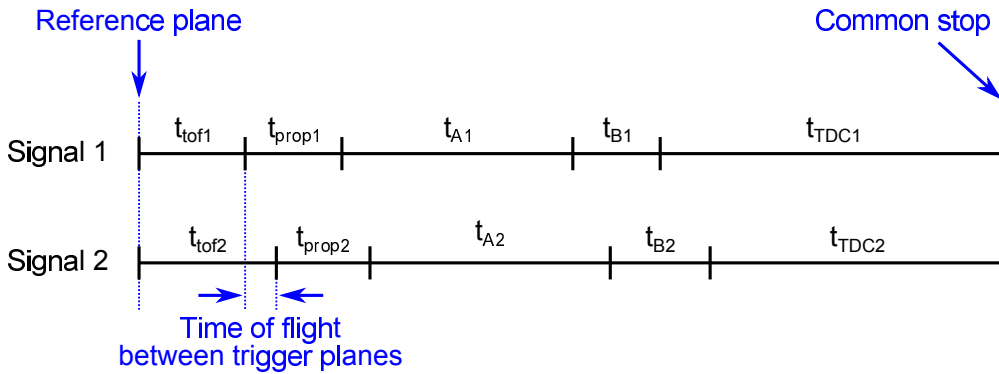
Figure 5.4: Principle of the time of flight measurement: schematic timeline for any two signals coming from trigger planes in the same SM caused by the same particle crossing the detector. The time of flight between the two corresponding trigger planes is the difference in the respective sums of t_{prop}, t_A, t_B and t_{TDC}. The different time intervals are not to scale.

5.2   Calibration of the Stop Signal Path

The first propagation delay to be determined is the one of the stop signal path C (see Figure 5.2). The main contribution to the total delay on path C and to the differences in delay between the trigger stations comes from the OTB masters. It can directly be measured for each trigger station individually using the built-in test pulse function, without the need for actual trigger signals or the knowledge of their chronological order. This calibration step is covered in Section 5.2.1. The minor differences in the propagation delays behind the OTB masters were also measured and are presented in Section 5.2.2.

5.2.1   Signal Propagation Delay on the Trigger Boards

The OTB test pulses are sent by the on-board microcontroller to the first CPLD. At the same time a signal goes to the built-in TDC chip to start the measurement. The test pulses take the same path as trigger signals coming from the OTB inputs with the exception of the PECL to TTL converter, the input pulse width controller and the mask stage (see Section 4.1.2). Since these components have only minor and fixed propagation delays of the order of 10 ns, they do not make a significant contribution to the differences in the propagation delays of different trigger stations and can be omitted for the calibration. All adjustable devices are passed by the test pulses before they reach the TDC chip to stop the measurement (see Figure 4.8). The on-board TDC is of the type MSC TDC501 with a time resolution of 220 ps [MSC10]. However, the measured values are handled within the PT slow control system with nanosecond accuracy.

The slow control software is set up to automatically initiate timing measurements on all six OTBs about every eleven minutes, synchronously sending test pulses to all five channels of each board. During these test pulse measurements the OTBs' input stages remain open so that trigger signals from the detector reaching the first CPLD before the test pulses can distort the measurement results, yielding smaller delay values than expected. This is the case for any signal arriving at the majority logic within 75 ns before the test pulses, as well as for two or more trigger signals, which themselves fulfill the majority condition and produce a stop signal at any given time after the TDC has been started and before it has been stopped by the test pulses. At first, these low values for the OTBs' propagation delays, occurring statistically about once every other day, have been misinterpreted as a spontaneous loss of the stored settings of the programmable delay lines, which could happen during a local power cut. As a measure against this presumed failure the slow control software was programmed to reset all delay lines to their designated

values whenever any of the six timing measurements on the OTBs gave a result of less than 1600 ns. Directly after a reset another measurement was done, and if the resulting value was still low this process was repeated until a maximum of six measurements/resets was reached. On 30 August 2010 this procedure was slightly revised: after the first measurement of a value below 1600 ns[1] the delay lines are not reset. Instead, a second measurement is performed right away. Should the result still be below the threshold, resets plus further measurements are initiated as before. Also since that date, all measurement values are stored in the slow control database, together with a counter that indicates if and, if so, how many times a measurement had to be repeated. On only five occasions between September 2010 and the end of the 2012 run more than one repetition was needed. In all of these cases a power cut in parts of the detector was the reason for the faulty or missing measurement results so that the delay line settings can be considered completely stable. It should be noted that each test pulse measurement produces an actual stop signal also causing a readout of all PT TDCs. However, the very low rate of these stop signals of less than 2 mHz can be neglected in terms of detector dead time.

To determine the propagation delay for each OTB, 5170 on-board measurements from 10 August until 18 September 2012 were averaged. The values and their corresponding statistical errors are listed in Table 5.1. This period was chosen for being one of very stable detector operation and of relatively

Table 5.1: Signal propagation delays on the OTB masters averaged over about 5000 consecutive measurements. The uncertainties assigned to the delay values are the corresponding statistical errors.

SM	Trigger Station	Propagation Delay [ns]
1	1	1643.0 ± 1.0
1	2	1638.5 ± 0.6
1	3	1646.3 ± 0.8
2	1	1638.0 ± 1.2
2	2	1624.8 ± 0.6
2	3	1648.5 ± 0.7

constant ambient temperature in hall C. The average temperature during the measurements is later used to try to correct the boards' propagation delays for a possible temperature dependence with the aim to improve the calibration (see Section 6.2).

---

[1] On 13 September 2010 the threshold was raised to 1622 ns.

Over 100 temperature sensors of type KTY81-110 (Philips Semiconductors) are distributed over the detector, connected to PT preamplifier boards and read out through the OSUBs once every minute [Göl12]. In addition to the individual measurements, the readout values of all sensors are averaged and saved in the slow control database as `hallC_temp` once per hour, providing a measure for changes in the ambient temperature of the experimental hall. The temperature during the 2012 run is shown in Figure 5.5, the highlighted area corresponds to the period chosen for the OTB delay measurements listed in Table 5.1. During this period of time the temperature in hall C, averaged over 936 values of `hallC_temp`, was $(18.6 \pm 0.1 \text{ (stat.)})\,^\circ\text{C}$.
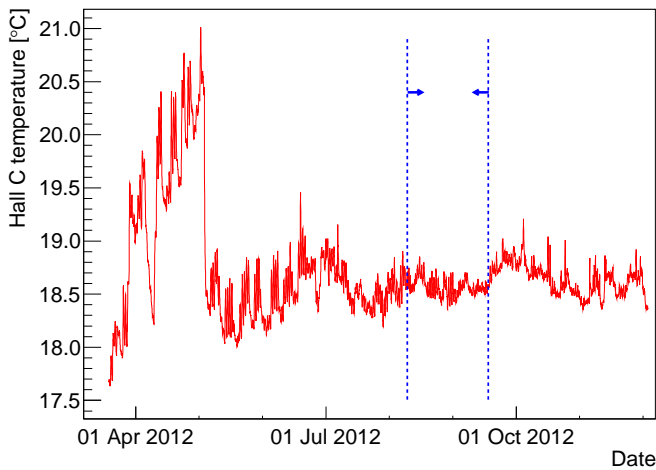
Figure 5.5: Ambient temperature of hall C in the LNGS during the 2012 run. Once per hour the readout values of all PT temperature sensors are averaged. The highlighted area is the period chosen for the OTB delay measurements (10 Aug. – 18 Sept.).

5.2.2   Signal Propagation Delay of the Stop Signal Distribution

For all six PT trigger stations the cables used to transfer the stop signals from the OTB master outputs to the OTB slave inputs are of the same type and length. The electronics components along this signal path also have the same specifications for all stations, and the only programmable delay lines are on the OVTBs, applying likewise to all channels of the same SM. Nevertheless, the total length of the stop signal distribution path behind the OTB masters is more than 30 m, including two 15 m coaxial cables (C'' and C''' in Figure 4.4). This way, even small variations in the propagation delay per meter cable may add up to a sizable difference between the trigger stations and should therefore be known and, if necessary, considered.

The propagation delays were measured with an oscilloscope, averaging more than 200 measurements for each trigger station. The OTB masters have two TTL output connectors, one of which is not used. The measurements were taken between this connector and the TTL input connector of the OTB slave.

Both OTB sections are integrated in the same printed circuit board so that the two connectors are only a few centimeters apart and easy to access with very short cables. The measurement results are listed in Table 5.2. The differences between the trigger stations are only of the order of 1 ns but are included in the calibration nonetheless.

Table 5.2: Signal propagation delays on the cables and electronics between the OTB master outputs and the corresponding OTB slave inputs. The delays were measured using an oscilloscope, averaging more than 200 measurements for each trigger station. The uncertainties assigned to the delay values are the corresponding statistical errors.

SM	Trigger Station	Propagation Delay [ns]
1	1	222.7 ± 0.1
1	2	223.3 ± 0.1
1	3	223.4 ± 0.1
2	1	222.6 ± 0.4
2	2	223.7 ± 0.3
2	3	223.4 ± 0.3

The signal propagation delays on the OTB slaves (see Figure 4.9), all twelve of which are built identically and do not contain any adjustable components, are considered equal. The maximum timing difference for the stop signal on the crate backplane was measured between the slots labeled TDC 0 and TDC 4 (see Figure 4.5). Since the result was below 1 ns, the difference in delay between the neighboring slots TDC 7 and TDC 8, where all TDCs that record trigger signals are located, can be neglected.

5.3 Determination of the Trigger Signal Generating Station

For the following calibration steps it is essential to know which trigger station delivers the stop signal that is then distributed by the OVTB to all TDCs of the same SM. The TTL to LVDS converters described in Section 4.2.4 and the 1 m coaxial cables labeled D in Figure 4.4 have been installed in order to directly provide this information. The principle of the determination of the trigger signal generating station is illustrated in Figure 5.6. The signals coming from the OTB masters of the different trigger stations via signal paths C (denoted by t_{C1} and t_{C2}) are branched off towards a TDC board, right before they enter the OVTB. The signal arriving first at this point is the one that stops all TDC measurements in the respective SM, since the OVTB builds
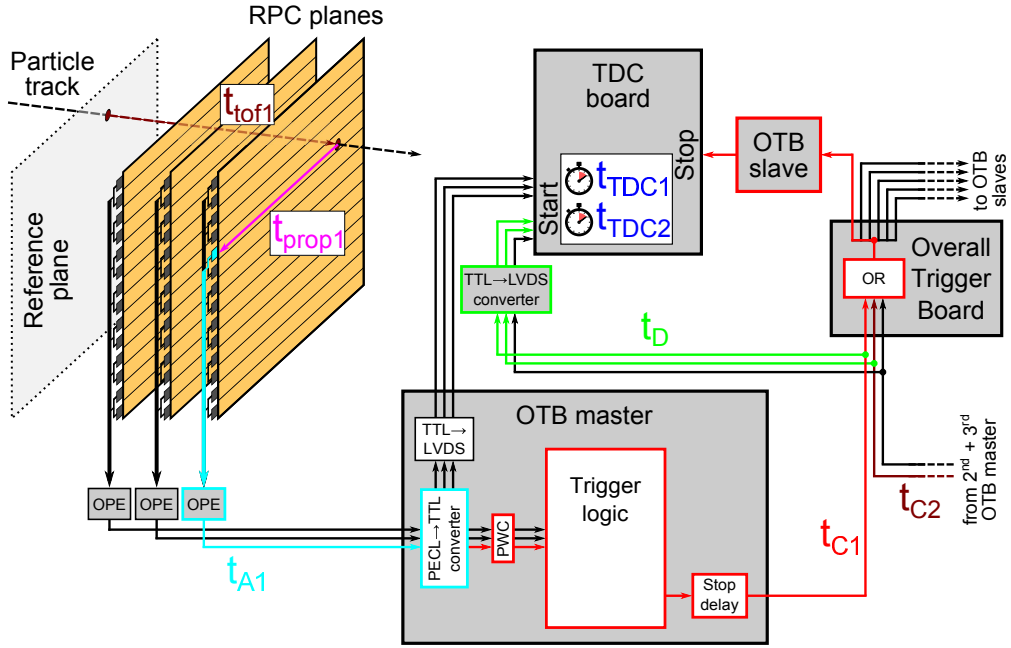
Figure 5.6: Simplified schematic illustrating signal path D and the corresponding time interval t_D. Path D branches off right before the OVTB input. For an overview of the time intervals used in this chapter see Table B.2.

the logic OR of all incoming signals and in this way distributes the first one as the common stop signal (see Section 4.2.2). As the differences in propagation delay t_D on the short coaxial cables D and the TTL to LVDS converters are negligible, the order in which the signals are branched off is preserved when they arrive at the TDC board. In Figure 5.7 the signals from two trigger stations of the same SM are shown in a schematic timeline: the one above is the first signal, providing the common stop. The signal below arrives at the OVTB input later than the first one and is therefore without effect. For this second trigger station the TDC measurement (signal path D) is started later than the one for the first station. Consequently, the measured time t_{TDC2} is shorter than t_{TDC1}, so that the order in which the signals from the different trigger stations arrive at the OVTB can be deduced from the length of the measured times t_{TDC}. Since the propagation delays on path D and on the second part of path C (from the OVTB onwards) deviate very little from each other for the different stations (see Section 5.2.2), the measured value t_{TDC1} for the trigger generating station is almost constant, no matter which station produces the first signal. To securely identify the first trigger signal using just the timing information t_{TDC}, the spread of the time interval t_{TDC1} measured via signal path D has to be determined and an adequate cut has to be defined.
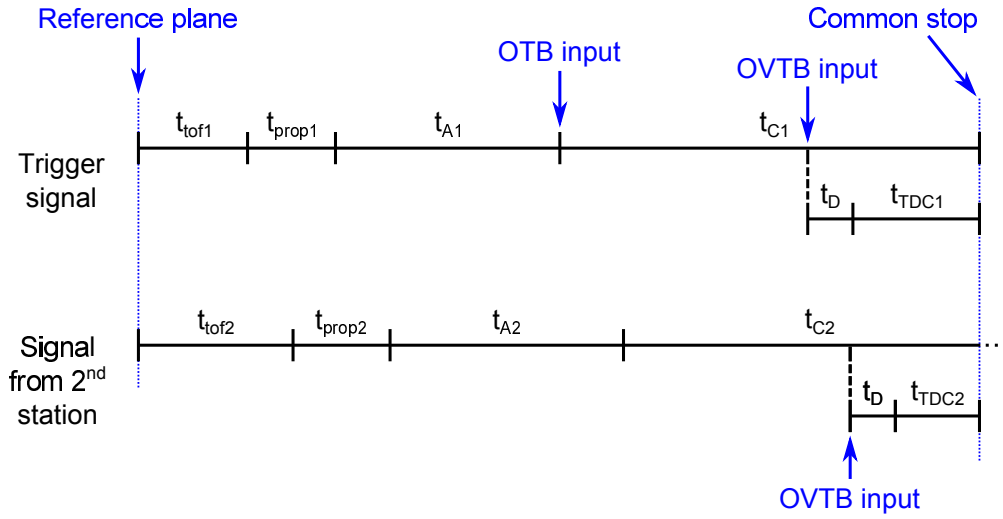
Figure 5.7: Schematic timeline for the determination of the trigger signal generating station via cables D and the TTL to LVDS converters. In this example two trigger stations generated a signal. For each station only the first signal is shown. The principle for the production of a trigger signal within one station is shown in Figure 5.3. The different time intervals are not to scale.

From the dataset described at the beginning of this chapter and in Appendix C, all events with no more than one signal at the OVTB input (respectively the LVDS converters) per SM are selected. These signals are evidently the first ones in their respective SM. The times t_{TDC} measured via the LVDS converters are stored in a histogram. Since these times are identical for both SMs, all measured values are accumulated in just one histogram, as shown in Figure 5.8. More than 99.5 % of all values lie within 4 ns, populating the bins from 145 ns to 148 ns.[2] To unambiguously determine the first signal, it is required that the longest measured time be inside this range and that the time measured for the second signal be more than 4 ns apart. For any of the calibration steps where knowledge of the first trigger signal is needed, all events not passing this cut are discarded.

---

[2] Note that these values are the ones directly measured by the TDCs, whereas the values handled within the OPERA software are converted according to Equation 4.1, so that here the corresponding range is from 1855 ns to 1852 ns.
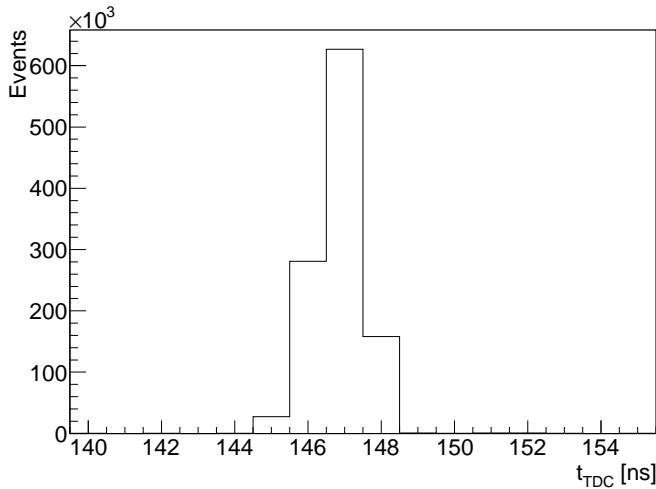
Figure 5.8: Time interval t_{TDC} of all first trigger signals transmitted over signal paths D and measured by the TDCs to which the TTL to LVDS converters are connected. The full dataset described in Appendix C is used and a maximum of one OVTB input signal per SM is required.

5.4 Calibration of the Path from Trigger Board to TDC Board

A rough estimate for the propagation delay t_B on the signal path from the trigger board input to the TDC board input (see Figure 5.2) can be obtained from the lengths of the respective cables and their specified propagation delay per meter. For all connections between the OTBs and the TDC boards, the cable type "3M Twisted Pair Flat Cable, 2100 Series" with a propagation delay of 5.7 ns/m [3M10] is used. The first and the second trigger station of SM 1 as well as the first station of SM 2 have 1 m cables. The remaining three stations are equipped with 10 m cables, so that between the stations with short cables and the ones with long cables a difference in the delay on path B of about 50 ns is to be expected.

To calibrate signal path B, only the trigger plane which produced the trigger signal has to be known. In fact, the trigger signal does not even have to come from a particle interaction within the detector but may also be caused by two random noise signals which coincide by chance within 75 ns and fulfill the trigger condition. The first signal, being the one to produce the common stop, is split up at the OTB input stage and transmitted via signal path B as well as via path C, as illustrated in the schematic timeline in Figure 5.9. Since the delay on path C is known (see Section 5.2), the delay on path B can directly be determined from the time measured by the TDC:

$$t_B = t_C - t_{TDC}. \tag{5.6}$$

In order to identify the triggering station for each SM, the information gained through the LVDS converters can be utilized as described in Section 5.3. For the determination of the first signal within the triggering station, the yet
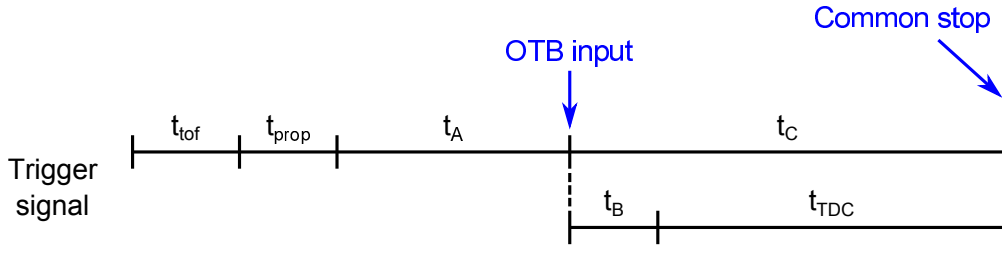
Figure 5.9: Schematic timeline for the calibration of the signal path for a trigger signal from the OTB input stage to the TDC board. The different time intervals are not to scale. For an overview of the time intervals used in this chapter see Table B.2.

uncalibrated signal path B is used. Due to possible but at this point unknown differences between the propagation delays for the two or three signals on path B, the times t_{TDC} can lead to a wrong assignment for the first signal. Therefore, a strong cut on the measured time difference between first and second signal is applied. The signals are transmitted over different pairs of conductors on the same flat cable, so the expected differences in delay are only about 2 ns for a 10 m cable. As a precaution against any unknown effects not accounted for, the first signal is required to arrive more than 10 ns before the second one. To reduce the risk of selecting events where the stop signal is produced by noise on or behind the OTB, it is also required that the signals from two trigger planes in the triggering station arrive at the TDC board within 65 ns, also taking a 10 ns buffer into account as compared to the trigger condition. Signals from the two readout sides of the same XPC (corridor and rock side) are treated as their logic OR, as implemented in the hardware of the corresponding OTBs (see Section 4.1.2). If also a signal from the third trigger plane falls into the 65 ns time frame, the event is discarded.

Three further selection criteria have been tested. Firstly, only events were taken, where the width of all signals transmitted via path B was above 81.25 ns. Since the trigger signals are recorded by the same TDC boards as the drift tube signals, their signal widths are also measured and stored using the same categories. Secondly, only events with a reconstructed 3D track[3] were selected. And thirdly, all events with more than one triggering station per SM were discarded. None of these three criteria had a positive effect on the quality of the calibration, and they were therefore abandoned to avoid the mere reduction of statistics which they caused.

---

[3] A 3D track results from merged Kalman tracks in the xz- and the yz-plane.

In summary, the following cuts are applied for the selection of events:

- The time measured via path D (LVDS converters) for the first signal at the OVTB input has to be within the expected range (145 ns to 148 ns).

- A possible second signal at the OVTB input of the same SM has to arrive more than 4 ns after the first one.

- The first signal from a trigger plane has to arrive at the TDC (via path B) more than 10 ns before the second one.

- Two signals in the triggering station have to arrive within 65 ns. If two signals come from the same XPC (corridor and rock side readout), they are treated as their logic OR, as implemented in the hardware of the corresponding OTBs.

- If also a signal from the third trigger plane falls into the 65 ns time frame, the event is discarded.

Figure 5.10 exemplarily shows the result for the determination of t_{TDC} for the first RPC trigger plane in SM 1. The distributions for all other trigger planes are similar in width and shape. On the x-axis the histogram does not display the measured time t_{TDC} directly, but instead the actual TDC output in terms of bits. The TDCs have a maximum measurement range of 3.2 μs, and the measured time is stored in a 12 bit register. Accordingly, the least significant bit corresponds to a measured time of 0.78125 ns. This type of presentation was favored over another binning, e. g. in nanoseconds, in order to avoid a distortion of the already digitized data through binning effects. To obtain the measurement value in nanoseconds, a Gaussian is fitted to the peak, and the resulting mean is multiplied by 0.78125 ns. The results are listed in Table 5.3 in the column labeled t_{TDC}. Although each XPC functions as one trigger plane, the two-sided readout entails the use of two separate signal paths which have to be calibrated individually. Therefore, the number of so-called trigger channels per SM is eleven, numbered in the order: XPC 1 rock side, XPC 1 corridor side, XPC 2 rock side, XPC 2 corridor side, followed by the seven RPC planes enumerated in beam direction.

The high value of χ^2 per number of degrees of freedom for the Gaussian fit in Figure 5.10 states that the data is not accurately described by a normal distribution. In fact several known phenomena suggest the presence of electronic noise that could explain an asymmetrical distribution. For example, the same calibration plot for trigger channel 8 in SM 2 shows a peak with a clear tail towards shorter measurement times t_{TDC} for the 2011 data (see Figure 5.11a). In 2012 the peak remains at the same value but the background causing the tail
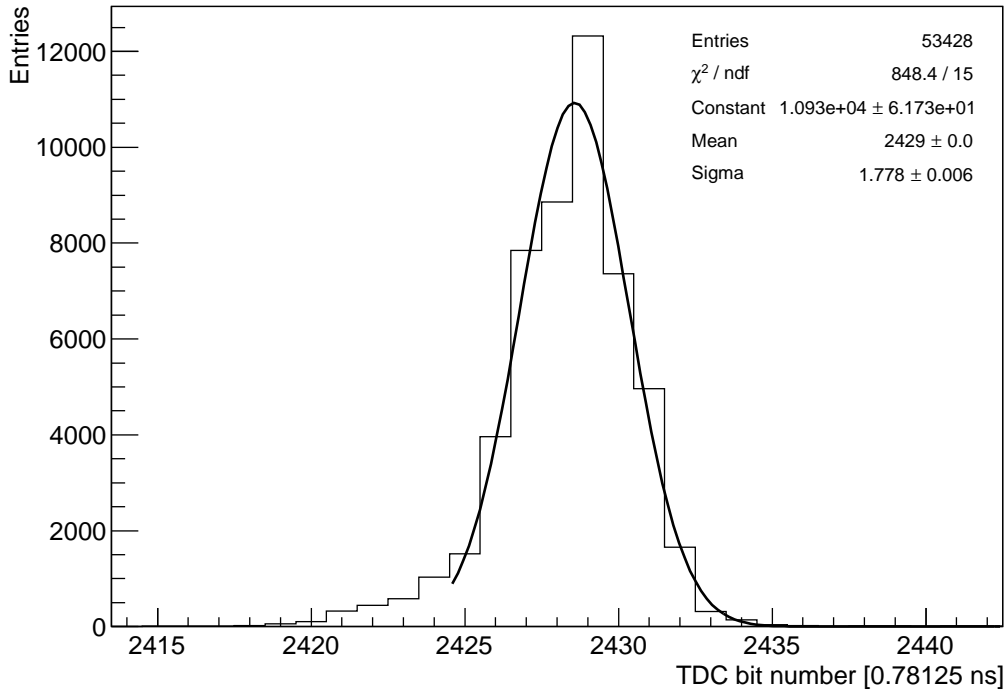
Figure 5.10: TDC output for the calibration of signal path B for the first RPC trigger plane in SM 1. The x-axis shows the actual TDC output in terms of bits. The least significant bit corresponds to a measured time of 0.78125 ns. The event selection criteria and the choice of the fit function are explained in the text.

is vanished (see Figure 5.11b). The reason for this abrupt change is unknown but a feasible explanation is the deactivation of an external source of noise after the 2011 run. One such source are certain fluorescent lamps installed on the platform on top of the detector. During the commissioning phase it was noticed that a few of these lamps induce high noise rates in the electronics, in some cases even causing crashes of the DAQ system due to excessive event rates. Another possible source of signal disturbance was discovered after the installation of the OVTB and the crossover trigger (see Section 4.2.3). Between the ground levels of the two crates, which are each housing the OVTB for one SM, a potential difference of up to ±300 mV was measured. If, for instance, the ground level of the OTB was pulled up by 300 mV by an external load connected to the same ground, the switching times of components processing TTL signals would decrease. Since TTL uses single-ended signaling with a fixed logical high level voltage of 2 V and all signals have finite rise times, the raising of the ground level reduces the time until a high level is reached. As a consequence, the OTB's signal propagation delay would decrease, resulting in a faster delivery of the stop signal and in shorter measurement times on the TDCs. Nevertheless, the actual reason for the given shape of the distribution

(a) 2011 data   **(b)** 2012 data
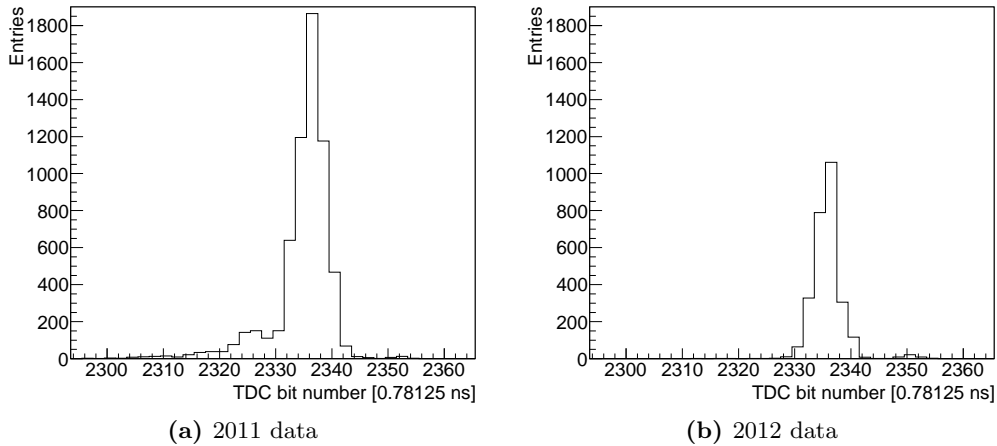
Figure 5.11: TDC output for the calibration of signal path B for trigger channel 8 in SM 2. The tail towards shorter measurement times visible in the 2011 data is vanished in the 2012 dataset. A possible explanation for this abrupt change is the deactivation of an external source of noise after the 2011 run.

remains unknown. Since within the TDCs' time resolution the mean value of the Gaussian fit leads to the same result as the arithmetic mean or even the value of the highest bin, the fit was chosen for the determination of t_{TDC}.

For all relative corrections of the propagation delays on the different signal paths, the first RPC trigger plane of each SM (trigger channel 5) is taken as reference and therefore always has a correction value of 0.0 ns. To obtain the relative corrections for t_C, the corresponding values in Tables 5.1 and 5.2 are added, after which the resulting delay for the first trigger station is subtracted from the values of all three stations of the same SM. Since the five or three channels of each trigger station share the same signal path C, their relative corrections for t_C are naturally the same (see Table 5.3). To get the relative corrections for t_B, Equation 5.6 is used and, again, the results are expressed with respect to trigger channel 5 of the same SM, the value of which is set to zero. Positive values correspond to longer propagation times on the respective signal path.

As anticipated, the correction values for t_B for the three trigger stations with 10 m long cables B are about 50 ns. Also the variations in delay between stations using cables of the same length are in the expected range. This could be due to slight differences in actual cable length or possible variations in the ground level of the electronics crates housing the respective OTB and/or TDC board, resulting in slower or faster signal processing in the electronics components. However, the differences in t_B of several nanoseconds between the XPC channels 1–4 and the RPC channel 5, all within the same trigger station, cannot

Table 5.3: Correction values for the signal propagation delays on signal paths C and B. t_B is derived from the measured value t_{TDC} by using Equation 5.6. The first four trigger channel numbers refer to the two XPCs, each with two readout sides/cables, in the order: XPC 1 rock side, XPC 1 corridor side, XPC 2 rock side, XPC 2 corridor side. Trigger channel numbers 5 through 11 refer to the RPC planes in beam direction. The correction values are expressed with respect to the first RPC plane (trigger channel 5) of the same SM, the value of which is set to zero.

SM	Trigger Channel	t_{TDC} [ns]	Rel. Correction for t_C [ns]	Rel. Correction for t_B [ns]
1	1	1893.4 ± 0.01	0.0	3.8 ± 0.01
1	2	1896.0 ± 0.02	0.0	1.2 ± 0.02
1	3	1891.1 ± 0.01	0.0	6.2 ± 0.01
1	4	1892.6 ± 0.03	0.0	4.6 ± 0.03
1	5	1897.3 ± 0.01	0.0	0.0
1	6	1890.6 ± 0.02	-3.9 ± 1.2	2.8 ± 1.20
1	7	1889.1 ± 0.01	-3.9 ± 1.2	4.3 ± 1.20
1	8	1889.6 ± 0.02	-3.9 ± 1.2	3.8 ± 1.20
1	9	1848.9 ± 0.03	4.1 ± 1.3	52.4 ± 1.30
1	10	1847.8 ± 0.02	4.1 ± 1.3	53.6 ± 1.30
1	11	1847.9 ± 0.02	4.1 ± 1.3	53.4 ± 1.30
2	1	1887.6 ± 0.02	0.0	4.8 ± 0.02
2	2	1890.1 ± 0.04	0.0	2.3 ± 0.04
2	3	1890.8 ± 0.01	0.0	1.5 ± 0.01
2	4	1889.3 ± 0.05	0.0	3.1 ± 0.05
2	5	1892.4 ± 0.01	0.0	0.0
2	6	1828.7 ± 0.05	-12.1 ± 1.7	51.6 ± 1.70
2	7	1825.5 ± 0.04	-12.1 ± 1.7	54.8 ± 1.70
2	8	1824.9 ± 0.02	-12.1 ± 1.7	55.3 ± 1.70
2	9	1850.9 ± 0.02	11.3 ± 1.8	52.8 ± 1.80
2	10	1849.7 ± 0.03	11.3 ± 1.8	54.0 ± 1.80
2	11	1850.6 ± 0.02	11.3 ± 1.8	53.1 ± 1.80

be explained by these effects, since they all share the same cables and crates. The tolerance in conductor lengths within the same 1 m twisted pair cable can only account for a deviation in delay far below the TDCs' time resolution. To exclude or find a possible difference between the XPC and RPC input channels on the OTB, e.g. due to the additional logic OR gate for the two pairs of XPC channels, test measurements on a spare board, programmed for the use with one RPC and four XPC signals (see Section 4.1.2), were performed. A pulse

generator and a TTL to PECL converter were used to produce an input signal, and an oscilloscope to measure the board's propagation delay. No difference whatsoever was found between the propagation delays of the five input channels.

Another explanation for the longer delays measured for the XPC trigger signals may be potentially longer rise times. As opposed to the RPCs, made of Bakelite and installed inside the magnet arms, the glass XPCs are slightly different in setup: they are installed outside the magnets, with a greater distance to dense materials, and their timing boards are connected with longer cables to their own set of OPE boards. Different ground levels on the timing board or OPE side, or higher capacitance or inductance of components along the signal path could increase the rise times of the XPC signals, leading to a later start of the corresponding TDC measurements and consequently to greater correction values for t_B. Since the deviations in the XPC signal delays were only noticed after the final detector shutdown, the actual signal shapes could not be verified. Nevertheless, the evaluation of data from four years of data-taking gave stable results for the timing measurements. Therefore, the correction values for all channels are used in the following calibration steps.

5.5   Calibration of the Path from Timing Board to Trigger Board

For an approximation of the differences in signal delay t_A on the signal path from the timing boards, via the OPE boards and towards the OTB inputs, the length and type of the installed cables is listed in Table 5.4. The cables A′ (see Figure 4.4) and the OPE boards were installed by the working groups that constructed the XPC/RPC detectors before the drift tube detector and the rest of the trigger system were assembled by the PT group from Hamburg. Since the cables partially run inside the detector, they are not accessible anymore and their length cannot be verified. The values in Table 5.4 are taken from [S+08]. The cables A″ were inspected visually. In some cases their lengths deviate considerably from the designated length of 15 m. In addition, two further types of twisted pair flat cable were installed, other than the 3M 2100 Series, which is used for the drift tube readout and for the cables B (see Section 5.4). The "Amphenol Spectra-Strip Twist 'N' Flat" cable has a propagation delay of 5.2 ns/m [Spe14]. The supplier of the third type of cable could not be identified. Its propagation delay was measured to be 5.4 ns/m, using an oscilloscope and LVDS signals on a 10 m spare cable of said type. Summarizing, differences in delay of up to about 30 ns should be expected.

Table 5.4: Cable lengths and types for signal path A. The lengths of the cables A′ are taken from [S⁺08]. The propagation delays on the different cable types are 5.7 ns/m for the 3M 2100 Series [3M10], 5.2 ns/m for the Spectra-Strip [Spe14], and 5.4 ns/m for the unknown type (measured).

SM	Trigger Channel	Length A′ [m]	Length A″ [m]	Cable Type A″
1	1	18.0	5.0	unknown type
1	2	18.0	10.0	Spectra-Strip
1	3	18.0	5.0	unknown type
1	4	18.0	10.0	Spectra-Strip
1	5	16.0	10.5	3M 2100 Series
1	6	16.0	10.0	3M 2100 Series
1	7	16.0	10.0	3M 2100 Series
1	8	16.0	10.0	3M 2100 Series
1	9	16.0	10.0	3M 2100 Series
1	10	16.0	10.0	3M 2100 Series
1	11	16.0	10.0	unknown type
2	1	18.0	15.0	3M 2100 Series
2	2	18.0	15.0	3M 2100 Series
2	3	18.0	15.0	3M 2100 Series
2	4	18.0	15.0	3M 2100 Series
2	5	16.0	15.0	3M 2100 Series
2	6	16.0	15.0	3M 2100 Series
2	7	16.0	15.0	3M 2100 Series
2	8	16.0	15.0	3M 2100 Series
2	9	16.0	10.0	3M 2100 Series
2	10	16.0	10.0	3M 2100 Series
2	11	16.0	10.0	3M 2100 Series

To calibrate signal path A, XPC and RPC signals belonging to a well known particle track in the detector have to be selected. For one thing, the particle's trajectory has to be known to determine the time of flight between the two trigger planes, the signal delays t_A of which are to be compared. And for another thing, the x-coordinates of the track's intersection points with the planes have to be known to calculate the propagation times on the readout strips. Figure 5.12 shows a schematic timeline for two trigger signals produced by the same particle crossing the detector. The particle's time of flight towards the trigger planes is given with respect to an arbitrarily chosen, but common reference
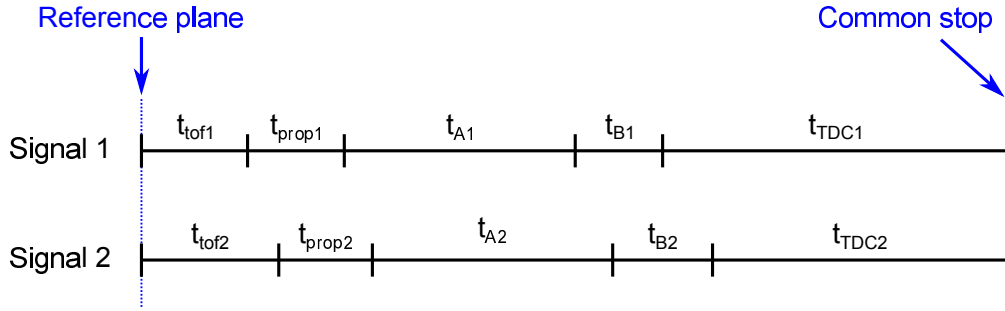
Figure 5.12: Schematic timeline illustrating the calibration of signal path A. The two signals are produced by the same particle, successively crossing two trigger planes of the same SM. The difference in the respective sums of t_{tof}, t_{prop}, t_B and t_{TDC} yield the difference in propagation delay t_A on path A. The different time intervals are not to scale. For an overview of the time intervals used in this chapter see Table B.2.

plane. Because also the instant of the stop signal is common to both timelines, the two sums of time of flight, the propagation delays on the signal strip as well as on the cables A and B, and the time measured by the TDC are equal:

$$t_{tof1} + t_{prop1} + t_{A1} + t_{B1} + t_{TDC1} = t_{tof2} + t_{prop2} + t_{A2} + t_{B2} + t_{TDC2}. \quad (5.7)$$

The time interval t_{TDC} is measured for each signal coming from a trigger plane, t_B is known from the previous calibration step and, providing t_{tof} and t_{prop} can be determined from the reconstructed track, the difference Δt_A in propagation delay on the two cables A can be obtained using:

$$\Delta t_{A12} \equiv t_{A1} - t_{A2}$$
$$= t_{tof2} + t_{prop2} + t_{B2} + t_{TDC2} - t_{tof1} - t_{prop1} - t_{B1} - t_{TDC1}. \quad (5.8)$$

To get a simple yet sufficiently precise estimate of the particles' flight path, long and straight muon tracks are selected by applying several cuts. Only events with exactly one reconstructed 3D Kalman track are taken to avoid ambiguities when assigning trigger signals to the particle track which generated them. A minimum of 70 digits is required. A digit in the electronic detectors is a point in one projection plane, the xz- or the yz-plane. A track with 70 digits has a minimum length of about 5 m in the detector. Ignoring possible scattering of the particle or its deflection in the spectrometers' magnetic fields, a linear regression with all Kalman track digits is done for each projection

plane.[4] This approximation is justified a posteriori by cutting on the RMS[5] of the residuals, constraining the RMS to values below $3\,\text{cm}$ both for the xz- and the yz-projection. In addition, tracks with a maximum residual of $5\,\text{cm}$ or more in any projection are excluded. The distance d traveled by the particle between the two trigger planes in question is then determined by the intersection points (x_1, y_1, z_1) and (x_2, y_2, z_2) of the fitted straight line with the planes:

$$d = \sqrt{(x_1 - x_2)^2 + (y_1 - y_2)^2 + (z_1 - z_2)^2}. \tag{5.9}$$

The absolute value of t_{tof} in nanoseconds is calculated using the speed of light:[6]

$$|t_{tof}| = \frac{d}{29.9792458\,\text{cm/ns}}. \tag{5.10}$$

In order to acquire an event sample where also the direction of flight and thereby the sign of t_{tof} is known with near certainty, only ontime events are selected. Although this constraint considerably reduces the number of tracks for the calibration, the number of beam induced muon tracks is sufficiently high. In four years of beam runs (2009–2012) more than 10^5 CNGS neutrinos interacted with the material in or in front of the OPERA detector and featured long muon tracks in z-direction. For a further reduction of the number of particles with the wrong direction of flight, i. e. atmospheric muons in negative z-direction which fall into the $40\,\mu\text{s}$ ontime window by chance, a cut on the vertical track slope is introduced. Only tracks with a fitted line that has a slope in the yz-plane between -0.7 and 0.8 are selected. In Figure 5.13 the slopes of all tracks in the yz-plane are shown, the two cut boundaries are indicated by dashed vertical lines. The sharp distribution in the middle is centered at about 0.06 and shows to the ontime events. This slope corresponds to the inclination of the CNGS beam facility (see Section 3.1). The second distribution with broader peaks, one for negative and one for positive slopes, shows the cosmic particles. Since the vast majority of cosmics reach the LNGS from above, negative slopes correspond to particles coming in from northwestern directions and positive slopes correspond to particles from southeastern directions. This way, the asymmetric structure of the Gran Sasso massif which provides a weaker shielding towards the southeast is reflected in the higher cosmic rates from that direction. The cuts on the slope mentioned above are chosen roughly symmetrical around the beam direction and discard about $1\,\%$ of the ontime

---

[4] The Kalman track is reconstructed using TT, RPC and PT digits. XPC entries are not used for the Kalman track reconstruction.

[5] Root mean square: square root of the arithmetic mean of the squares of a set of values

[6] All lengths, and in this case d, are given in centimeters within the OPERA software.
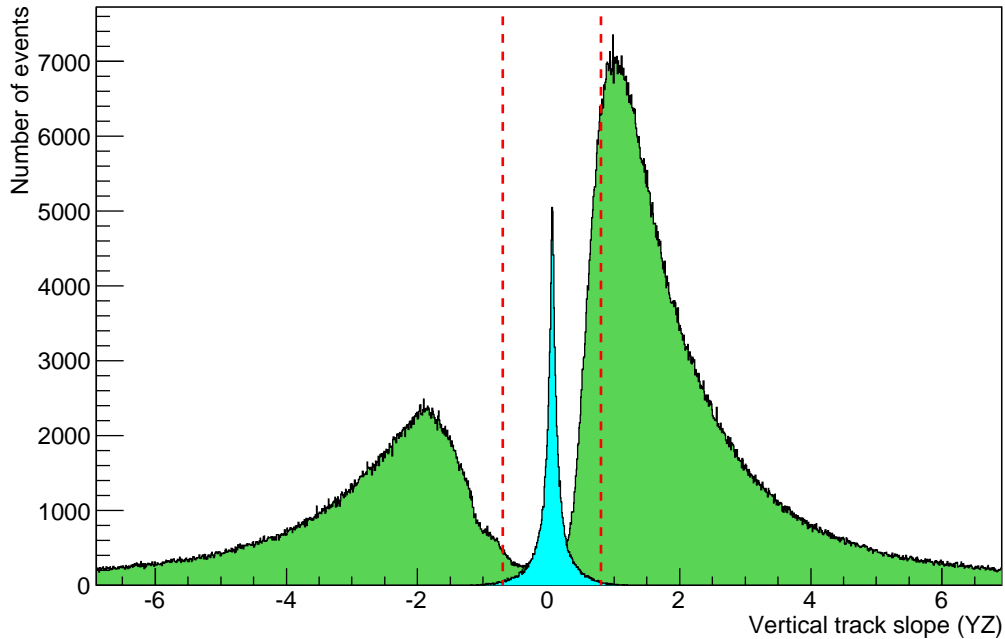
Figure 5.13: Slopes of all reconstructed tracks of the 2009–2012 dataset in the yz-plane. The blue distribution in the middle is centered at about 0.06 (slope of the CNGS beam) and shows the ontime events. The green distribution with broader peaks, one for negative and one for positive slopes, shows the cosmic particles. The cut boundaries on the slopes of ontime events at -0.7 and 0.8 are indicated by dashed vertical lines.

events, while they reduce the number of particles traveling against beam direction by excluding the majority of coinciding cosmics.

The XPC/RPC signal's propagation delay on the readout strip is determined by the distance from the point in the detector where the signal is produced to the end of the strip where the timing board is attached, and by the specific signal propagation velocity on the strip. Despite the restriction of the data sample to events with only one Kalman track, due to random noise in the XPCs/RPCs of individual trigger planes, wrong associations of trigger signals with points of interaction in the detector are still possible. Therefore, only events are selected where the XPC and RPC planes generating a trigger signal have exactly one readout signal for each coordinate, so that the interaction points can be determined without ambiguities. Note that the timing boards of one trigger plane can be distributed over up to three RPC planes (see Section 4.1.1). This has to be taken into account regarding the signal selection. For the same reason a strict limit on the so-called clustersize is set. The clustersize is the number of XPC/RPC readout strips per coordinate that carry a signal caused by the same interaction. For the horizontal readout, clustersizes of two

or more may lead to ambiguities in the association of detector signals with the attached timing boards due to their distribution over different RPC planes. And for the vertical readout, larger clusters may spoil the estimate for the propagation length on the signal strip. Therefore, only events are chosen where all XPC/RPC signals contributing to the trigger have a clustersize of 1. For beam events the average clustersize is always below three (see Figure 5.14). Because
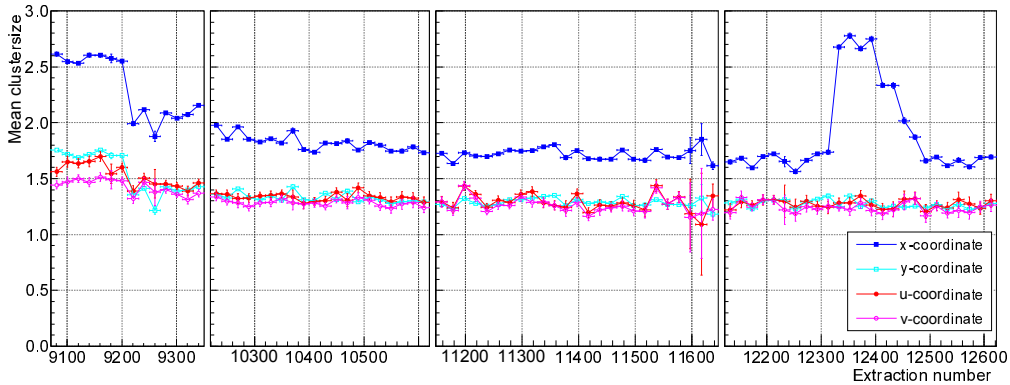
Figure 5.14: Clustersizes of all ontime events from the detector runs 2009–2012, averaged over 20 extractions. The extraction numbers start with a number corresponding to the year of the run, followed by a three-digit consecutive number. The drop in clustersize in 2009 and 2010 is due to several improvements in the XPC/RPC slow control and in the quality of the gas. The reason for the temporary increase in clustersize for the x-coordinate in 2012 is unknown.

the majority of ontime tracks crosses the detector planes at small angles with respect to the planes' normal, mostly short streamers evolve in the XPC's/RPC's gas volumes, which produce localized charges and induce a signal in only very few strips. The fluctuations in clustersize are based on changes in the detector's operating conditions, e. g. high voltage level, discriminator thresholds, gas pressure and gas quality [Pao14]. The different average clustersizes for the x- and y-coordinate are due to the different pitches of the readout strips, 2.6 cm for the vertical strips as compared to 3.5 cm for the horizontal ones. Although the XPC's readout strips have the same pitch as the vertical RPC ones, their average clustersizes are lower. This can be explained by the slightly different detector setup, using glass instead of Bakelite as highly resistive material. For an estimate of the frequentness of events with clustersize 1, Figure 5.15 shows the distribution of clustersizes for the x-coordinate of all ontime events in 2011. Almost 60 % of the events have a clustersize of 1 in x, therefore this cut can be used to improve the quality of the selected events without overly diminishing the number of events.
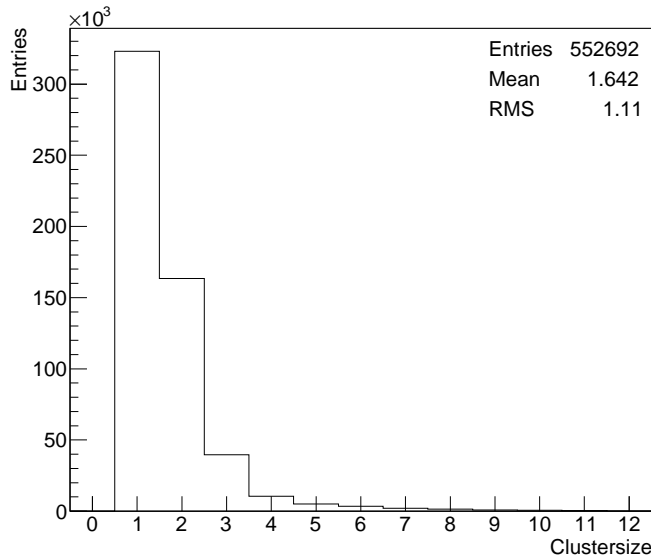
Figure 5.15: Clustersizes for the x-coordinate of all ontime events in 2011. Almost 60 % of the events have a clustersize of 1 in x.

The signal propagation velocities on the XPC and RPC readout strips differ slightly. For the XPCs a value of 25.5 cm/ns was measured, and for the RPCs 22.0 cm/ns [Ber14, B⁺12c]. These measurements were taken in situ on XPCs/RPCs installed in the detector. Test bench measurements on an RPC not surrounded by dense material like the magnets' iron slabs revealed higher propagation velocities, similar to the ones for the XPCs [B⁺12a]. This indicates a possible effect of the RPCs' surroundings beyond the ground plate (see Figure 3.9) on the way signals propagate on the readout strips.

Summarizing, the following cuts are applied to select events for the calibration of signal path A:

- Only events with exactly one reconstructed 3D Kalman track are selected.

- Each track has to have at least 70 digits.

- The RMS of the residuals of the linear regression with all track digits has to be below 3 cm in both projection planes (xz and yz).

- The maximum residuals have to be below 5 cm in both projection planes.

- Only ontime events are selected.

- The slope of the straight line fitted to the track has to be between −0.7 and 0.8.

- Exactly one readout signal per coordinate is required for all XPC/RPC trigger planes that delivered a signal.

- A clustersize of 1 for both coordinates is required for all XPC/RPC trigger planes that delivered a signal.

Figure 5.16 exemplarily shows the difference $\Delta t_{A95} \equiv t_{A9} - t_{A5}$ in propagation delay on path A between trigger channels 9 and 5 of SM 1 according to Equation 5.8. Trigger channel 5 of each SM is taken as reference for all relative corrections within the corresponding SM. The correction values for all channels are listed in Table 5.5. The standard deviation σ shows a spread of the measurements of about 5 ns for all trigger channels. This indicates deviations in the lengths of the cables A' within each trigger channel which cannot be identified by this calibration. As the logic OR of the signals from the 14 timing boards of each channel is built in the OPE (see Section 4.1.1), the calibration of path A does correct differences in the lengths of the cables A'', but can only correct the mean differences between the sets of 14 cables A' of each trigger channel.
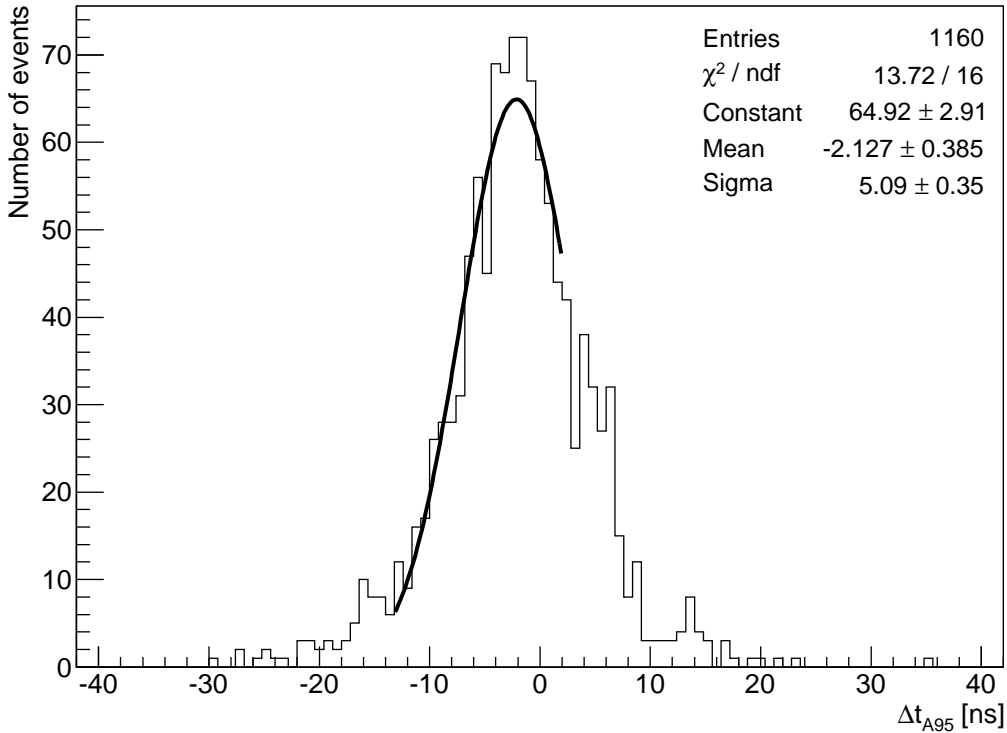
Figure 5.16: Difference $\Delta t_{A95} \equiv t_{A9} - t_{A5}$ in propagation delay on path A between trigger channel 9 and trigger channel 5 (reference channel) of SM 1 according to Equation 5.8

Table 5.5: Correction values for the signal propagation delays on signal path A. The correction values are expressed with respect to the first RPC plane (trigger channel 5) of the same SM, the value of which is set to zero. σ is the standard deviation of the Gaussian fit (see Figure 5.16).

SM	Trigger Channel	Rel. Correction for t_A [ns]	σ [ns]
1	1	-25.1 ± 0.5	5.0
1	2	0.2 ± 0.8	5.4
1	3	-19.0 ± 0.5	4.2
1	4	7.0 ± 0.6	5.4
1	5	0.0	—
1	6	-2.6 ± 0.4	5.3
1	7	-9.0 ± 0.2	5.4
1	8	-2.9 ± 0.3	5.2
1	9	-2.1 ± 0.4	5.1
1	10	-5.1 ± 0.4	4.9
1	11	-4.2 ± 0.3	5.3
2	1	-14.4 ± 0.4	5.6
2	2	9.3 ± 0.4	5.6
2	3	-13.6 ± 0.7	5.2
2	4	12.4 ± 0.4	5.5
2	5	0.0	—
2	6	1.6 ± 0.2	5.1
2	7	0.2 ± 0.3	4.9
2	8	-1.8 ± 0.2	5.4
2	9	-27.2 ± 0.2	5.3
2	10	-25.1 ± 0.2	5.1
2	11	-24.2 ± 0.4	5.3

Chapter 6

Calibration Results and Time of Flight Measurement

In a similar way as a spatial misalignment of the drift tubes, which is not corrected in the reconstruction software, reduces the spatial resolution of the PT, also uncompensated deviations in the trigger signal timing impair the results of the track reconstruction. Since the track information is directly derived from time measurements, inaccuracies in the timing likewise diminish the spatial resolution. In the case of misalignment of a detector part, e.g. a drift tube module, all tracks passing through that section are affected. However, if the trigger signal is generated by a trigger plane the signal path of which is not correctly calibrated, all PT tracks in the same SM are compromised. This effect becomes more prominent if signal path A (see Figure 5.2) of the trigger channel in question is shorter than anticipated, as it is for all channels of the last trigger station in SM 2 (see Section 5.5). In this case the probability that the station delivers the first signal and produces the common stop is increased due to its smaller propagation delay on the way to the OTB, causing an even greater number of tracks to be reconstructed with inaccurate timing information. That way, a single short and uncalibrated cable from one of the eleven trigger channels may spoil a significant percentage of all tracks in the same SM, and even more so for beam induced events which usually cross several trigger stations. Therefore, the timing correction values obtained by the analysis presented in Chapter 5 are essential for the track reconstruction quality, and they are now implemented in the software to ensure the best possible spatial resolution for the drift tubes and to allow for time of flight measurements on atmospheric muons crossing the spectrometers.

6.1   Validation of the Timing Corrections

An adequate measure for the quality of the track reconstruction is the distribution of the residuals of all drift tube signals contributing to the track fit. The residuals are the shortest distances between the drift circles, determined by the drift time measurement, and the reconstructed track. Provided that different control parameters indicate a well-performing reconstruction procedure, the RMS of the residuals' distribution can directly be taken as a measure for the spatial resolution: for one thing, the distribution of the residuals for a large number of tracks has to be symmetric and centered at zero. If the distances to the drift circles left and right of the tracks do not balance out statistically, then a systematic error affects the fit, e.g. a general time offset of the trigger signal. For another thing, the mean of the χ^2 distribution per number of degrees of freedom has to be close to one. χ^2 is the quantity that is iteratively minimized during the track fit procedure in order to find the optimum fit, and the number of degrees of freedom is the number of drift tubes used for the fit minus the number of fit parameters, which is two, since the PT only provides two-dimensional track information. For an ideal fit χ^2 equals the number of degrees of freedom. A further parameter for monitoring the validity of the track fit is the χ^2 probability distribution. The probability density function for a χ^2 distribution is given by

$$f(x) = \frac{x^{(n/2)-1}e^{-x/2}}{2^{n/2}\Gamma(n/2)} \qquad \text{for} \quad x \geq 0, \tag{6.1}$$

where n is the number of degrees of freedom and Γ is the gamma function, defined for positive real numbers p by

$$\Gamma(p) = \int_0^\infty x^{p-1}e^{-x}\,\mathrm{d}x \qquad \text{for} \quad x > 0. \tag{6.2}$$

The probability of finding a χ^2 for n degrees of freedom that is greater than x is then

$$P_{\chi^2} = \int_{\chi^2}^\infty f(x)\,\mathrm{d}x \qquad \text{for} \quad x > 0. \tag{6.3}$$

In the ideal case, where the fits accurately describe the particle tracks, the χ^2 probability distribution is flat between its boundary values of zero and one and therefore has a mean value of 0.5. In a realistic case, however, the distribution increases slightly towards zero and one, but should still be symmetric around 0.5. The excess for low probabilities is due to tracks which cannot be fitted correctly, e.g. when the particle scattered and changed direction between drift tube layers or walls. Higher χ^2 probabilities occur more often when the track fit is better than it can be expected from the spatial

resolution of the detector. This may happen if noise signals are mistaken for being part of the track and which then provide a good fit merely by coincidence.

In order to demonstrate the effect of the timing corrections on the PT track reconstruction quality, three different sets of values are tested (see Sections 6.1.1–6.1.3). The values are implemented in the drift tube reconstruction software in the subprogram `DTubeCosmicProp_ToF` that is part of the package `DTubeReco` which in turn is a component of `OpRec`, the package for the event reconstruction in the electronic detectors. For details on the track reconstruction for the drift tubes see [Won07]. The dataset used in this section for the validation of the timing corrections consists of the 2010 ontime events. It has to be noted that for each set of values the general timing offset corrections, which are applied to all trigger signals of the same SM (see Chapter 5), had to be adjusted for the residuals' distribution to be centered around zero. The position of the distribution's center is sensitive to the average deviation in timing of the different trigger signal paths. To get comparable results for all three scenarios, the general timing offset corrections have been determined for each one and were adapted in the track reconstruction software accordingly. However, the resolution function, which describes the drift tubes' spatial resolution as a function of the drift time inside the tubes, is not recalculated for each scenario. The function can be determined during the calibration of the track reconstruction software by iterating over the fit procedure of selected straight tracks (see [Won07]). For all three sets of timing correction values, the resolution function optimized for the third and final set (Section 6.1.3) is used. As a consequence, the average spatial resolution of the drift tubes is overestimated for the track fits when using the first two sets of values (Sections 6.1.1 and 6.1.2). This leads to a distortion of the distributions described above: the residuals' distribution exhibits asymmetries with respect to its peak, the mean of the χ^2 distribution per number of degrees of freedom is higher and the χ^2 probability distribution is shifted towards lower values. Nevertheless, the width of the track residuals' distribution is basically unaffected by the use of a non-optimal resolution function and remains a valid indicator for the achieved spatial resolution and thereby for the quality of the timing calibration.

6.1.1 Initial Cable Corrections

To test the effect, an insufficient knowledge of the trigger timing has on the track reconstruction for the drift tube detector, propagation corrections according to the initially planed cable lengths as specified in [S⁺08] are used. As stated in Section 5.5 the deviations in length for the actually installed cables A'' range from 0 up to 10 m. For all cables on signal paths A and B a propagation delay of 5.7 ns/m is assumed, since the 3M 2100 Series cable was

originally foreseen for every twisted pair cable of the trigger system. For path C the results of the OTB test pulse measurements are taken (see Table 5.1). The small corrections due to slight differences in the signal delay for the stop signal distribution (see Section 5.2.2) are not applied here. The values that are used for the initial cable corrections, again relative to trigger channel 5 of the corresponding SM, are listed in Table 6.1.

Table 6.1: Relative correction values for the signal propagation delays on signal paths A, B and C according to the initially envisaged cable lengths. Trigger channels 1–4 belong to the XPCs which were planned to have 2 m longer cables for signal path A. For path C the results of the OTB test pulse measurements are used. The correction are expressed relative to the first RPC plane (trigger channel 5) of the corresponding SM.

SM	Trigger Channel	Rel. Correction for t_A [ns]	Rel. Correction for t_B [ns]	Rel. Correction for t_C [ns]
1	1–4	11.4	0.0	0.0
1	5	0.0	0.0	0.0
1	6–8	0.0	0.0	−4.5
1	9–11	0.0	51.3	3.4
2	1–4	11.4	0.0	0.0
2	5	0.0	0.0	0.0
2	6–8	0.0	51.3	−13.2
2	9–11	0.0	51.3	10.5

The distribution of the residuals of all drift tube signals that are used for the track fits of the 2010 ontime data are shown in Figure 6.1. It exhibits an asymmetric pattern and lacks a defined peak. The distribution of the χ^2 per number of degrees of freedom has a mean value above 2.5. Moreover, the distribution of the χ^2 probability is not flat but shows an excess towards small P_{χ^2} (see Figure 6.2), leading to a mean probability of 0.22. As elaborated above, these are indications for an overestimation of the spatial resolution in the resolution function used for the track fits, implying that the initial cable corrections are inferior to the final ones concerning the track reconstruction accuracy. And in fact, the RMS of the residuals' distribution of 396 μm fails to reach the spatial resolutions achieved for test setups with a well known and almost constant trigger timing by more than 100 μm (see e.g. [Old09] and [Len07]), showing that the fitted tracks do not accurately reflect the recorded data.
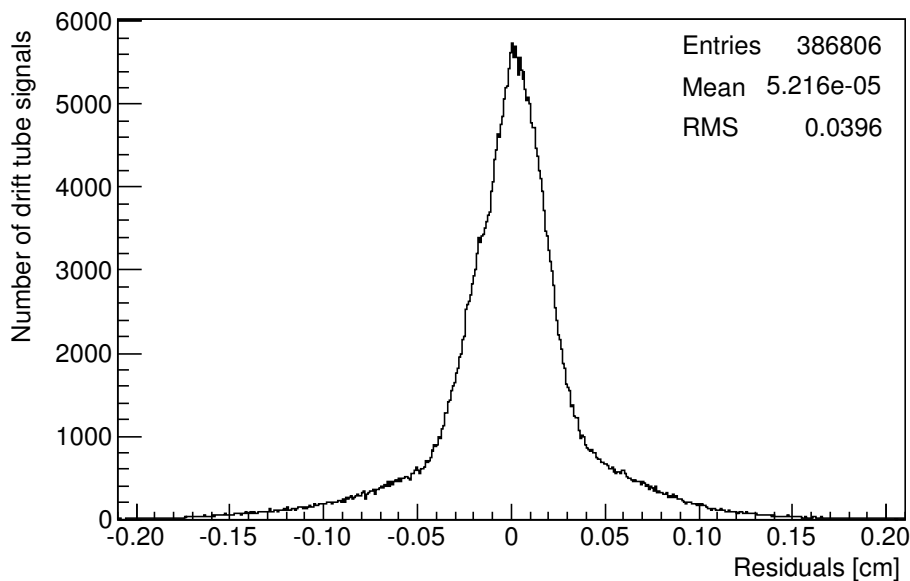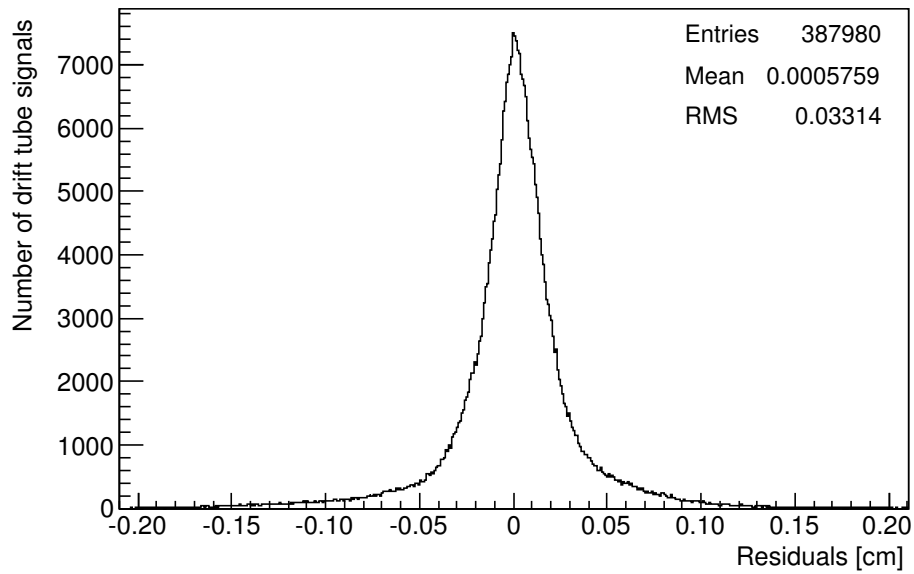
Figure 6.1: Distribution of the residuals of all drift tube entries contributing to the track reconstruction for the 2010 ontime data. The signal propagation delays of the trigger system are corrected according to the initially envisaged cable lengths as specified in [S+08] and by using the results of the OTB test pulse measurements.

In summary, it can be stated that for the present scenario the control parameters indicate a not yet properly performing track reconstruction. Without further tests, the exact reason for this cannot be established. For instance, a misalignment of the drift tubes can have the same negative effect on the track reconstruction. But since the signal propagation corrections are the only parameters that are changed in this section, the differences in spatial resolution between the three sets of correction values can be attributed to the influence of the trigger timing.
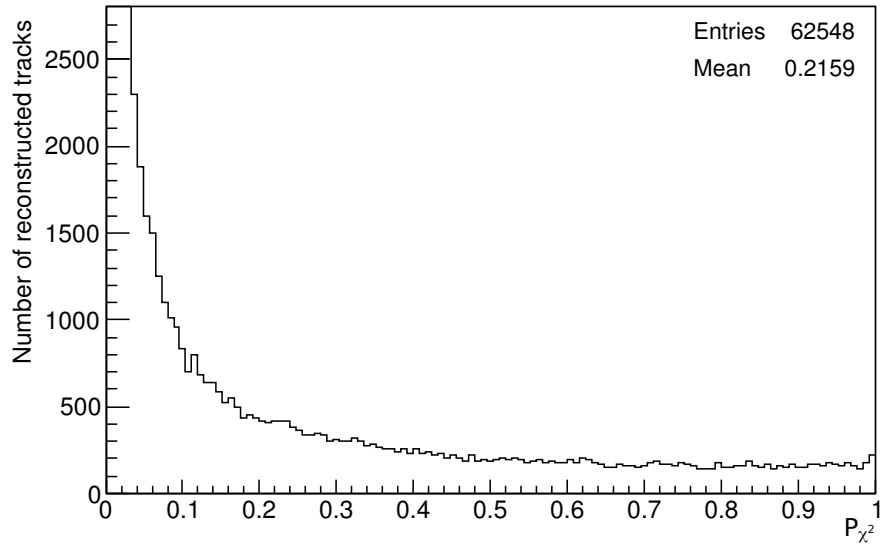
Figure 6.2: Distribution of the χ^2 probability of the reconstructed tracks for the 2010 ontime data. The signal propagation delays of the trigger system are corrected according to the the initially envisaged cable lengths as specified in [S+08] and by using the results of the OTB test pulse measurements.

6.1.2   Rough Cable Corrections

This set of correction values takes into account the lengths and types of the actually installed twisted pair cables. All cables A$''$ and B were inspected by eye. The latter are in accordance with the initial cabling plan. The lengths and types found for cables A$''$ are listed in Table 5.4 whereas the lengths of the cables A$'$ could not be verified because they are inaccessible. The correction values used here are listed in Table 6.2. The values for signal paths B and C are the same as in Section 6.1.1.

Figure 6.3 shows the distribution of the residuals using the rough cable corrections. In contrast to the one for the initial corrections, this distribution is closer to a symmetric shape. The RMS of $331\,\mu$m indicates an improved spatial resolution with respect to the initial cable corrections but does not yet meet the expectations raised by the test setup measurements. The distribution of the χ^2 per number of degrees of freedom has a mean value of about 1.9, and the distribution of the χ^2 probability (see Figure 6.4), though being almost leveled out, still exhibits an excess for low values of P_{χ^2}, leading to a mean probability of about 0.37. This implies a still present overestimation of the spatial resolution by the resolution function.

Table 6.2: Relative correction values for the signal propagation delays on signal paths A, B and C according to the actually installed cable lengths and types. The unverified lengths of the cables A′ are taken from [S⁺08]. The values for signal paths B and C are the same as in Section 6.1.1.

SM	Trigger Channel	Rel. Correction for t_A [ns]	Rel. Correction for t_B [ns]	Rel. Correction for t_C [ns]
1	1	−21.5	0.0	0.0
1	2	3.5	0.0	0.0
1	3	−21.5	0.0	0.0
1	4	3.5	0.0	0.0
1	5	0.0	0.0	0.0
1	6	−2.9	0.0	−4.5
1	7	−2.9	0.0	−4.5
1	8	−2.9	0.0	−4.5
1	9	−2.9	51.3	3.4
1	10	−2.9	51.3	3.4
1	11	−5.9	51.3	3.4
2	1	11.4	0.0	0.0
2	2	11.4	0.0	0.0
2	3	11.4	0.0	0.0
2	4	11.4	0.0	0.0
2	5	0.0	0.0	0.0
2	6	0.0	51.3	−13.2
2	7	0.0	51.3	−13.2
2	8	0.0	51.3	−13.2
2	9	−28.5	51.3	10.5
2	10	−28.5	51.3	10.5
2	11	−28.5	51.3	10.5

Therefore, further improvements of the trigger timing corrections are necessary. For one thing, possible differences in the lengths of cables A′ have to be addressed, for another thing, apparently also smaller deviations in the propagation delays of cables of the same length have to be compensated.

Figure 6.3: Distribution of the residuals of all drift tube entries contributing to the track reconstruction for the 2010 ontime data. The signal propagation delays of the trigger system are corrected using the actual lengths for cables A″ and B and their specific propagation delays per meter (see Sections 5.4 and 5.5).
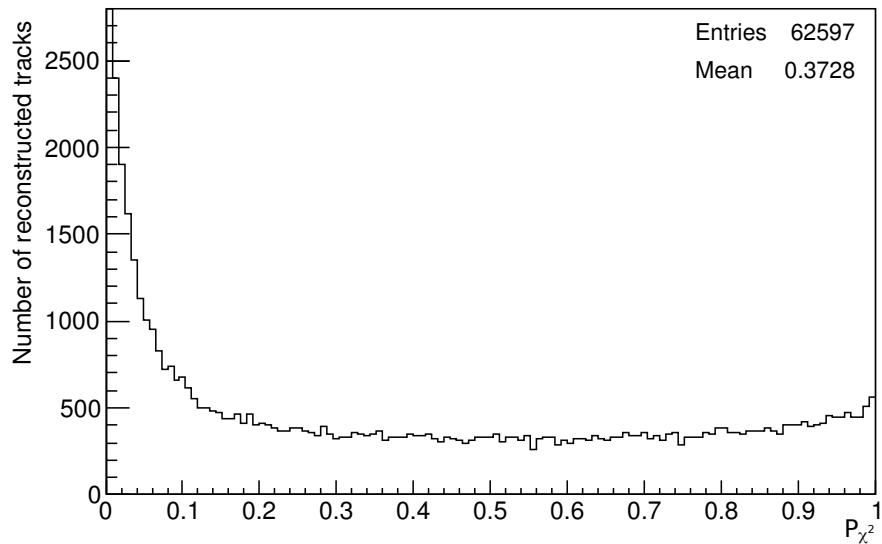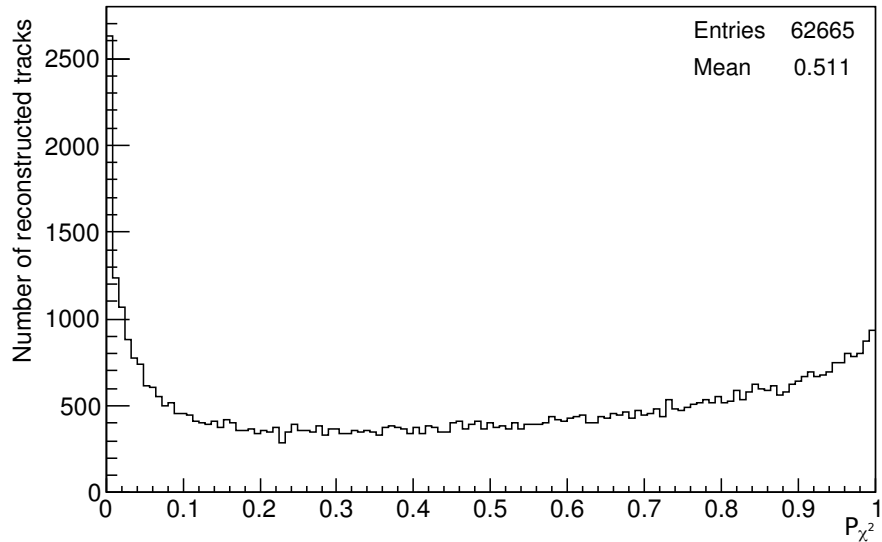

Figure 6.4: Distribution of the χ^2 probability of the reconstructed tracks for the 2010 ontime data. The signal propagation delays of the trigger system are corrected using the actual lengths for cables A″ and B and their specific propagation delays per meter (see Sections 5.4 and 5.5).

6.1.3   Fine Corrections Using Calibration Results

Finally, in this section all calibration results presented in Chapter 5 are implemented in the track reconstruction software. For signal path A each individual trigger channel is calibrated by comparing the signals of about 10^3 selected tracks with the signal from a reference channel (see Section 5.5). The resulting correction values now also include cables A′. To measure delay differences on path B, several 10^4 selected signals per trigger channel are used (see Section 5.4). And for signal path C the small deviations in the propagation delays behind the OTB master output (see 5.2.2) are now corrected in addition to the different delays on the OTBs themselves. All relative correction values used in this section are listed in Tables 5.3 and 5.5.

The distribution of the residuals using all calibration results from Chapter 5 is shown in Figure 6.5. It is symmetric in shape and centered at zero. The RMS of 255 µm is compatible with the spatial resolution achieved with the test setups. The distribution of the χ^2 per number of degrees of freedom has a mean value of about 1.3, indicating that, on average, the track fits are valid hypotheses for describing the recorded data. Figure 6.6 shows the χ^2 probability distribution. As expected for a well performing track reconstruction, the distribution is flat with minor excesses towards zero and one, and its mean of 0.51 is close to the expected value of 0.5.

Summarizing, it can be stated that for the fine corrections of the trigger signal timing all control parameters indicate a correctly functioning reconstruction procedure. By means of the presented calibration, the same spatial resolution is reached for the OPERA PT, with its widely distributed eleven trigger channels per SM, as for the test setups, where every trigger signal is generated by a coincidence signal of the same two small scintillator planes, which are placed close to the drift tubes, and therefore with an almost constant timing. Since the only differences between the three scenarios considered in this chapter are the correction values for the trigger signal propagation delays, and since all three sets of values where examined using the same dataset, the improvements in the track reconstruction quality and especially the satisfactory results using the fine corrections can be attributed to a now calibrated trigger system.
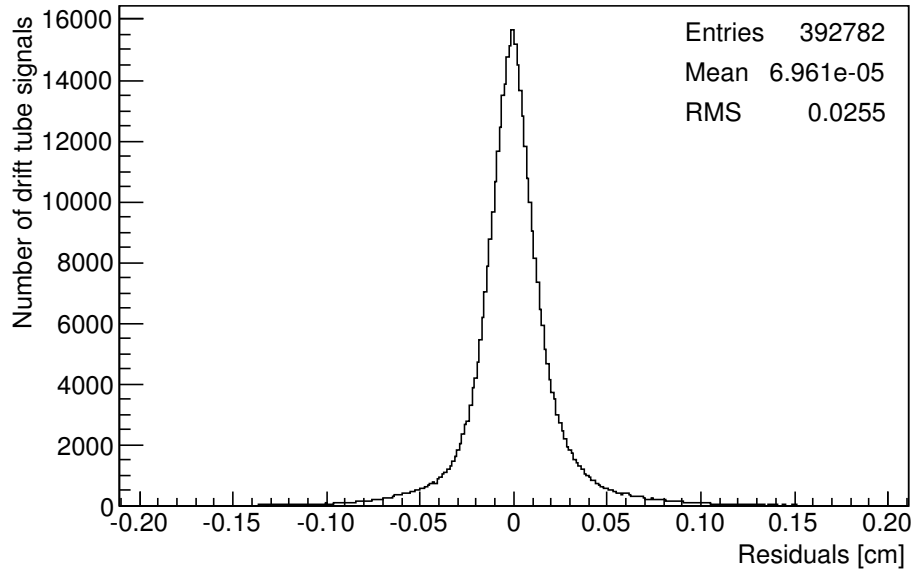
Figure 6.5: Distribution of the residuals of all drift tube entries contributing to the track reconstruction for the 2010 ontime data. The signal propagation delays of the trigger system are corrected using all calibrations described in Chapter 5.

Figure 6.6: Distribution of the χ^2 probability of the reconstructed tracks for the 2010 ontime data. The signal propagation delays of the trigger system are corrected using all calibrations described in Chapter 5.

6.2 Temperature Dependence of the Trigger Timing

In 2011 a fluctuating shift of the mean value of the residuals in the PT track reconstruction was noticed [Won11]. As explained in Section 6.1, the mean of the residuals is supposed to be constant and approximately zero if all calibrations are taken into account and if the general offset values described in Chapter 5 are set accordingly. Therefore, a time-dependent effect must be responsible for the fluctuations. Subsequently, a possible correlation between the ambient temperature of the experimental hall at the LNGS and the observed variations of the mean residuals was investigated. One possible explanation for such variations may be a change in the trigger timing, which in turn may be due to a temperature-dependent signal propagation delay in the trigger system. In Section 6.2.1 the effect of temperature changes on the OTB, the central electronics component of the trigger system, is studied. And in Section 6.2.2 an approach for a temperature compensation for the trigger timing is tested.

6.2.1 Temperature Dependence of the Trigger Board Delay

The total delay of the trigger signal from the timing boards to the TDC stop inputs is roughly $2\,\mu s$ (see Figure 4.4). The greatest contribution (about $80\,\%$) of this delay comes from the OTB. And on the OTB the two delay lines DS1110-500[1] for the TROUT signal (see Figure 4.8) provide the major part of the board's delay. These delay lines are sensitive to temperature changes. Over their entire operating temperature range from $-40\,°C$ to $85\,°C$ their delay exhibits an approximately linear temperature dependence with a negative temperature coefficient, so that the delay value decreases with increasing temperature [Max02]. In principle the changes in the OTB delays could be measured on-site using the boards' test pulse systems and TDCs described in Section 4.1.2. The on-board TDCs possess a built-in temperature compensation (see [MSC10]), so that the measured propagation delays actually show the temperature effect on the OTB circuits and are not distorted by the temperature dependence of the TDC. But the results of these time measurements are only available with nanosecond precision (see Section 5.2.1) and the temperature changes at the detector are too small to obtain a reliable temperature calibration. Therefore, the OTB delay was measured with an oscilloscope and in a small laboratory, offering higher measurement precision and a wider range of temperatures that could be adjusted at will.

---

[1] Maxim DS1110-500 10-Tap Silicon Delay Line, Maxim Integrated Products, $500\,ns$ delay per unit

For the delay measurements a pulse generator was used to send TTL pulses both to an oscilloscope and through a TTL to PECL converter to the PECL input stage of the OTB master. The TTL output signal from the OTB master was sent to a second channel of the oscilloscope, which then determined the delay between the two TTL signals, averaged over several hundred pulses with a statistical error of about 0.6 ns. The temperature in the laboratory, where the OTB was operated, was lowered to 18 °C and then over two days slowly raised to 26 °C. The slow speed of the temperature change justifies the approximation that the OTB was in thermal equilibrium with the surrounding air at all times. An alcohol thermometer, read out by eye, was used to determine the ambient temperature with an accuracy of about ±0.2 °C. To avoid any temperature effects on the equipment which was used to measure the delay, the pulse generator and the oscilloscope where kept in another room at constant temperature in between measurements. Figure 6.7 shows the measured values and a linear fit to the data. The hereby obtained calibration indicates that an increase in temperature of 1 K causes the OTB master delay to decrease by (0.77 ± 0.09) ns.[2] Note that the measured delay values shown in Figure 6.7 include the signal propagation delays on the short cables to and from the board, as well as the delay of the TTL to PECL converter used for this measurement. The values are therefore higher than the actual propagation delay of the OTB master. However, for the designated temperature calibration the absolute values are irrelevant.
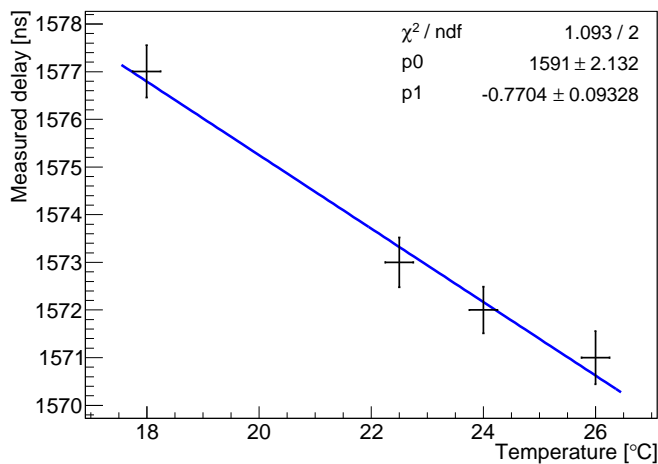
Figure 6.7: Temperature calibration of the signal propagation delay on the OTB master for ambient temperatures from 18 to 26 °C. The blue line is a linear fit to the data, p1 is the slope and p0 the y-intercept. The error in temperature of ±0.2 °C is due to the readout of the thermometer by eye. The error of the measured delay is the statistical error of the oscilloscope measurements.

---

[2] This statement is only valid for temperatures that are covered by the calibration measurements. However, the temperatures in hall C of the LNGS lie in or near the specified range (see Figure 5.5).

6.2.2 Temperature Compensation for the Trigger Timing

The temperature dependence of the OTB delays affects all trigger stations alike. Therefore, the compensation factor of -0.77 ns per 1 K is applied to the trigger timing globally. The current average temperature in hall C is determined by using the sensors which are connected to PT preamplifier boards and read out by the slow control system as described in Section 5.2.1. Since this part of the slow control information was not integrated in the `ROOT` files containing the detector data, the value of `hallC_temp` is added to the data files manually. The timing compensation value is then calculated within the track reconstruction software for each event individually using the temperature at the time of the event. Temperature changes relative to the value of 18.6 °C, the average temperature for which signal path C is calibrated (see Section 5.2.1), are compensated by adding/subtracting the corresponding number of nanoseconds to/from the general timing offset values. For testing this temperature compensation, the data of the 2012 run is chosen because it exhibits the greatest temperature variations (see Figure 5.5). Figure 6.8 shows the mean of the residuals of all drift tube entries contributing to the track reconstruction for the 2012 data with constant trigger timing. The mean value is determined per data extraction. Its steep increase at the beginning of the run coincides with an increase in the average temperature of hall C, whereas the sudden drop in temperature by about 2 K at the beginning of May (extraction 12210) is not reflected in the mean of the track residuals. Nevertheless, the inclusion of the temperature compensation leads to a visible effect: Figure 6.9 shows the mean of the track residuals for the same dataset, but now the trigger timing is corrected for the temperature-dependent change in delay. As a result the maximum variations in the mean value are reduced to about half as compared to the uncompensated timing. Yet there is no effect on the PT's spatial resolution whatsoever.

In conclusion, the influence of the ambient temperature on the OTBs' propagation delay is verifiable but can be neglected concerning the detector's performance. A further variation in the timing of the drift tube signals is caused by temperature changes of the drift gas. Since the PT gas system maintains a constant gas pressure inside the tubes within the limits of 1000 mbar and 1010 mbar [F$^+$08], a rise in temperature is equivalent to a decrease of the gas density. This in turn causes the electron drift velocity to increase [Kre08], so that the signals on the anode wires are generated earlier and consequently the drift time measurements on the TDCs are started sooner. The early start of the TDCs counteracts the early arrival of the common stop signal due to the reduced OTB delay for higher temperatures. However, the drift time for each tube and event depends on the individual drift distance. For this reason, a change in the electron drift velocity cannot be
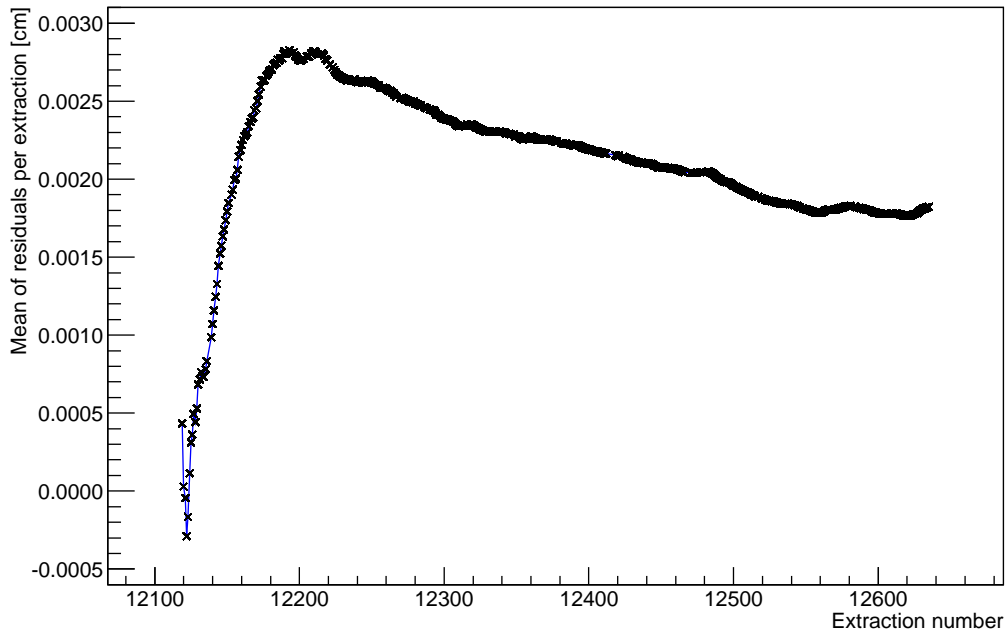
Figure 6.8: Mean of the residuals of all drift tube entries contributing to the track reconstruction per extraction for the 2012 data with constant trigger timing
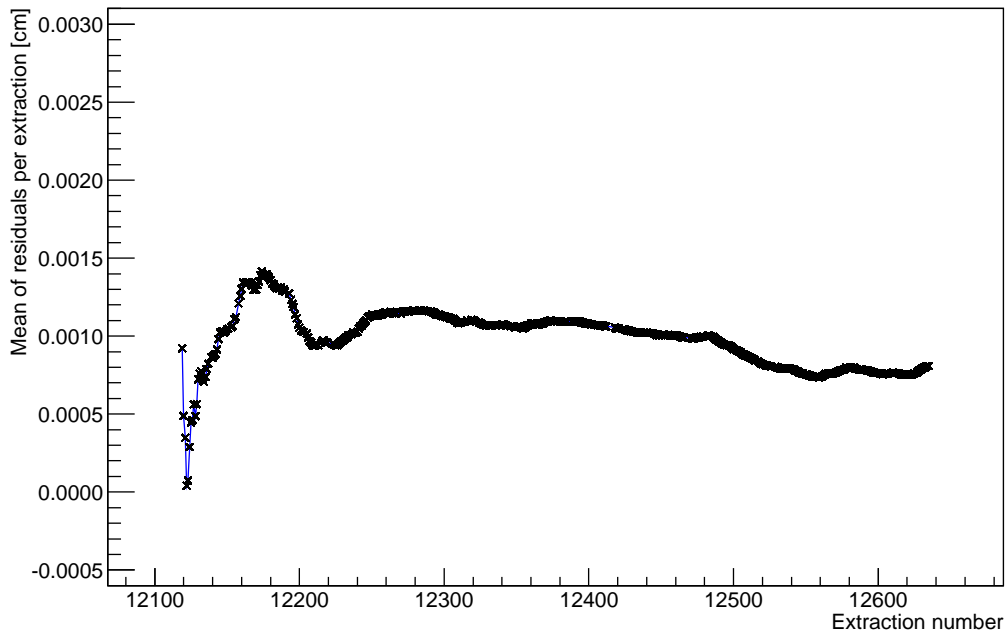
Figure 6.9: Mean of the residuals of all drift tube entries contributing to the track reconstruction per extraction for the 2012 data, applying a temperature compensation of $-0.77\,\mathrm{ns}$ per $1\,\mathrm{K}$ to the trigger timing

compensated globally by a timing offset. Instead, a separate time to distance relation would have to be determined and used for each gas temperature. But as shown in [Old09], the PT's design specifications concerning the spatial resolution are met even for temperature variations of the drift gas up to 6 K. Therefore, no further approach to compensate temperature effects is considered.

6.3 Time of Flight Measurement

All timing calibrations applied, the PT trigger system can now be used to determine the direction of flight of particles passing through the detector by measuring their time of flight between trigger planes as outlined in Section 5.1. Due to the remaining uncertainties in the timing, the track has to cross several trigger planes in order to increase the probability of a correct direction of flight identification. To obtain more than five trigger plane signals, the particle has to pass through at least one magnet arm, implying a minimum transit of 60 cm of steel. Therefore, a direction of flight determination is only possible for muons that are crossing a spectrometer.

The OPERA detector is optimized for the detection of particles traveling in beam direction, that is at small angles towards the z-axis. Accordingly, the planes of the different electronic detectors are oriented parallel to the xy-plane (see Figure 3.5), and in the case of the PT trigger planes they are up to about 1 m apart. However, the majority of particles, for which a direction of flight identification is of interest, i.e. atmospheric muons, are crossing the detector at larger angles towards the z-axis. Therefore, not all particles crossing a spectrometer also cross two or more trigger planes. But despite the fact that the given geometrical setup of the detector is far from ideal for the study of cosmic rays, it still allows to perform time of flight analyses for a subsample of the recorded atmospheric muon tracks.

To identify a particle's direction of flight, its time of flight between different trigger planes is plotted as a function of the distance of flight (see Figures 6.10–6.13). For each SM, the first trigger plane in beam direction, that generated a signal, is taken as reference. The flight times and distances to all following trigger planes of the same SM are expressed relative to the corresponding reference plane. To determine the distance of flight between trigger planes, a linear regression with all Kalman track digits is done for each projection plane (xz- and yz-plane), in the same way as for the calibration of signal path A (see Section 5.5). The distance traveled by a particle between two trigger planes is calculated using the intersection points of the fitted straight line with the planes, and Equation 5.9. The time of flight is determined as

described in Section 5.1 and illustrated in Figure 5.4: for each signal the estimated propagation time on the RPC/XPC signal strip, the propagation times on signal paths A and B, and the time measured by the TDC are added. The time of flight between two trigger planes is the difference between the respective sums.

For the reference plane of SM 1, the entry in the flight time over distance plot is set to (0,0). All flight times determined by planes in SM 2 have to be shifted by the time of flight between the reference planes of the two SMs. This shift is approximated by, once again, using the linear track fit for the flight distance, and by assuming that the particle travels at the speed of light c. Regarding the two SMs, there are only two possible directions of flight: either the particle enters the detector through SM 1 and then travels towards SM 2, or vice versa. In the first case, the time of flight between the reference planes has to be added to all flight times determined by SM 2. In the second case, it has to be subtracted from them. Both possible hypotheses are tested for each event. A straight line is fitted to the data points, for the first hypothesis with a fixed slope of $1/c$ and for the second one with a slope of $-1/c$. Then the residuals for each fit are determined and compared with each other. For the plot in which the correct direction of flight between the SMs is assumed, the RMS of the residuals should be smaller than for the plot referring to the wrong hypothesis. This is illustrated with two exemplary events: Figures 6.10 and 6.11 show the flight time over distance plot for a beam event, and Figures 6.12 and 6.13 show the plot for a cosmic event. The direction of flight for the ontime event is known to be the beam direction. In Figure 6.10 the opposite direction is assumed. Here, the time of flight between the reference planes of the two SMs is subtracted from the times determined by the two trigger planes in SM 2, and the slope of the linear fit (p1) is set to $-1/c$. The resulting RMS of the residuals is 9.4 ns. In Figure 6.11 the time of flight between the two reference planes is added to the times from SM 2, and, accordingly, the straight line is fitted with a fixed slope of $1/c$. The lower RMS of the residuals of 2.2 ns confirms the validity of the hypothesis that the particle traveled in beam direction.

The direction of flight for the cosmic event is unknown. Figure 6.12 shows the flight time over distance plot for the hypothesis that the particle is flying in beam direction. The resulting RMS of the residuals is 10.5 ns. The corresponding plot for the opposite direction is shown in Figure 6.13. The lower RMS of the residuals of 4.6 ns favors the hypothesis that the cosmic particle traveled against the direction of the beam.
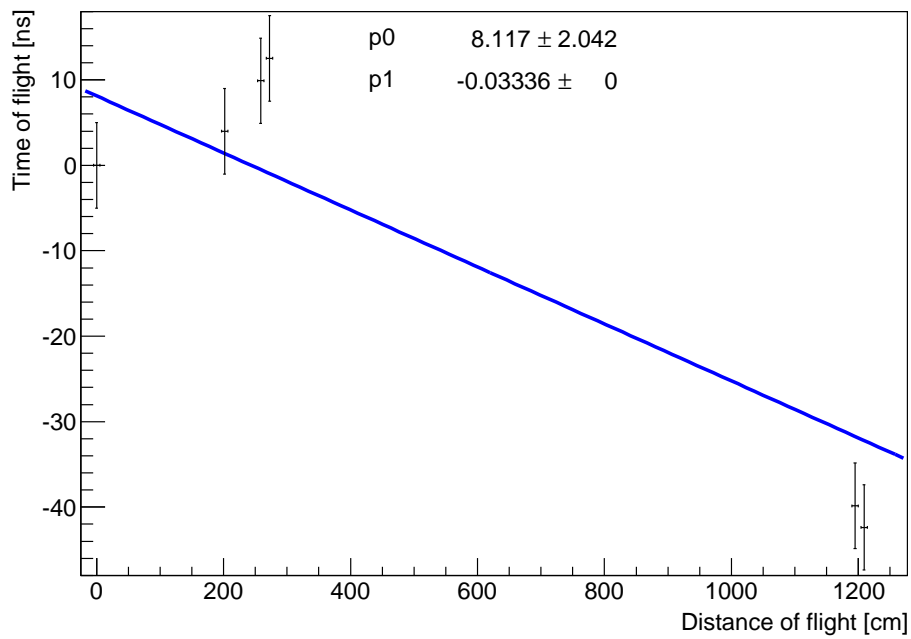
Figure 6.10: The time of flight as a function of the distance of flight for an ontime event from extraction 11535 (2011 beam run), assuming the particle traveled against beam direction. The RMS of the residuals is 9.4 ns.
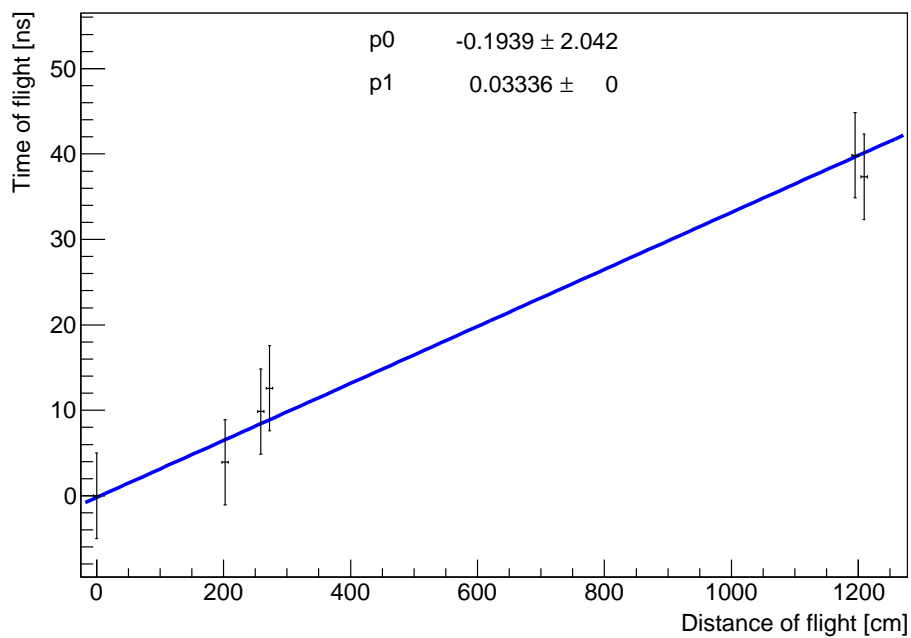
Figure 6.11: The time of flight as a function of the distance of flight for an ontime event from extraction 11535 (2011 beam run), assuming the particle traveled in beam direction. The RMS of the residuals is 2.2 ns.
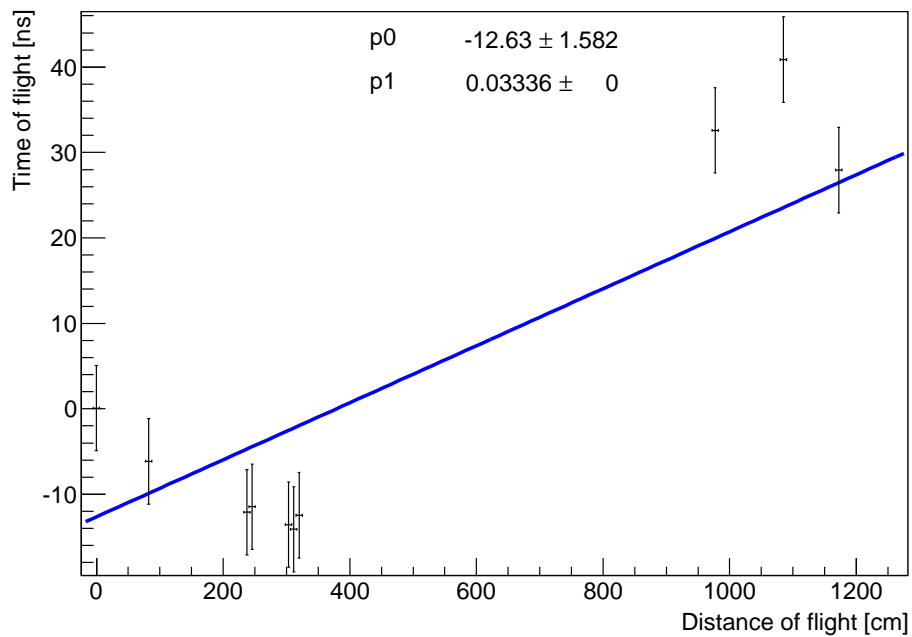
Figure 6.12: The time of flight as a function of the distance of flight for a cosmic event from extraction 11535 (2011 beam run), assuming the particle traveled in beam direction. The RMS of the residuals is 10.5 ns.
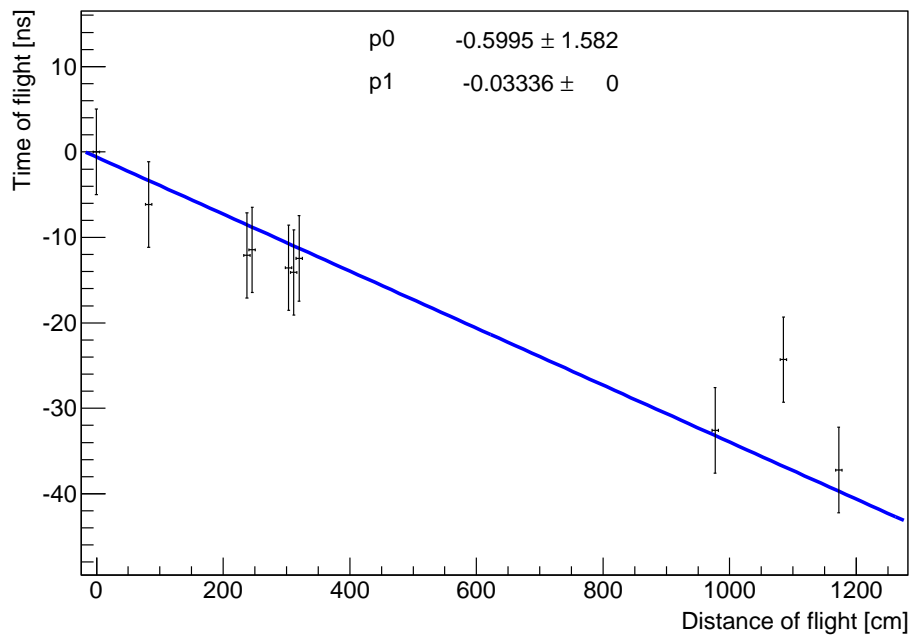
Figure 6.13: The time of flight as a function of the distance of flight for a cosmic event from extraction 11535 (2011 beam run), assuming the particle traveled against beam direction. The RMS of the residuals is 4.6 ns.

To obtain an estimate of the error of the flight time information, the method described above is applied to a large number of events for which the direction of flight is known. Nearly all tracks tagged as ontime (see Section 3.2.5) are due to particles traveling in beam direction, since the fraction of cosmic events in the sample of ontime events is only about 10^{-4} [A+06a] and therefore negligible concerning this purpose. The 2011 ontime events passing the same cuts that are applied for the calibration of signal path A (see Section 5.5) are selected for the determination of the error. In addition, a minimum of six data points in the flight time over distance plot are required. Figure 6.14 shows the distribution of the residuals for all corresponding linear time of flight fits with a positive slope. A Gaussian is fitted to the residuals' distribution. Its standard deviation σ of about 5 ns is taken as the error of the time of flight measurements. The error of the distance of flight is derived from one of the event selection cuts: for the linear fit to the Kalman track digits, which is used as an approximation to the particle track through the detector, the maximum residuals are required to be less than 5 cm in both projection planes (see Section 5.5). This value is taken as the error of the distances of flight in Figures 6.10–6.13.
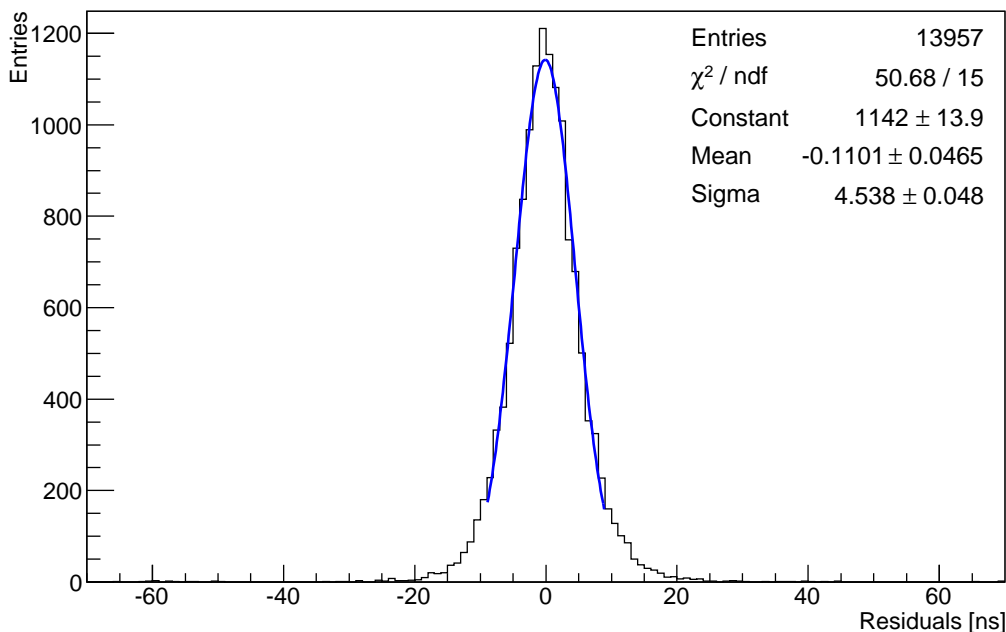
Figure 6.14: Distribution of the residuals of the linear fits to the time of flight data for all ontime events of the 2011 run which are passing the cuts described in the text. For all ontime events a positive slope is used for the linear fit. A Gaussian is fitted to the residuals' distribution.

The dataset of all 2011 ontime events passing the selection cuts specified above is also used to test the capability of the presented method to identify a particle's direction of flight by means of the time of flight measurements. For this purpose, the RMS of the residuals is determined for both possible fits, the one for particles traveling in beam direction, and the one for the opposite flight direction. For 91.9 % of the selected ontime events, the direction of flight is identified correctly by using the lower RMS of the residuals as an indicator.

Although the average error of ±4.5 ns on the flight times is small enough to determine the flight direction for the majority of particles, the method still fails for part of the events, since the error on the time information for individual trigger signals may be considerably larger than the average error. For one thing, the signal propagation delays on the cables labeled A′ in Figure 4.4 may deviate from the expected value. The 14 timing boards of each trigger channel are connected to the corresponding OPE board by individual twisted pair cables. The OPE board provides the logic OR of all incoming signals, which is transmitted via the twisted pair cable A″ to the OTB (see Section 4.1). The calibration of signal path A does not take differences in the propagation delays on the cables A′ within the same trigger channel into account. The relative correction value for path A for a specific trigger channel only regards the average propagation delay of the corresponding 14 cables A′, as well as the delay on cable A″ (see Section 5.5). Therefore, the propagation delay of individual timing board signals may deviate from the average value on this signal path. For another thing, an additional error of up to several tens of nanoseconds may be added to the time of flight determined by an individual trigger channel if an XPC/RPC detector signal is wrongly assigned to the trigger signal. Despite the selection of unambiguous detector hits in the trigger planes, requiring exactly one readout signal per coordinate, there may still be interactions in the detector that generate a trigger signal, but are undetected by the direct readout for the track reconstruction. This is possible because the timing boards are completely independent from the direct detector readout and have separate threshold settings. If a trigger signal is generated by a hit in an XPC/RPC plane and is not detected by the direct readout, but is wrongly associated with another hit in the same plane, the time of flight determined in this case deviates from the correct value by the signal propagation time between the two detector hits. In summary it can be said, that larger errors for the time information of a few individual trigger signals may cause a misidentification of the direction of flight. This applies specifically to short particle tracks due to their relatively short times of flight and fewer points of measurement.

Finally, the average error on the flight times can be taken as a measure for the error of the trigger signal timing. The value of $\pm 4.5\,$ns is well within the limit of $\pm 5\,$ns for achieving the designated momentum resolution. As an additional test for the quality of the timing calibration of the trigger system, Figure 6.15 shows the residuals of the linear fits to the time of flight data for all ontime events of the 2011 beam run. Here, each trigger channel is displayed separately. The selection cuts listed above are applied. The residuals' distribution for all 22 trigger channels are centered close to 0, which is a further indication for a successful timing calibration of the PT trigger system.

(a) SM 1   (b) SM 2
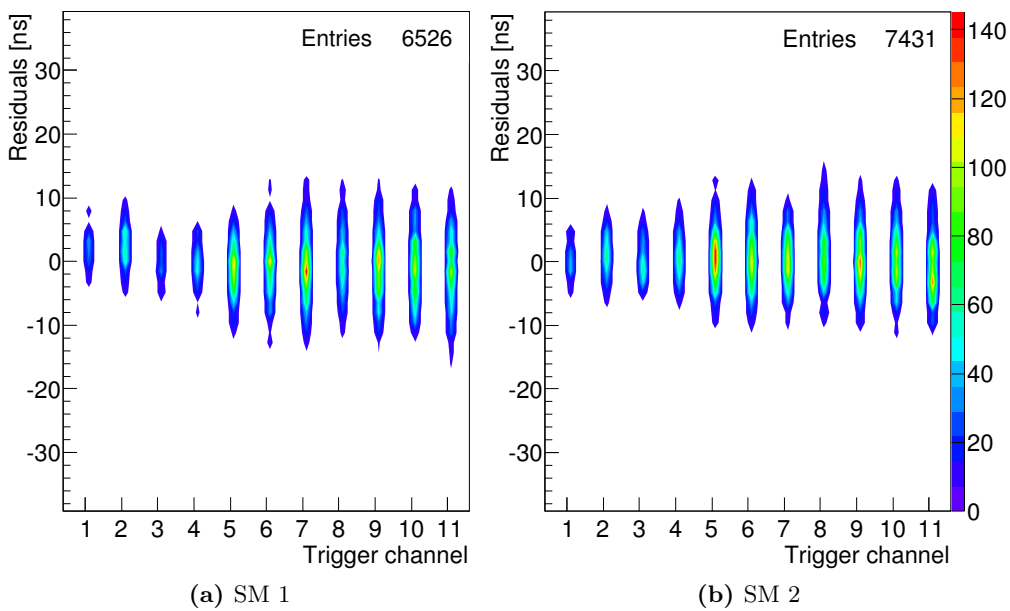
Figure 6.15: Two-dimensional histogram showing the residuals of the linear fits to the time of flight data for all ontime events of the 2011 beam run, displayed for each trigger channel separately. The selection cuts listed in the text are applied.

Chapter 7

Conclusion

The neutrino oscillation scenario is well-established today, owing to the measurement results of a multitude of solar, atmospheric, reactor and accelerator neutrino experiments. By now, all mass squared differences and mixing angles of the three-neutrino framework have been measured. However, many questions concerning the neutrino's properties still remain unanswered, requiring higher precision measurements for the oscillation parameters and new experimental approaches. The main goal of the OPERA experiment is to substantiate the neutrino oscillation scenario by the first direct observation of ν_τ appearance in the $\nu_\mu \to \nu_\tau$ oscillation channel on an event-by-event basis.

OPERA has the unique capability to resolve individual ν_τ events on a large scale using lead/emulsion targets and automated high-speed scanning systems. So far, OPERA has detected four ν_τ candidates, establishing $\nu_\mu \to \nu_\tau$ oscillations with a significance of $4.2\,\sigma$. As the scanning of the emulsion films still continues, the significance of the ν_τ appearance signal will increase even further if additional candidate events are found. Moreover, the search for transitions of the type $\nu_\mu \to \nu_e$ allows OPERA to constrain the parameter space of a potential sterile neutrino.

In addition to the passive emulsions in the target sections, electronic detectors are indispensable to identify neutrino interactions in real-time and locate their vertices. Magnetic spectrometers are used to determine the charge and momentum of muons, which is necessary in order to increase the oscillation signal by also exploiting the muonic τ decay channel and to reduce the background by rejecting charmed hadron decays. A precise particle tracking in close proximity of the magnetic field is provided by the drift tube detector. Its trigger signals are delivered by selected RPC/XPC planes. The first incoming signal is distributed to all drift tubes of the respective super module as a common stop signal, triggering the readout. The major contribution to the intrinsic error of the drift time measurement is the uncertainty on the trigger

timing, necessitating a precise calibration of all trigger signal paths in order to reach the required spatial resolution.

Within this thesis, a timing calibration procedure for the trigger system of the OPERA drift tube detector was developed and applied. The delay of the stop signal distribution behind the trigger boards was measured by means of test pulses. For the calibration of the signal paths from the trigger boards to the TDC boards, the detector plane which produced the trigger signal had to be known. To facilitate the determination of the signal generating trigger station, additional cables and LVDS converters were installed. This allowed for using a large number of arbitrary signals for the calibration, including electronic noise, which improved the precision of the resulting correction values significantly. In the final calibration step the signal delays from the timing boards to the trigger boards were analyzed, using signals produced by muons crossing the spectrometers. In addition to the previously determined delay values, the propagation delay inside the RPCs/XPCs and the time of flight between planes contributing to the trigger signal had to be determined. A set of rigorous selection cuts, taking detector inefficiencies and possible track reconstruction ambiguities into account, was developed to ensure a clean data sample for the calibration.

Furthermore, the correlation between the trigger timing and the ambient temperature was studied. A minor temperature dependence of the signal delay on the trigger board was observed, although too small to be compensated and therefore negligible. With all calibrations implemented, a spatial resolution of $255\,\mu\mathrm{m}$ was achieved, the same as for test setups with a trigger timing uncertainty close to zero, illustrating the success of the timing calibration procedure.

Finally, the possibility to perform time of flight measurements with cosmic muons using the fully calibrated trigger system was demonstrated. A method to determine a particle's direction of flight was presented. Additionally, the average error on the flight times was determined. Its value of $\pm 4.5\,\mathrm{ns}$ is a measure for the error of the trigger timing and is well within the limit of $\pm 5\,\mathrm{ns}$ required to achieve the designated momentum resolution for the OPERA spectrometers.

Appendix A

List of Abbreviations

ADC	Analog-to-digital converter
BMS	Brick Manipulator System
BooNE	Booster Neutrino Experiment
BOREX	Boron Solar Neutrino Experiment
CAN	Controller Area Network
CC	Charged current
CERN	Conseil Européen pour la Recherche Nucléaire
CL	Confidence level
CNGS	CERN Neutrinos to Gran Sasso
COBRA	Cadmium Zinc Telluride 0-Neutrino Double-Beta Research Apparatus
CP	Charge parity
CPLD	Complex programmable logic device
CS	Changeable Sheets
DAC	Digital-to-analog converter
DAQ	Data acquisition
DONUT	Direct Observation of Nu Tau
ECC	Emulsion Cloud Chamber
ECHo	Electron Capture ^{163}Ho Experiment
ECM	Ethernet Controller Mezzanine
Fermilab	Fermi National Accelerator Laboratory

GALLEX	Gallium Experiment
GERDA	Germanium Detector Array
GNO	Gallium Neutrino Observatory
GPS	Global Positioning System
HOLMES	The Electron Capture Decay of ^{163}Ho to Measure the Electron Neutrino Mass with sub-eV sensitivity
IH	Inverted hierarchy
IP	Impact parameter
J-PARC	Japan Proton Accelerator Research Complex
JUNO	Jiangmen Underground Neutrino Observatory
Kamiokande	Kamioka Nucleon Decay Experiment
KamLAND	Kamioka Liquid Scintillator Antineutrino Detector
KamLAND-Zen	KamLAND Zero Neutrino Double Beta Decay Search
KARMEN	Karlsruhe Rutherford Medium Energy Neutrino Experiment
KATRIN	Karlsruhe Tritium Neutrino Experiment
LED	Light-emitting diode
LEP	Large Electron-Positron Collider
LHC	Large Hadron Collider
LNGS	Laboratori Nazionali del Gran Sasso
LSND	Liquid Scintillator Neutrino Detector
LVDS	Low-voltage differential signaling
MAC-E Filter	Magnetic Adiabatic Collimation combined with an Electrostatic Filter
MINOS	Main Injector Neutrino Oscillation Search
NC	Neutral current
NH	Normal hierarchy
NIM	Nuclear Instrumentation Module
NOMAD	Neutrino Oscillation Magnetic Detector
NOvA	NuMI Off-Axis ν_e Appearance
NuMI	Neutrinos at the Main Injector

OPE	OR plane electronics
OPERA	Oscillation Project with Emulsion-Tracking Apparatus
OSUB	OPERA Support Board
OTB	OPERA Trigger Board
OVTB	Overall Trigger Board
PECL	Positive emitter-coupled logic
PET	Polyethylene terephthalate
PMNS	Pontecorvo-Maki-Nakagawa-Sakata (matrix)
PMT	Photomultiplier tube
p.o.t.	Protons on target
PP	Polypropylene
PT	Precision Tracker
PWC	Pulse width controller
RENO	Reactor Experiment for Neutrino Oscillations
RMS	Root mean square
RPC	Resistive plate chamber
SAGE	Soviet-American Gallium Experiment
SM	Super Module
SNO	Sudbury Neutrino Observatory
SOX	Short distance neutrino Oscillations with Borexino
SPS	Super Proton Synchrotron
T2K	Tokai to Kamioka
TB	Timing Board
TDC	Time-to-digital converter
TT	Target Tracker
TTL	Transistor-transistor logic
UTC	Coordinated Universal Time
WLS	Wavelength shifting
XPC	Crossed RPC

Appendix B

Definitions of All Relevant Time Intervals

The following tables list all parameters used within this thesis to denote different time intervals. The time intervals are named t with an index indicating the path a particle or signal traveled during the interval. A digit added to the index is used to distinguish different signals.

Table B.1: Definitions of all time intervals used in Chapter 4 in connection with the description of the drift time measurement

Name	Description
$t_{trigger}$	Time interval between the particle's crossing of the reference plane and the delivery of the common stop signal to the TDCs (In Chapter 5 this interval is broken down into its subcomponents.)
t_{tof}	Time of flight between the reference plane and a detector part (here: a drift tube)
t_{drift}	Drift time of the electrons through the gas inside a drift tube
t_{wire}	Signal propagation time on the anode wire to the readout end of the drift tube
t_{cable}	Signal propagation time from the readout end of the drift tube to the TDC board input (includes the amplifier/discriminator board and the twisted pair cable)
t_{TDC}	Time interval measured by a TDC channel between the start and stop signals

Table B.2: Definitions of all time intervals used in Chapter 5 in connection with the calibration of the trigger system

Name	Description
t_{tof}	Time of flight between the reference plane and a detector part (here: a trigger plane)
t_{prop}	Signal propagation time on an XPC/RPC signal strip, from the point of the particle interaction to the readout end of the strip
t_A	Signal propagation time on signal path A, from the readout end of the XPC/RPC to the OTB master (includes the interconnection board, the timing board, the OPE board, the PECL to TTL converter at the OTB input stage, and the twisted pair cables in between)
t_B	Signal propagation time on signal path B, from the OTB master input stage to the TDC board (includes the TTL to LVDS converter on the OTB, and the twisted pair cable leading to the TDC board input stage)
t_C	Signal propagation time on signal path C, from the OTB master to the stop signal input of the TDC board (includes the entire OTB master with the exception of the PECL to TTL converter, the TTL line driver, the OVTB, the OTB slave, all coaxial cables connecting these components, and the crate's backplane)
t_D	Signal propagation time on signal path D, branching off from path C just before the OVTB, and leading to the TDC board (includes the 1 m coaxial cable and the LVDS converter board)
t_{TDC}	Time interval measured by a TDC channel between the start and stop signals

Appendix C

Dataset Used for Calibrations

The following dataset is used for all calibration steps, unless noted otherwise. The electronic data collected by the detector during beam or cosmic runs is extracted from the DAQ system twice a day and saved in a file. Therefore, a so-called extraction corresponds to the data of twelve hours of detector operation.

The first commissioning run of the OPERA detector and the CNGS beam started in August 2006. The electronic detector installations were completed in 2007 and the commissioning was finalized with a cosmic run in February 2008. From June until November 2008 a CNGS beam run was conducted, followed by two weeks of cosmic run. However, the 2008 data is not used for the calibration of the PT trigger system described within this thesis. This is due to several interventions and hardware replacements on the PT during the first part of the run and especially because of the exchange of the first overall trigger implementation, using NIM components, for the OVTBs after the 2008 beam run (see Section 4.2.2). During the cosmic run in November 2008 (extractions 973–987) and at the beginning of the 2009 run the crossover trigger was activated causing a significant reduction of the trigger efficiency, most notably in the second SM (see Section 4.2.3). Therefore, this data is also not considered for the calibrations. In addition to that, the LVDS converters, which are used for several steps of the calibration, were introduced and operational not until about three weeks into the 2009 run (see Section 4.2.4).

Table C.1 lists the numbers of the first and the last extraction from each year used for the calibrations. Extractions affected by unstable detector performance at the beginning and at the end of the runs are left out. Table C.2 shows the numbers of the extractions within the OPERA runs that are omitted for the calibration due to detector failures or inefficiencies, especially regarding the PT trigger system.

Table C.1: Extractions of the OPERA detector runs 2009–2012 used for the calibration of the PT trigger system. Extractions affected by unstable detector performance at the beginning and at the end of the runs are left out. Individual extractions in between, that are omitted due to detector failures, are listed in Table C.2.

Year	First Extraction	Last Extraction
2009	9071	9352
2010	10186	10635
2011	11120	11647
2012	12119	12635

Table C.2: Extractions within the OPERA runs 2009–2012 that are omitted for the calibration due to detector failures or inefficiencies, especially regarding the PT trigger system

Year	Extraction Number(s)	Reason for Omission
2009	9000–9070	crossover trigger activated
2009	9167–9185	high voltage discharges in RPC plane 13, SM 1, causing high PT trigger rate in SM 1 and also severe noise in RPCs and PT
2010	10204–10207	OPE crate failure causing reduced PT trigger rate
2010	10237	RPC high voltage down, loss of PT trigger for about 70 minutes
2010	10277–10279	RPC and XPC high voltage down during CNGS maintenance
2010	10365	RPCs serving 2nd trigger station in SM 2 down for about one hour
2010	10432–10433	power cut due to faulty TT power supply, affecting 2nd and 3rd trigger station in SM 2
2010	10493–10495	high voltage of four RPC planes down, affecting 1st and 2nd trigger station in SM 1
2010	10578–10581	RPC high voltage down due to problems with the RPC gas system

(Table C.2 continued)

Year	Extraction Number(s)	Reason for Omission
2011	11135–11139	high voltage down for topmost row of RPC plane 14, SM 1, due to gas leak, affecting 2nd trigger station in SM 1
2011	11177	RPC high voltage in SM 1 temporarily down
2011	11227	RPC high voltage problems in SM 1
2011	11228	RPC gas system problems, high voltage temporarily down
2011	11339	DAQ crash due to partial power cut
2011	11340–11342	DAQ problems concerning several PT modules, PT DAQ temporarily down
2011	11369	tests on RPCs, DAQ temporarily down
2011	11431	high voltage of 1st PT plane in SM 1 down for about 30 minutes
2011	11433	several interventions on PT planes in SM 1
2011	11438–11439	high voltage down for topmost rows of RPC planes 12–14, SM 1, affecting 2nd trigger station in SM 1
2011	11561–11564	no data files with reconstructed tracks available due to problems with GPS synchronization
2011	11595	1st trigger station in SM 2 down for about one hour
2011	11617–11621	RPC high voltage problems affecting the PT trigger
2011	11632–11635	PT low voltage temporarily down due to broken cooling fan
2012	12163–12164	TT DAQ of SM 1 down
2012	12556	TT, several PT planes and PT trigger down due to TT power supply problem
2012	12557	several TT planes down
2012	12558–12565	6th PT plane in SM 1 down
2012	12577	TT DAQ down

List of Figures

List of Tables

Bibliography

[3M10]   3M Electronics Solutions Division, *Twisted Pair Flat Cable, 2100 Series*, Technical Data Sheet, TS-0762-D (2010).

[A+94]   Dzh. N. Abdurashitov et al., *Results from SAGE*, Phys.Lett. **B328** (1994), 234–248.

[A+96]   A. Adam et al., *The Forward muon detector of L3*, Nucl.Instrum.Meth. **A383** (1996), 342–366.

[A+01a] K. Abe et al., *Observation of large CP violation in the neutral B meson system*, Phys.Rev.Lett. **87** (2001), 091802.

[A+01b] A. Aguilar et al., *Evidence for neutrino oscillations from the observation of $\overline{\nu}_e$ appearance in a $\overline{\nu}_\mu$ beam*, Phys.Rev. **D64** (2001), 112007.

[A+01c] Q. R. Ahmad et al., *Measurement of the rate of $\nu_e + d \rightarrow p + p + e^-$ interactions produced by ^8B solar neutrinos at the Sudbury Neutrino Observatory*, Phys.Rev.Lett. **87** (2001), 071301.

[A+02]   B. Armbruster et al., *Upper limits for neutrino oscillations $\overline{\nu}_\mu \rightarrow \overline{\nu}_e$ from muon decay at rest*, Phys.Rev. **D65** (2002), 112001.

[A+03a] M. Apollonio et al., *Search for neutrino oscillations on a long baseline at the CHOOZ nuclear power station*, Eur.Phys.J. **C27** (2003), 331–374.

[A+03b] P. Astier et al., *Search for $\nu_\mu \rightarrow \nu_e$ oscillations in the NOMAD experiment*, Phys.Lett. **B570** (2003), 19–31.

[A+04a] P. Achard et al., *Measurement of the atmospheric muon spectrum from 20 to 3000 GeV*, Phys. Lett. B **598** (2004), no. 1, 15–32.

[A+04b] M. Ambrosio et al., *The OPERA muon spectrometer tracking electronics*, Nucl.Instrum.Meth. **A533** (2004), 173–177.

[A+05]   M. Altmann et al., *Complete results for five years of GNO solar neutrino observations*, Phys. Lett. **B616** (2005), 174.

[A⁺06a] R. Acquafredda et al., *First events from the CNGS neutrino beam detected in the OPERA experiment*, New J.Phys. **8** (2006), 303.

[A⁺06b] L. Arrabito et al., *Hardware performance of a scanning system for high speed analysis of nuclear emulsions*, Nucl.Instrum.Meth. **A568** (2006), 578–587.

[A⁺07a] T. Adam et al., *The OPERA experiment target tracker*, Nucl.Instrum.Meth. **A577** (2007), 523–539.

[A⁺07b] L. Arrabito et al., *Electron/pion separation with an emulsion cloud chamber by using a neural network*, JINST **2** (2007), P02001.

[A⁺07c] D. S. Ayres et al., *The NOvA Technical Design Report*, FERMILAB-DESIGN-2007-01 (2007).

[A⁺08a] S. Abe et al., *Precision Measurement of Neutrino Oscillation Parameters with KamLAND*, Phys.Rev.Lett. **100** (2008), 221803.

[A⁺08b] A. Anokhina et al., *Emulsion sheet doublets as interface trackers for the OPERA experiment*, JINST **3** (2008), P07005.

[A⁺09a] J. N. Abdurashitov et al., *Measurement of the solar neutrino capture rate with gallium metal. III: Results for the 2002–2007 data-taking period*, Phys.Rev. **C80** (2009), 015807.

[A⁺09b] R. Acquafredda et al., *The OPERA experiment in the CERN to Gran Sasso neutrino beam*, JINST **4** (2009), P04018.

[A⁺10a] N. Agafonova et al., *Measurement of the atmospheric muon charge ratio with the OPERA detector*, Eur.Phys.J. **C67** (2010), 25–37.

[A⁺10b] N. Agafonova et al., *Observation of a first ν_τ candidate in the OPERA experiment in the CNGS beam*, Phys.Lett. **B691** (2010), 138–145.

[A⁺11a] K. Abe et al., *Indication of Electron Neutrino Appearance from an Accelerator-produced Off-axis Muon Neutrino Beam*, Phys.Rev.Lett. **107** (2011), 041801.

[A⁺11b] K. Abe et al., *Solar neutrino results in Super-Kamiokande-III*, Phys. Rev. **D83** (2011), 052010.

[A⁺11c] R. J. Abrams et al., *International Design Study for the Neutrino Factory - Interim Design Report*, arxiv:1112.2853v1 (2011).

[A⁺11d] P. Adamson et al., *Improved search for muon-neutrino to electron-neutrino oscillations in MINOS*, Phys.Rev.Lett. **107** (2011), 181802.

[A$^+$11e]   N. Agafonova et al., *Study of neutrino interactions with the electronic detectors of the OPERA experiment*, New J.Phys. **13** (2011), 053051.

[A$^+$11f]   V. N. Aseev et al., *An upper limit on electron antineutrino mass from Troitsk experiment*, Phys.Rev. **D84** (2011), 112003.

[A$^+$12a]   Y. Abe et al., *Indication for the disappearance of reactor electron antineutrinos in the Double Chooz experiment*, Phys.Rev.Lett. **108** (2012), 131801.

[A$^+$12b]   Y. Abe et al., *Reactor electron antineutrino disappearance in the Double Chooz experiment*, Phys.Rev. **D86** (2012), 052008.

[A$^+$12c]   N. Agafonova et al., *Momentum measurement by the Multiple Coulomb Scattering method in the OPERA lead emulsion target*, New J.Phys. **14** (2012), 013026.

[A$^+$12d]   J. K. Ahn et al., *Observation of Reactor Electron Antineutrino Disappearance in the RENO Experiment*, Phys.Rev.Lett. **108** (2012), 191802.

[A$^+$12e]   F. P. An et al., *Observation of electron-antineutrino disappearance at Daya Bay*, Phys.Rev.Lett. **108** (2012), 171803.

[A$^+$13a]   P. Adamson et al., *Electron neutrino and antineutrino appearance in the full MINOS data sample*, Phys.Rev.Lett. **110** (2013), no. 17, 171801.

[A$^+$13b]   P. Adamson et al., *Measurement of Neutrino and Antineutrino Oscillations Using Beam and Atmospheric Data in MINOS*, Phys.Rev.Lett. **110** (2013), no. 25, 251801.

[A$^+$13c]   N. Agafonova et al., *New results on $\nu_\mu \to \nu_\tau$ appearance with the OPERA experiment in the CNGS beam*, JHEP **1311** (2013), 036.

[A$^+$13d]   N. Agafonova et al., *Search for $\nu_\mu \to \nu_e$ oscillations with the OPERA experiment in the CNGS beam*, JHEP **1307** (2013), 004.

[A$^+$13e]   M. Agostini et al., *Results on Neutrinoless Double-β Decay of ^{76}Ge from Phase I of the GERDA Experiment*, Phys.Rev.Lett. **111** (2013), no. 12, 122503.

[A$^+$13f]   B. Aharmim et al., *Combined Analysis of all Three Phases of Solar Neutrino Data from the Sudbury Neutrino Observatory*, Phys.Rev. **C88** (2013), 025501.

[A$^+$14a]   K. Abe et al., *Observation of Electron Neutrino Appearance in a Muon Neutrino Beam*, Phys.Rev.Lett. **112** (2014), 061802.

[A$^+$14b]   K. Abe et al., *Precise Measurement of the Neutrino Mixing Parameter θ_{23} from Muon Neutrino Disappearance in an Off-Axis Beam*, Phys.Rev.Lett. **112** (2014), no. 18, 181801.

[A$^+$14c]   P. Adamson et al., *Combined analysis of ν_μ disappearance and $\nu_\mu \to \nu_e$ appearance in MINOS using accelerator and atmospheric neutrinos*, Phys.Rev.Lett. **112** (2014), 191801.

[A$^+$14d]   P. A. R. Ade et al., *Planck 2013 results. XVI. Cosmological parameters*, Astron.Astrophys. **571** (2014), A16.

[A$^+$14e]   N. Agafonova et al., *Evidence for $\nu_\mu \to \nu_\tau$ appearance in the CNGS neutrino beam with the OPERA experiment*, Phys.Rev. **D89** (2014), no. 5, 051102.

[A$^+$14f]   N. Agafonova et al., *Measurement of TeV atmospheric muon charge ratio with the full OPERA data*, arxiv:1403.0244 (2014).

[A$^+$14g]   N. Agafonova et al., *Observation of tau neutrino appearance in the CNGS beam with the OPERA experiment*, PTEP **2014** (2014), no. 10, 101C01.

[A$^+$14h]   B. Alpert et al., *HOLMES - The Electron Capture Decay of 163Ho to Measure the Electron Neutrino Mass with sub-eV sensitivity*, arxiv:1412.5060 (2014).

[A$^+$14i]   K. Asakura et al., *Results from KamLAND-Zen*, arxiv:1409.0077v1 (2014).

[AA$^+$13]   A. A. Aguilar-Arevalo et al., *Improved Search for $\overline{\nu}_\mu \to \overline{\nu}_e$ Oscillations in the MiniBooNE Experiment*, Phys.Rev.Lett. **110** (2013), 161801.

[AF$^+$07]   R. Adinolfi Falcone et al., *The instrumented magnets for the OPERA experiment: Construction and commissioning*, Nucl.Phys.Proc.Suppl. **172** (2007), 165–167.

[B$^+$01]   F. Boehm et al., *Final results from the Palo Verde neutrino oscillation experiment*, Phys.Rev. **D64** (2001), 112001.

[B$^+$09a]   A. Bergnoli et al., *Performances of the OPERA RPCs*, Nucl.Instrum.Meth. **A602** (2009), 635–638.

[B$^+$09b]   A. Bergnoli et al., *The OPERA VETO system*, Nucl.Instrum.Meth. **A602** (2009), 653–657.

[B$^+$10]   G. Bellini et al., *Measurement of the solar ^8B neutrino rate with a liquid scintillator target and 3 MeV energy threshold in the Borexino detector*, Phys.Rev. **D82** (2010), 033006.

[B$^+$11]   G. Bellini et al., *Precision Measurement of the ^7Be Solar Neutrino Interaction Rate in Borexino*, Phys.Rev.Lett. **107** (2011), 141302.

[B$^+$12a]   E. Balsamo et al., *The OPERA RPCs front end electronics; a novel application of LVDS line receiver as low cost discriminator*, JINST **7** (2012), P11007.

[B$^+$12b]   A. Bertolin et al., *Long term performances of OPERA bakelite RPC system*, Nucl.Instrum.Meth. **A661** (2012), S60–S63.

[B$^+$12c]   A. Bertolin et al., *RPC time calibration and analysis of the 2011 bunched beam data*, OPERA Public Note 147 (2012).

[B$^+$13]   G. Bellini et al., *SOX: Short distance neutrino Oscillations with BoreXino*, JHEP **1308** (2013), 038.

[B$^+$14a]   G. Bellini et al., *Neutrinos from the primary proton-proton fusion process in the Sun*, Nature **512** (2014), no. 7515, 383–386.

[B$^+$14b]   B. Büttner et al., *Alignment methods for the OPERA drift tube detector*, Nucl.Instrum.Meth. **A747** (2014), 56–61.

[Ber14]   A. Bertolin, personal communication (2014).

[BP95]   J. N. Bahcall and M. H. Pinsonneault, *Solar models with helium and heavy element diffusion*, Rev.Mod.Phys. **67** (1995), 781–808.

[C$^+$56]   C. L. Cowan, Jr. et al., *Detection of the Free Neutrino: a Confirmation*, Science **124** (1956), 103–104.

[C$^+$64]   J. H. Christenson et al., *Evidence for the 2 pi Decay of the k(2)0 Meson*, Phys.Rev.Lett. **13** (1964), 138–140.

[C$^+$98]   B. T. Cleveland et al., *Measurement of the solar electron neutrino flux with the Homestake chlorine detector*, Astrophys.J. **496** (1998), 505–526.

[C$^+$07]   H. Chen et al., *Proposal for a New Experiment Using the Booster and NuMI Neutrino Beamlines: MicroBooNE*, Experiment proposal (2007).

[C$^+$08]   J. P. Cravens et al., *Solar neutrino measurements in Super-Kamiokande-II*, Phys.Rev. **D78** (2008), 032002.

[C$^+$09]   G. Corradi et al., *A 16 channels Timing Board for the OPERA RPCs*, OPERA Public Note 70 (2009).

[Cha14]   J. Chadwick, *Intensitätsverteilung im magnetischen Spektrum der β-Strahlen von Radium B + C*, Verh. Phys. Gesell. **16** (1914), 383–391.

[CNG14] CNGS website, `http://proj-cngs.web.cern.ch/proj-cngs/`, accessed: 27 January 2014.

[D⁺62] G. Danby et al., *Observation of high-energy neutrino reactions and the existence of two kinds of neutrinos*, Phys. Rev. Lett. **9** (1962), 36–44.

[D⁺68] R. Davis, Jr. et al., *Search for Neutrinos from the Sun*, Phys.Rev.Lett. **20** (1968), 1205–1209.

[D⁺04] S. Dusini et al., *The DAQ system of OPERA experiment and its specifications for the spectrometers*, Nucl.Instrum.Meth. **A518** (2004), 519–521.

[DiC13] A. Di Crescenzo, *Search for $\nu_\mu \to \nu_\tau$ oscillations in the OPERA experiment*, PhD thesis, Università degli Studi di Napoli Federico II (2013).

[E⁺13] J. Ebert et al., *Current Status and Future Perspectives of the COBRA Experiment*, Adv.High Energy Phys. **2013** (2013), 703572.

[F⁺96] Y. Fukuda et al., *Solar Neutrino Data Covering Solar Cycle 22*, Phys.Rev.Lett. **77** (1996), 1683–1686.

[F⁺98] Y. Fukuda et al., *Evidence for Oscillation of Atmospheric Neutrinos*, Phys.Rev.Lett. **81** (1998), 1562–1567.

[F+07a] A. Ferrari et al., *An updated Monte Carlo calculation of the CNGS neutrino beam*, Tech. Report CERN-AB-Note-2006-038 (2007).

[F⁺07b] A. Ferrari et al., *CNGS neutrino beam: From CERN to Gran Sasso*, Nucl.Phys.Proc.Suppl. **168** (2007), 169–172.

[F⁺08] T. Ferber et al., *The gas system of the drift tube detector of the neutrino experiment OPERA*, Nucl.Instrum.Meth. **A592** (2008), 493–497.

[F⁺09] G. Felici et al., *The Trigger System of the OPERA Precision Tracker*, OPERA Public Note 71 (2009).

[F⁺14] D. V. Forero et al., *Neutrino oscillations refitted*, Phys.Rev. **D90** (2014), 093006.

[Fer06] T. Ferber, *Messung der Gaseigenschaften unter Einfluss von molekularem Sauerstoff und Aufbau eines Gassystems für das Driftröhren-Myon-Spektrometer des OPERA-Detektors*, diploma thesis, Universität Hamburg (2006).

[G⁺00]   M. Guler et al., *OPERA: An appearance experiment to search for* $\nu_\mu \leftrightarrow \nu_\tau$ *oscillations in the CNGS beam*, Experiment proposal (2000).

[G⁺11]   A. Gando et al., *Constraints on* θ_{13} *from a three-flavor oscillation analysis of reactor antineutrinos at KamLAND*, Phys.Rev. **D83** (2011), 052002.

[G⁺14]   L. Gastaldo et al., *The Electron Capture* ^{163}Ho *Experiment ECHo*, J.Low Temp.Phys. **176** (2014), no. 5-6, 876–884.

[Göl06]   C. Göllnitz, *Entwicklung und Test von Überwachungs- und Steuerungseinheiten sowie Bestimmung von Betriebsparametern des OPERA Precision Trackers*, diploma thesis, Universität Hamburg (2006).

[Göl12]   C. Göllnitz, *Alignment des Driftröhrendetektors am Neutrino-Oszillationsexperiment OPERA*, PhD thesis, Universität Hamburg (2012).

[H⁺06]   J. Hosaka et al., *Solar neutrino measurements in Super-Kamiokande-I*, Phys.Rev. **D73** (2006), 112001.

[Jan08]   B. Janutta, *Inbetriebnahme und Funktionsnachweis des OPERA Precision Trackers insbesondere des Zeitmesssystems*, PhD thesis, Universität Hamburg (2008).

[Jes09]   H. Jeschke, *Der Overall-Trigger für das Driftröhrenspektrometer des OPERA-Neutrinoexperiments*, diploma thesis, Universität Hamburg (2009).

[K⁺01]   K. Kodama et al., *Observation of tau neutrino interactions*, Phys.Lett. **B504** (2001), 218–224.

[K⁺05]   Ch. Kraus et al., *Final results from phase II of the Mainz neutrino mass search in tritium beta decay*, Eur.Phys.J. **C40** (2005), 447–468.

[K⁺10]   F. Kaether et al., *Reanalysis of the GALLEX solar neutrino flux and source experiments*, Phys. Lett. **B685** (2010), 47–54.

[Kae07]   F. Kaether, *Datenanalyse des Sonnenneutrinoexperiments GALLEX*, PhD thesis, Universität Heidelberg (2007).

[Kre08]   C. Kreyser, *Studien zum Einfluss von Magnetfeldern auf die Funktionsweise von Drahtkammern*, diploma thesis, Universität Hamburg (2008).

[Len07]   J. Lenkeit, *Kalibrationsmessungen für das Driftröhren-Myon-Spektrometer des OPERA-Detektors*, diploma thesis, Universität Hamburg (2007).

[Li14]   Y.-F. Li, *Overview of the Jiangmen Underground Neutrino Observatory (JUNO)*, Int.J.Mod.Phys.Conf.Ser. **31** (2014), 1460300.

[LNF14]   Laboratori Nazionali di Frascati website, `https://www.lnf.infn.it/esperimenti/opera/scanning/figs/brick.png`, accessed: 15 April 2014.

[M+62]   Z. Maki et al., *Remarks on the unified model of elementary particles*, Prog.Theor.Phys. **28** (1962), 870–880.

[M+07]   A. Mengucci et al., *Gas mixture studies for streamer operation of Resistive Plate Chambers at low rate*, Nucl.Instrum.Meth. **A583** (2007), 264–269.

[Mar10]   J. Marteau, *The OPERA global readout and GPS distribution system*, Nucl.Instrum.Meth. **A617** (2010), 291–293.

[Max02]   Maxim Integrated Products, *DS1110 10-Tap Silicon Delay Line*, Data Sheet (2003).

[MSC04]   MSC Vertriebs GmbH, *Benutzerhandbuch DES OPERA*, Version 10, user manual (2004).

[MSC10]   MSC Vertriebs GmbH, *User Manual MSC TDC501*, Version 1.4, user manual (2010).

[N+06]   T. Nakamura et al., *The OPERA film: New nuclear emulsion for large-scale, high-precision experiments*, Nucl.Instrum.Meth. **A556** (2006), 80–86.

[O+14]   K. A. Olive et al., *Review of Particle Physics*, Chin.Phys. **C38** (2014), 090001.

[Old09]   C. Oldorf, *Studien zu den Nachweiseigenschaften des OPERA-Driftröhrenspektrometers*, diploma thesis, Universität Hamburg (2009).

[Pao09]   A. Paoloni, personal communication (2009).

[Pao14]   A. Paoloni, *OPERA RPC system performances*, OPERA Note 169 (2014).

[Pau25]   W. Pauli, *Über den Zusammenhang des Abschlusses der Elektronengruppen im Atom mit der Komplexstruktur der Spektren*, Z. Phys. **31** (1925), no. 1, 765–783.

[Pon57]   B. Pontecorvo, *Mesonium and anti-mesonium*, Sov.Phys.JETP **6** (1957), 429.

[Pon60]   B. Pontecorvo, *Electron and Muon Neutrinos*, Sov.Phys.JETP **10** (1960), 1236–1240.

[S+06]   S. Schael et al., *Precision electroweak measurements on the Z resonance*, Phys.Rept. **427** (2006), 257–454.

[S+08]   B. Steinke et al., *The OPERA PT Trigger System: implementation and performance results*, OPERA Note 90 (2008).

[Sau77]   F. Sauli, *Principles of Operation of Multiwire Proportional and Drift Chambers*, CERN-77-09, report (1977).

[Sch60]   M. Schwartz, *Feasibility of Using High-Energy Neutrinos to Study the Weak Interactions*, Phys. Rev. Lett. **4** (1960), no. 6, 306–307.

[Sch09]   J. Schütt, *OVTB, OPERA Overall Trigger Board*, Universität Hamburg, user manual (2009).

[Seo14]   S.-H. Seo, *New Results from RENO*, Talk given at the XXVI International Conference on Neutrino Physics and Astrophysics, Boston, USA (2014).

[Sir07]   G. Sirri, *Fast automated scanning of OPERA emulsion films*, Nucl.Phys.Proc.Suppl. **172** (2007), 324–326.

[Spe14]   Spectra-Strip website, `http://www.spectra-strip.com/ecpartsearch3.cfm?partID=361`, accessed: 9 June 2014.

[Ste08]   B. Steinke, *Der Trigger für das OPERA-Driftröhrenspektrometer*, diploma thesis, Universität Hamburg (2008).

[UG25]   G. E. Uhlenbeck and S. Goudsmit, *Ersetzung der Hypothese vom unmechanischen Zwang durch eine Forderung bezüglich des inneren Verhaltens jedes einzelnen Elektrons*, Die Naturwissenschaften **13** (1925), no. 47, 953–954.

[Vot12]   L. Votano, *The Gran Sasso Laboratory*, Eur.Phys.J.Plus **127** (2012), 109.

[Wol10]   J. Wolf, *The KATRIN Neutrino Mass Experiment*, Nucl.Instrum. Meth. **A623** (2010), 442–444.

[Won07]   B. S. Wonsak, *Die Spurrekonstruktion für das Driftröhren-Myon-Spektrometer des Neutrino-Experiments OPERA*, PhD thesis, Universität Hamburg (2007).

[Won11]   B. S. Wonsak, personal communication (2011).

[Z+05]   R. Zimmermann et al., *The precision tracker of the OPERA detector*,
          Nucl.Instrum.Meth. **A555** (2005), 435–450.

[Zha14]   C. Zhang, *Recent Results From Daya Bay*, Talk given at the XXVI
          International Conference on Neutrino Physics and Astrophysics,
          Boston, USA (2014).

[Zim99]   R. Zimmermann, *Zeitmeßelektronik für den HERA-B-Detektor*, PhD
          thesis, Universität Rostock (1999).